Universität Karlsruhe (TH)

IEKP-KA/2004-16

Untersuchung der Eigenschaften von B*-Mesonen und von angeregten b-Hadronen

Zur Erlangung des akademischen Grades eines

Doktors der Naturwissenschaften

von der Fakultät für Physik der Universität (TH) Karlsruhe

genehmigte

Dissertation

von

Dipl.-Phys. Markus Moch
aus Bruchsal

Tag der mündlichen Prüfung: 16.07.2004
Referent: Prof. Dr. M. Feindt, Institut für Experimentelle Kernphysik
Korreferent: Prof. Dr. G. Quast, Institut für Experimentelle Kernphysik

Zusammenfassung

B^*-Mesonen und angeregte b-Hadronen wurden in multihadronischen Z^0-Zerfällen mit dem DELPHI-Detektor am LEP-Beschleiniger untersucht. Mit Hilfe dieser Messungen lassen sich Vorhersagen von nicht-perturbativen Modellen testen, die auf der Effektiven Theorie schwerer Quarks oder auf der Wahl eines Potentials basieren, was Fortschritte im Verständnis der Form des Potentials der Quantenchromodynamik (QCD) ermöglicht. Schwere Hadronen sind hierfür besonders geeignet, da man sie als das QCD-Äquivalent zu Wasserstoff ansehen kann. Dabei nimmt das schwere Quark[1] die Rolle des Protons und das leichte Quark[2] (oder die leichten Quarks) die Rolle des Elektrons im Wasserstoffatom ein. Diese Messungen können als Eingangsgrößen für Gitterrechnungen dienen, deren Ergebnisse dadurch verbessert werden können. Zusätzlich minimieren Messungen der Produktionsraten von angeregten b-Hadronen die Unsicherheiten bezüglich der Produktionsraten der primär im e^+e^--Annihilationsprozess erzeugten, schwach zerfallenden b-Hadronen. Außerdem können diese Messungen helfen, die Hadronisierung[3] besser zu verstehen. Zudem sind genaue Messungen dieser Produktionsraten wichtig für Untersuchungen der B^0-Oszillationen und der CP-Verletzung im B-System.

Für die im Rahmen dieser Arbeit durchgeführten Analysen war es erforderlich, B^+- und B^0-Mesonen voneinander und von den anderen b-Hadronen zu trennen. Hierfür wurden die schwach zerfallenden b-Hadronen inklusiv rekonstruiert. Deren rekonstruierte Energie wurde korrigiert, um Verlusten durch neutrale Teilchen und Ineffizienzen in der Rekonstruktion Rechnung zu tragen. Die Trennung der b-Hadronen wurde durch den Einsatz von neuronalen Netzen erreicht.

Die B^*-Mesonen wurden durch Kombination der B^+- bzw. B^0-Mesonen mit Photonen rekonstruiert, welche vor der Zeitprojektionskammer von DELPHI in Elektron-Positron-Paare konvertiert waren. Dadurch war es möglich, jeweils einen mit B^{+*}- und B^{0*}-Mesonen angereicherten Datensatz und einen in beiden Mesonarten abgereicherten Datensatz zu erhalten. Dieses Verfahren wurde sowohl für die Daten als auch für die auf dem JETSET 7.3-Modell[4] basierende DELPHI-Simulation von Z^0-Zerfällen durchgeführt. Die Anpassung der Simulation an die Daten ergab folgenden Wert für die hiermit erstmals bestimmte Isospinaufspaltung:

$$m(B_u^{+*}) - m(B_d^{0*}) - m(B_u^+) + m(B_d^0) = -0.2 \pm 1.4(\text{stat}) \pm 0.9(\text{syst}) \text{ MeV/c}^2.$$

Der erste Fehler gibt die statistische und der letzte Fehler die systematische Unsicherheit an. Aus dieser Messung lässt sich die Hyperfeinaufspaltung bei den geladenen B_u-Mesonen zu

$$m(B_u^{+*}) - m(B_u^+) = 45.7 \pm 0.9 \text{ MeV/c}^2$$

[1] c- oder b-Quark

[2] u-, d- oder s-Quark

[3] D.h. wie Hadronen aus den im Z^0-Zerfall entstandenen primären Quarks entstehen.

[4] T. Sjöstrand, Computer Phys. Com. **39** (1986) 347; T. Sjöstrand und M. Bengtson, Computer Phys. Comm. **43** (1987) 367.

und bei den neutralen B_d-Mesonen zu

$$m(B_d^{0*}) - m(B_d^0) = 45.9 \pm 0.9 \text{ MeV/c}^2$$

bestimmen. Diese Resultate ergeben zusammen mit dem Weltmittelwert[5] für $m(B_d^0) - m(B_u^+)$ von 0.33 ± 0.28 MeV/c^2 eine Massenaufspaltung für die B*-Mesonen von:

$$m(B_d^{*0}) - m(B_u^{*+}) = 0.5 \pm 1.7 \text{ MeV/c}^2.$$

Orbital angeregte B-Mesonen (sogenannte B**-Mesonen) wurden durch die Kombination der B^+- und B^0-Mesonen mit Pionen bzw. Kaonen rekonstruiert, deren Ursprung der Primärvertex war. Neuronale Netze wurden eingesetzt, um Datensätze zu bekommen, in denen diese Mesonen an- bzw. abgereichert waren. Desweiteren wurde ein neuronales Netz benutzt, um den Q-Wert[6] verschiebungsfrei zu rekonstruieren. Man unterscheidet bei den B**-Mesonen zwischen schmalen und breiten Zuständen - je nachdem, welche Zerfälle erlaubt sind. Da die Sensitivität nicht hoch genug war, um breite $B_{u,d}^{**}$-Zustände identifizieren zu können, wurden Annahmen bezüglich ihrer Massenaufspaltungen und Produktionsraten relativ zu den schmalen Zuständen gemacht. Diese Annahmen basieren auf Vorhersagen der Effektiven Theorie schwerer Quarks und Messungen von Mesonen, die ein c-Quark enthalten. Dies führt zu folgender Gesamtproduktionsrate pro b-Quarkjet für $B_{u,d}^{**}$-Mesonen:

$$\frac{\sigma(B_{u,d}^{**}) \cdot \text{BR}(\text{B}_{\text{u,d}}^{**} \to \text{B}^{(*)}\pi)}{\sigma_b} = 0.153 \pm 0.014(\text{stat})^{+0.027}_{-0.008}(\text{syst}) \pm 0.015(\text{model}).$$

Hier gibt der erste Fehler die statistische, der zweite Fehler die systematische und der letzte Fehler die Unsicherheit aufgrund der Modellannahmen an. Die Produktionsrate der schmalen Zustände pro b-Quarkjet wurde bestimmt zu:

$$\left(\frac{\sigma(B_{u,d}^{**}) \cdot \text{BR}(\text{B}_{\text{u,d}}^{**} \to \text{B}^{(*)}\pi)}{\sigma_b}\right)_{\text{schmal}} = 0.088 \pm 0.007(\text{stat})^{+0.013}_{-0.004}(\text{syst}) \pm 0.011(\text{model}).$$

Die Masse des B_2^*-Mesons, eines der schmalen Zustände, wurde gemessen zu:

$$m(B_2^*) = 5742 \pm 12 \text{ MeV/c}^2.$$

Die Messung der Massenaufspaltung zwischen den beiden schmalen Zuständen B_2^* und B_1 ergab

$$m(B_2^*) - m(B_1) = 15 \pm 13(\text{stat}) \pm 4(\text{syst}) \pm 5(\text{model}) \text{ MeV/c}^2,$$

was insgesamt zu einer B_1-Masse von

$$m(B_1) = 5727 \pm 19 \text{ MeV/c}^2$$

führt.

[5] Particle Data Group, K. Hagiwara et al, Phys. Rev. **D 66** (2002) 010001.

[6] Der Q-Wert ist definiert als die Differenz zwischen der invarianten Masse des ursprünglichen Teilchens - hier B**-Mesonen - und der Masse seiner Zerfallsteilchen.

Bei B_s^{**}-Mesonen konnte nur ein schmales Signal beobachtet werden. Dieses wurde dem Zerfall $B_{s2}^* \to BK$ zugeordnet. Die Produktionsrate pro b-Quarkjet wurde bestimmt zu:

$$\frac{\sigma(B_{s2}^*) \cdot \mathrm{BR}(B_{s2}^* \to BK)}{\sigma_b} = 0.0093 \pm 0.0020(\mathrm{stat}) \pm 0.0013(\mathrm{syst}).$$

Die B_{s2}^*-Masse wurde gemessen zu:

$$m(B_{s2}^*) = 5852 \pm 4 \ \mathrm{MeV/c^2}.$$

Eine Suche nach $\Sigma_b^{(*)}$-Baryonen wurde durchgeführt, indem inklusiv rekonstruierte Λ_b-Baryonen mit einem vom Primärvertex stammenden geladenen Pion kombiniert wurden. Ein signifikantes Signal konnte nicht beobachtet werden. Eine obere Schranke auf die Produktionsrate pro b-Quarkjet für eine schmale Resonanz wurde im Q-Wertbereich von 0 bis 300 $\mathrm{MeV/c^2}$ mit einem Vertrauensintervall von 95% zu

$$\frac{\sigma(\Sigma_b^{(*)}) \cdot \mathrm{BR}(\Sigma_b^{(*)} \to \Lambda_b \pi)}{\sigma_b} < 0.0124 \ @ \ 95\% \, \mathrm{CL}$$

bestimmt.

Universität Karlsruhe (TH)

Study of B*-Meson and of Excited b-Hadron Properties

Zur Erlangung des akademischen Grades eines

Doktors der Naturwissenschaften

von der Fakultät für Physik der Universität (TH) Karlsruhe

genehmigte

Dissertation

von

Dipl.-Phys. Markus Moch
aus Bruchsal

Tag der mündlichen Prüfung: 16.07.2004
Referent: Prof. Dr. M. Feindt, Institut für Experimentelle Kernphysik
Korreferent: Prof. Dr. G. Quast, Institut für Experimentelle Kernphysik

Contents

List of Figures

List of Tables

Chapter 1

Introduction

We all meandered through our schooling
haphazard; so, to God be thanks,
it's easy, without too much fooling,
to pass for cultured in our ranks.

A. S. Pushkin
(trans. Ch. Johnston)

Particle physics deals with questions like how matter is formed, of which building blocks matter is made up and which forces keep them together. This is also an important issue for understanding the beginning of the universe. The best way for studying these questions is to obtain similar conditions to those predominating the universe shortly after the Big Bang. This is achieved in particle accelerators.

One of the forces mentioned above is the strong interaction which binds particles called *quarks* together in *hadrons*. Two types of hadrons are known: mesons containg a quark and an antiquark, and baryons, bound states of three quarks (or antiquarks). The theory describing the strong interaction is called *Quantum Chromodynamics (QCD)*. The major problem in studying this force is that there are no free quarks due to the nature of the strong interaction. Thus, it is not easy to learn anything about that force and QCD both theoretically and experimentally. But the properties of hadrons can be studied in accelerators where they are produced in *jets*. These events are called *multihadronic events* because of the high multiplicity of hadrons in such events. By analysing such events and the generated hadrons conclusions can be drawn about quarks and the strong interaction.

Very good candidates for studying the potential of QCD are hadrons containing quarks with a relatively high mass, the charm (c-) and the bottom (b-)quark. These *heavy hadrons* are an analogon to the hydrogen atom which has been very useful to study and understand the electromagnetic force and the theory describing it. The heavy quark takes on the part of the proton in the hydrogen atom, and the electron is replaced by one of the light quarks in the case of of heavy-light mesons. Since the b-quark is heavier than the c-quark, hadrons containing the first fulfil this analogon better than hadrons containing the latter. An important issue here is the spectroscopy of the different hadron states, i.e. what the masses of the states are. Especially important are the mass splittings between the members of multiplets which are predicted by an effective theory of QCD, the *Heavy Quark Effective Teory (HQET)*. These mass splittings are comparable to the hyperfine splitting in hydrogen atoms. From these

measurements it is possible to extract some parameters of HQET. Moreover, the results of these measurements can be used as input to calculations on the lattice.

An accelerator where heavy hadrons were produced, was the copious Large Electron Positron collider LEP. In its first phase it ran at an energy where mainly a particle called Z^0-boson was produced. This particle can decay into a b-quark pair which then hadronises to ground state or excited heavy hadrons. These events are called b-events. How many of the b-hadrons are produced as excited states is an open question. The answer can help to better understand the process of hadronisation. Moreover, a large production rate of excited states would be useful in tagging the b-quark flavour (i.e. b or $\bar{b}$) of a b-hadron at the time of its production. This is important for $B^0_{d,s}$-oscillation and CP violation studies.

One of the detectors at LEP was called DELPHI[1]. It was a detector well suited for reconstructing b-quark events due to its vertex detector and tracking system. Powerful particle identification was made possible by the combination of energy loss measurements from the Time Projection Chamber with information from the Ring Imaging Cherenkov counters. This was an important tool for reconstructing and discriminating the different b-hadrons. Excited b-hadrons decay either strongly or electromagnetically into ground state hadrons which decay further mainly into c-hadrons. These mesons are reconstructed inclusively by the use of artifical neural networks.

The hyperfine excitation of a ground state B-meson (just called B or B-meson) is a B^*-meson. This meson decays into a B-meson and a photon. Since this photon has a very small energy it has to be reconstructed with the help of an electron-positron pair which is created when the photon converts. Orbital excitations of B-mesons are generically called B^{**}. $B^{**}_{u,d}$-mesons decay into B- or B^*-mesons and a pion, while B^{**}_s-mesons are supposed to decay into a kaon instead of a pion. A study of all these states is presented in this thesis. For b-baryons, there are three baryons which are not orbitally or radially excited. The ground state b-baryon Λ_b is well-known, but there is no confirmed observation of or published result about the other two baryons Σ_b and Σ_b^*. A search for these baryons is presented in this thesis as well.

This thesis is organised as follows: chapter 2 briefly introduces the theoretical basics of the quark model and QCD and the current understanding of hadron production in Z^0-decays. Theoretical and experimental results about B^*-mesons and excited b-hadrons are presented in chapter 3. The functionality of artifical neural networks is explained very briefly in chapter 4, which also contains an introduction to the detector, the reconstruction of charged particles and low energetic photons and the tagging of b-events. Inclusive reconstruction and identification of b-hadrons is explained in chapter 5. The measurement of mass splittings in the B^*-B system is presented in chapter 6 and the study of orbitally excited B-mesons in chapter 7 along with an explanation of the search for $\Sigma_b^{(*)}$-baryons. The summary of this thesis can be found in chapter 8.

[1] Detector with Lepton, Photon and Hadron Identification.

Chapter 2

Theoretical Basics

In this chapter a brief introduction into the theory of strong interactions and hadrons is given which is necessary for the understanding of the analyses presented in this thesis. Starting from the quark model for mesons and baryons, the basic concepts of Quantum Chromodynamics (QCD) are developed. Emphasis is given to the symmetries of QCD, especially the heavy quark symmetry is discussed, which leads to an effective theory of QCD, the Heavy Quark Effective Theory (HQET).

Then, the production mechanism of hadrons at LEP is described. This is followed by a description of the current phenomenological and experimental knowledge of B-meson spectroscopy.

2.1 The Quark Model

Today it is well known that protons and neutrons are not elementary particles, since they consist of three fundamental particles which are called quarks[1]. This traces back to the discovered symmetries in the spectrum of hadrons by Gell-Mann and Ne'emen [1], which first led to a classification of all known mesons and baryons, and later to the proposal of the existence of new fundamental particles – quarks. The observation was that it is possible to represent all hadrons with equal spin and parity in an irreducible representation of the group $SU(3)_F$. They are described completely by their quantum numbers I_3 and Y, where I_3 denotes the third component of the (strong) isospin and Y is the strong hypercharge. Both can be combined to form the electric charge Q [2]:

$$Q = I_3 + \frac{1}{2}Y \tag{2.1}$$

The hypercharge is defined as the sum of baryon number B and strangeness S:

$$Y = B + S \tag{2.2}$$

At that time the known hadrons could be constructed with the three quark flavours up (u), down (d) and strange (s). They could be identified with the irreducible representation of lowest dimension of $SU(3)_F$, i.e. the triplet [3], which cannot be related to known hadrons. Thus, all hadrons could be described as bound quark states. This description is called quark model. So, mesons ($B = 0$) are bound states of a quark with an antiquark, and baryons ($B = 1$) can be described as bound states of three quarks (see figure 2.1).

[1] Sea quarks and gluons are neglected for the moment.

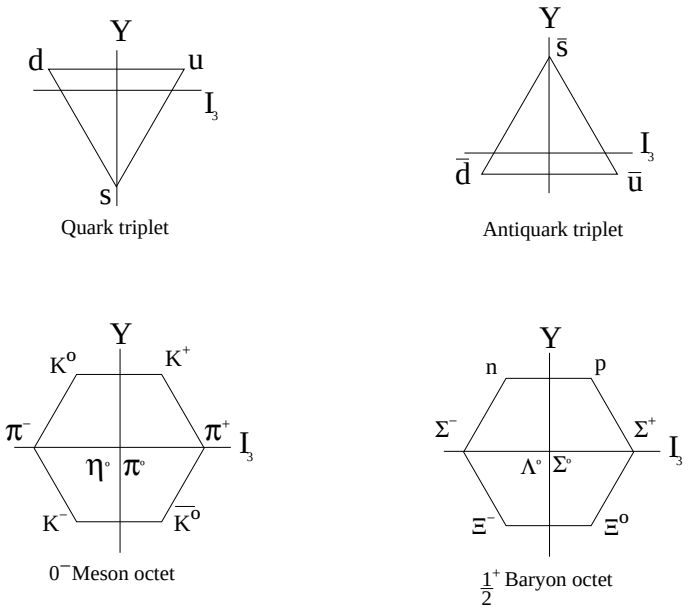

Figure 2.1: *Example for particle multiplets in the $SU(3)_F$ quark model.*

Today, three more quarks are known: charm (c), bottom (b), also called beauty in spectroscopy, and top (t). As these quarks have large masses hadrons containing these quarks cannot be well described by higher dimensional symmetries. An overview over the different quarks and their additive quantum numbers is given in table 2.1. All six quarks have spin 1/2 and baryon number 1/3. By convention, each quark has positive parity. Thus, each antiquark must have negative parity.

2.1.1 MESONS: $q\bar{q}$-STATES

As already mentioned, mesons are bound states of a quark q and an antiquark $\bar{q}'$ (the flavours of q and $\bar{q}'$ can be different). If the orbital angular momentum of the $q\bar{q}$-system is L, the

	quark					
quantum number	u	d	c	s	t	b
el. charge Q	+2/3	-1/3	+2/3	-1/3	+2/3	-1/3
3rd isospin component I_3	+1/2	-1/2	0	0	0	0
charm C	0	0	+1	0	0	0
strangeness S	0	0	0	-1	0	0
topness T	0	0	0	0	+1	0
bottomness B	0	0	0	0	0	-1

Table 2.1: *Additive quantum numbers of quarks. The sign of C, S, T and B is by convention the same sign as the electric charge of the quark.*

total spin is S with $S = 0, 1$ and the total angular momentum is J with $J = L \oplus S$, then the parity P and charge conjugation C is given by

$$P = (-1)^{L+1} \quad , \quad C = (-1)^J. \tag{2.3}$$

The states with $L = 0$ are called pseudoscalar ($J^P = 0^-$) and vector mesons ($J^P = 1^-$) respectively. According to this, states in the normal spin-parity series, $P = (-1)^J$, must have $S = 1$ and hence $CP = +1$. That means that mesons with normal spin-parity and $CP = -1$ are forbidden in the quark model. The state with $J^{PC} = 0^{--}$ is forbidden as well. Mesons with such J^{PC} would lie outside the additive quark model [4].

For a fixed J^{PC}, there are nine possible $q\bar{q}$-combinations containing u-, d- and s-quarks. They group in an octet and a singlet according to the $SU(3)_F$-symmetry:

$$\mathbf{3} \otimes \bar{\mathbf{3}} \quad = \quad \mathbf{8} \oplus \mathbf{1} \quad . \tag{2.4}$$

Figure 2.1 (bottom left) shows the 0^--octet. The combination at the edge can be directly identified as mesons while this is not possible for $q\bar{q}$-combinations with the same flavour, since states with the same IJ^P (I = isospin) and the same additive quantum numbers can mix. Thus, the $\pi^0 (= \frac{1}{\sqrt{2}}(u\bar{u} - d\bar{d}))$ and the $\eta^0 (= \frac{1}{6}(u\bar{u} + d\bar{d} - 2s\bar{s}))$ are mixtures of those combinations. The singlet is the totally symmetric combination and can be identified with the η' [5]. The η and the η' do also mix because of the same quantum numbers.

2.1.2 Baryons: qqq-States

All the established baryons are three quark states (qqq). Those containing only u-, d- and s-quarks can be divided into a decuplet, two octets and a singlet:

$$\mathbf{3} \otimes \mathbf{3} \otimes \mathbf{3} \quad = \quad \mathbf{10}_S \oplus \mathbf{8}_M \oplus \mathbf{8}_M \oplus \mathbf{1}_A \tag{2.5}$$

Here, S indicates symmetric, M mixed-symmetric and A antisymmetric states under interchange of any two quarks. By convention, the parity of the proton is +1. Therefore the parity of the other baryons is given by:

$$P \quad = \quad (-1)^L \quad , \tag{2.6}$$

where L denotes the sum of the relative angular momenta of quark 2 around quark 1 and of quark 3 around the quark pair (1,2) [6].

There is no ground state baryon that could be assigned to the singlet because this would violate Pauli's principle. The $1/2^+$-octet of the ground state is shown in figure 2.1 on the bottom right. The ground state decuplet has $J^P = 3/2^+$.

2.2 Quantum Chromodynamics (QCD)

The quark model has some weaknesses which led to its replacement by a new theory: the Quantum Chromodynamics. The maybe best known example for that is the Δ^{++}-paradox. The Δ^{++} is a baryon with spin 3/2 and therefore consists of three u-quarks with the same spin orientation. Thus, it is a totally symmetric state which violates Pauli's principle stating that two fermions cannot occupy the same state. This problem has been solved by the introduction of a new quantum number which is carried by quarks. This quantum number is called 'colour'.

In this way, one can achieve that the quarks occupy different states. Three colours are needed for that. They are called r (red), g (green) and b (blue). As this quantum number could not be observed, hadrons are singlets with regard to the QCD symmetry $SU(3)_C$ (colour singlets).

Moreover, the quark model cannot explain why mesons and baryons are the only stable (or relative long-living) quark states. Other quark-antiquark or quark-quark combinations are stable as well in this model. This is not the case in QCD. Recently, there have been experimental hints for the existence of pentaquarks, a combination of (at least) four quarks and an antiquark decaying in mesons and baryons [7].

2.2.1 Gluons - the Gauge Bosons of QCD

QCD is a gauge field theory describing the strong interactions of coloured quarks and gluons. Gluons are the gauge bosons of this theory. As its symmetry group is $SU(3)_C$, a non-Abelian group, the gluons itself carry colour and therefore interact with each other. They span the $\mathbf{3} \otimes \bar{\mathbf{3}}$ colour space which would lead to nine different types of gluons. But they build an octet and a singlet. The gluons of the octet can be identified as the gauge bosons. The singlet does not exist because the $SU(3)_C$ group has only eight generators. The fact that strong interactions have only a scope of one femtometer, is evidence for this. If the singlet gluon existed it would cause a force of infinite range as it would couple to other colour singlets - the hadrons - and not to the quarks [5]. The transmission of the eight coloured gluons also involves net transmission of colour. Hadrons are colour-singlet combinations of quarks, antiquarks and gluons.

2.2.2 Asymptotic Freedom and Confinement

Analogously to the reduction of an electric field of a point-like charge by the dipoles of a dielectric liquid, a colour charge experiences a reduction by the production of virtual quark-antiquark pairs by vacuum fluctuations. One measures a larger colour charge the closer one gets. But the fact that gluons carry colour as well causes a converse effect: the effective colour charge becomes smaller the closer one gets because the quarks radiate virtual gluons and can thus change their colour. So, the effective charge and the coupling constant depend on the distance and therefore also on the energy μ. This phenomenon complicates calculations in QCD (gauge theories in general) for higher order corrections. In first order, the strong coupling constant α_s is:

$$\alpha_s(\mu) = \frac{4\pi}{(11 - \frac{2}{3}N_F)\ln(\mu^2/\Lambda^2_{QCD})} \quad . \tag{2.7}$$

Here, Λ_{QCD} denotes a fundamental parameter of QCD, the asymptotic scale parameter which has to be determined in experiments. N_F is the number of quark flavours with masses smaller than μ. It follows from equation (2.7) that $\alpha_s \to 0$ for $\mu \to \infty$. This behaviour is called *asymptotic freedom*. It makes the use of perturbation theory possible for large momentum transfers because the coupling constant is small in this region. $\alpha_s \to \infty$ applies to $\mu \to 0$. This behaviour, called *confinement*, is the reason that free, colour-charged particles cannot be observed. Quarks are confined into hadrons.

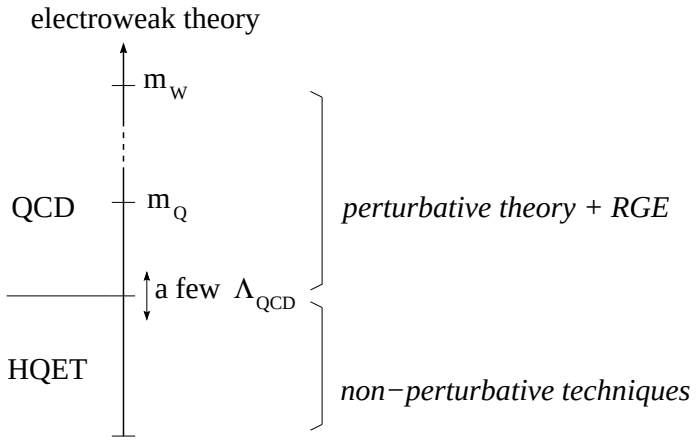

Figure 2.2: *Scope of HQET.*

2.2.3 Symmetries in QCD

There are a few cases where it is possible to make predictions for the non-perturbative region of QCD by using analytic methods. This is based on several symmetries of QCD.

Isospin symmetry: The isopin symmetry SU(2) was the first symmetry discovered. It is not an exact symmetry and arises because the difference of the light quark masses $m_d - m_u$ is small against Λ_{QCD}. If this difference was zero the predictions based on this symmetry would be exact. Corrections to the limit $m_d - m_u = 0$ can be studied in an expansion in the small parameter $(m_d - m_u)/\Lambda_{QCD}$. $\mathrm{SU(3)_F}$ symmetry is similar but the corrections are larger since $(m_s - m_u)/\Lambda_{QCD}$ is not small. If the isospin symmetry was exact there would be degenerate multiplets. Examples for isospin multiplets are:

$$\begin{pmatrix} p \\ n \end{pmatrix} \quad \text{und} \quad \begin{pmatrix} \pi^+ \\ \pi^0 \\ \pi^- \end{pmatrix}.$$

Chiral symmetry: The chiral symmetry $\mathrm{SU(2)_L} \otimes \mathrm{SU(2)_R}$ arises because both m_d and m_u are small compared to Λ_{QCD}. It is associated with the separate conservation of vector and axial vector currents. Although this symmetry is spontaneously broken in nature the chiral perturbative theory can be applied. If one also considers the mass of the s-quark as small against Λ_{QCD} then $\mathrm{SU(3)_L} \otimes \mathrm{SU(3)_R}$ is the symmetry group.

Heavy quark symmetry: A heavy quark Q, i.e. a quark with a mass $m_Q \gg \Lambda_{QCD}$, takes no notice from the light quark(s) which is (are) bound with it in a hadron. The resulting symmetry is called *heavy quark symmetry*. From this, an effective theory of QCD can be constructed: the *Heavy Quark Effective Theory* (*HQET*) [8].

2.2.4 Heavy Quark Effective Theory (HQET)

The Heavy Quark Effective Theory is a limit of QCD for $m_Q \to \infty$ and for a fixed velocity of the heavy quark v_Q^μ. It simplifies the description for energies smaller than m_Q and thus

for distances in the order of $1/\Lambda_{QCD}$. This allows for model independent predictions in the confinement region. For small distances, predictions can be made by using perturbative theory and the Renormalisation Group Equations (RGE) of QCD (see figure 2.2) [9].

The starting point in the construction of HQET is the observation that a heavy quark bound inside a hadron moves approximately with the same velocity v^μ as the hadron. Its momentum can be written as:

$$p_Q^\mu = m_Q v^\mu + k^\mu \quad , \tag{2.8}$$

where the components of the residual momentum k are much smaller than the mass of the heavy quark m_Q. Interactions of the heavy quark with the light degrees of freedom change the residual momentum by an amount of order $\Delta k \sim \Lambda_{QCD}$, but the corresponding changes in the velocity of the heavy quark vanish as $\frac{\Lambda_{QCD}}{m_Q} \to 0$. Thus, fluctuations of the heavy quark can be neglected.

The heavy quark symmetries appearing in HQET are the *Heavy Quark Flavour Symmetry* and the *Heavy Quark Spin Symmetry* [11].

Heavy Quark Flavour Symmetry: There is no change in the behaviour of the light quarks when replacing a heavy quark with another one with the same velocity v. The flavour symmetry originates from the fact that the effectice Lagrange density in the limit of $m_Q \to \infty$ is independent of m_Q and therefore independent of the flavour. It can be compared to the same chemical behaviour of a chemical element's isotopes.

Heavy Quark Spin Symmetry: The spin of the heavy quark decouples since the interactions with gluons do not change it. The only appearing interactions are due to relativistic effects which vanishes for $m_Q \to \infty$. The spin symmetry is analogous to the degeneration of the hyperfine levels in atoms for $\frac{m_e}{m_N} \to 0$.

Due to these symmetries, the heavy quark can be considered a static colour source. The first order corrections are proportional to $1/m_Q$. Thus, the prediction for the mass of a hadron containing a heavy quark is:

$$m_H = m_Q + \bar{\Lambda} + \frac{\Delta m^2}{2m_Q} + \mathcal{O}\left(\frac{1}{m_Q^2}\right) \quad , \tag{2.9}$$

with $\bar{\Lambda}$ denoting all terms independent of m_Q and Δm^2 the corrections due to the kinetic energy of the heavy quark bound in the hadron and due to the interaction of its spin with the colour field (chromo-magnetic interaction) [9].

2.2.5 Potential Models

Another possibility to predict hadron properties, as e.g. their mass, is the use of quark potential models. But they cannot be deduced from QCD because the actual QCD potential is unknown albeit the general behaviour is known (see section 2.2.2). Different potentials are used for different problems. Some examples for potential models often used are given in table 2.2. Potential models are very successful for systems containing heavy quarks, especially for charmonium ($c\bar{c}$) and bottomonium ($b\bar{b}$) states since non-relativistic approaches are

authors	potential
Eichten [12]	$V = -\frac{4}{3}\frac{\alpha_S}{r} + ar$
Quigg, Rosner [13]	$V = a\ln(r/r_0)$
Martin [14]	$V = A + Br^{0,1}$
Buchmüller [15]	$V = -\frac{4}{3}\frac{1}{(2\pi)^3}\int d^3q\ \exp(i\vec{q}\vec{r})\frac{4\pi\alpha_S(\vec{q}^2)}{\vec{q}^2}$

Table 2.2: *Potentials for different models.*

justified[2]. This is not true for systems containing light quarks since the spin-spin interactions cannot be assumed to be small. This can be seen e.g. in the ρ-π-system: the pion has spin 0 with a mass of 140 MeV/c^2 while the ρ-meson has spin 1 with a mass of 770 MeV/c^2.

2.3 Hadron Production in Z^0-Decays

When a Z^0-boson, produced in an electron-positron collision, decays into a $q\bar{q}$-pair, many observable particles are produced. Such events are called *multihadronic events* where twenty charged particles can be detected on average and additionally neutral ones, mainly photons. The particles emerge bundled in *jets*. The evolution of a multihadronic Z^0-decay is described by a model which accurate calculated parton[3] cross-sections, phenomenological algorithms and a lot of measured properties of hadron decays enter. The production of hadrons (*fragmentation* or *hadronisation*) takes place in the regime of non-perturbative QCD and can therefore only be described by models so far. The process $e^+e^- \rightarrow$ hadrons can be divided into four phases (see figure 2.3):

(I) the production of a $q\bar{q}$-pair governed by electroweak interactions,

(II) the phase of perturbative QCD,

(III) the hadron production (non-perturbative QCD) and

(IV) the decay into final state particles which are detectable.

2.3.1 Quark-Antiquark Pair Production

The process $e^+e^- \rightarrow q\bar{q}$ proceeds in first order approximation by the exchange of a photon or a Z^0-boson. There are three contributions to the cross-section of this process: one term describes the photon exchange, one the Z^0-exchange and the third the γ-Z^0 interference. All three terms are modified by higher-order corrections as virtual corrections (vertex and propagator corrections) and initial as well as final state radiation. The dependence of the hadronic cross-section on the centre-of-mass energy $\sqrt{s}$ and the contributions of the three terms are illustrated in figure 2.4. At a centre-of-mass energy corresponding to the mass of the Z^0-boson, the Z^0-exchange dominates. Thus, the relative production rates of the different

[2] If the charmonium system is described with the potential $V = -\frac{4}{3}\frac{\alpha_S}{r} + ar$ one gets $v^2/c^2 \simeq 0.4$.

[3] Quarks and gluons are combined under the expression 'parton'.

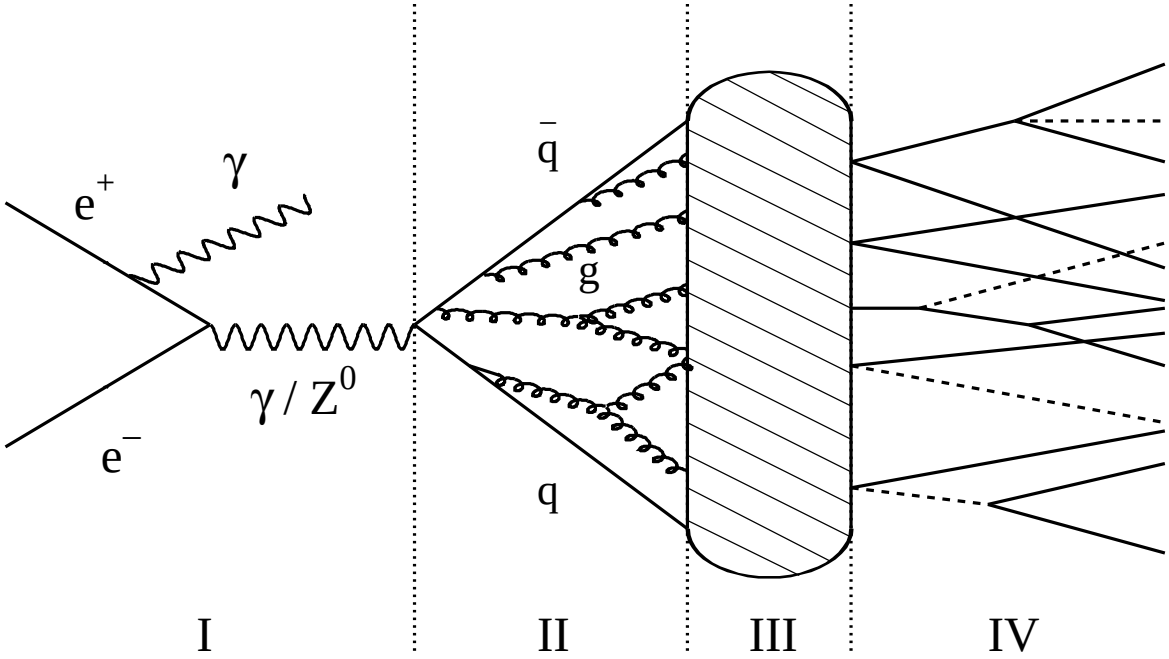

Figure 2.3: *The four phases of the process $e^+e^- \rightarrow$ hadrons: I) electroweak phase, II) perturbative QCD, III) fragmentation and IV) particle decays.*

fermions are given by the branching fractions of the Z^0:

$$\begin{aligned} BR(Z^0 \rightarrow l^+l^-) &\approx 10.1\%, \\ BR(Z^0 \rightarrow \nu\bar{\nu}) &\approx 20.0\%, \\ BR(Z^0 \rightarrow q\bar{q}) &\approx 69.9\%. \end{aligned} \tag{2.10}$$

The decay into neutrinos is experimentally not accessible due to their extremely weak interactions. Up-type quarks (u,c) are produced with a relative fraction to all quarks produced of about 17% and down-type quarks (d, s, b) are produced with a relative rate of 22%. Overall, only about 15% of the Z^0-bosons produced at LEP decay into a $b\bar{b}$-pair.

Due to the behaviour of the strong coupling constant α_s described in section 2.2.2, the transition from quarks to hadrons is subdivided into two phases, characterised by different energy scales.

2.3.2 The Perturbative Phase

Starting from the produced quark-antiquark pair a configuration of colour-charged quarks and gluons is produced by perturbative QCD processes. This is implemented in established Monte Carlo models by two approaches. The first method is the complete second order QCD matrix element calculation, and the second is the parton shower approach in leading log approximation.

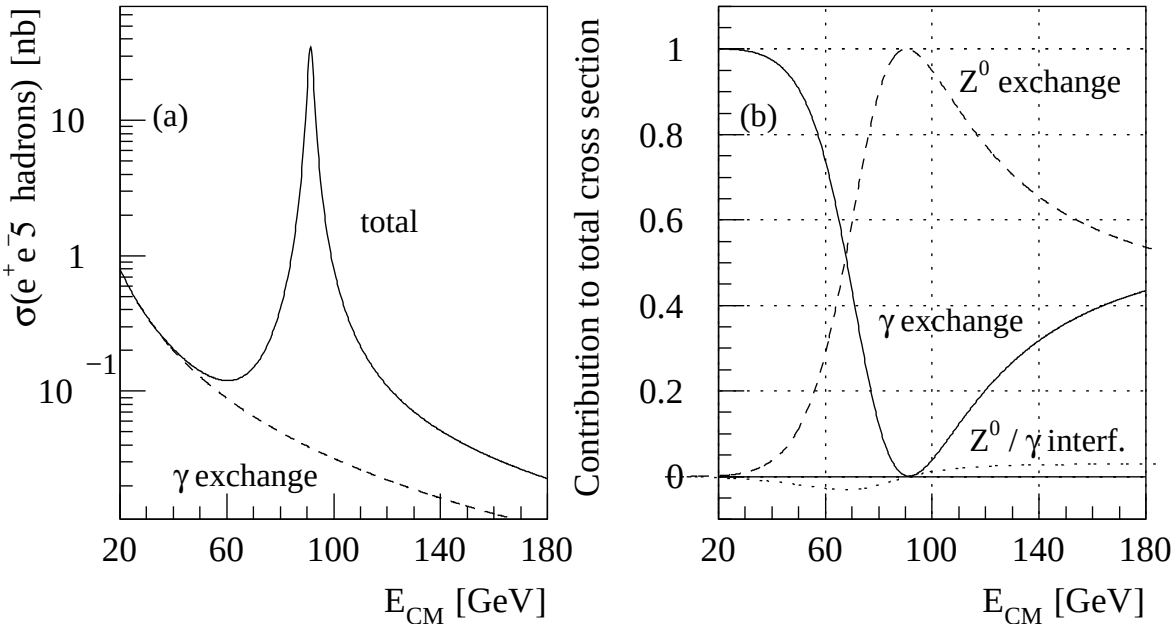

Figure 2.4: *a) The dependence of the total hadronic cross-section on the centre-of-mass energy. b) The relative contributions of the γ/Z^0-exchange and the γ-Z^0 interference to the total cross-section.*

QCD Matrix Elements

The first order term of the annihilation process $e^+e^- \rightarrow q\bar{q}$ is modified by the possible gluon radiation of coloured quarks. In this order, one gets a maximum of four partons in the final state, i.e. the following final states can be described: $e^+e^- \rightarrow q\bar{q}$, $e^+e^- \rightarrow q\bar{q}g$, $e^+e^- \rightarrow q\bar{q}q\bar{q}$ and $e^+e^- \rightarrow q\bar{q}gg$.

Parton Shower Model

In order to calculate multi-parton final states a vast number of Feynman diagrams[4] has to be considered. An alternative to these calculations is available in terms of the leading log approximation. In this approach only the leading terms of the perturbative expansion are kept, thus neglecting non-leading terms. The parton shower model is based on the picture of a time ordered cascade of subsequent splitting processes of the partons $q \rightarrow qg$, $g \rightarrow q\bar{q}$ and $g \rightarrow gg$. The evolution of the shower is stopped when an energy scale of $Q_0 \approx 1$ GeV is reached. Interference effects of higher order are included by the angular ordering of the radiated gluons.

The main difference between these two approaches is that the first is restricted to a maximal number of four partons while the second produces multi-gluon events with an average of nine (comparably soft) gluons per Z^0-event.

[4]Some of them are not easily solvable.

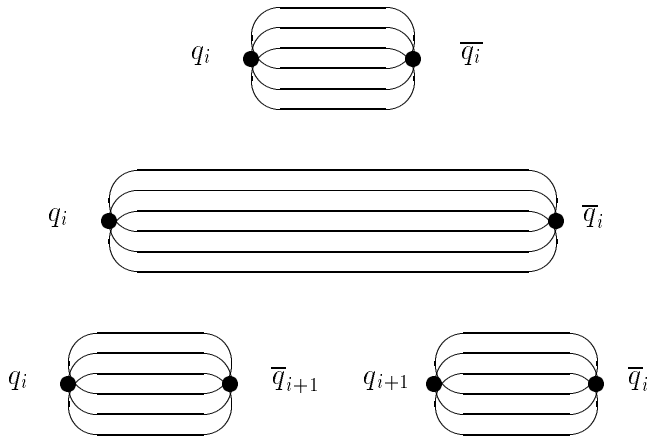

Figure 2.5: *Schematic figure of the string fragmentation. The quarks in the primary $q\bar{q}$-pair depart from each other leading to an increase of the string's energy with the distance until the string breaks and another $q\bar{q}$-pair is created. This process can be iterated with the subsystems.*

2.3.3 Fragmentation

Fragmentation or hadronisation describes the production of colourless hadrons from colour-charged quarks and gluons. It is not perturbatively accessible due to the large strong coupling constant in this region. Therefore phenomenological models have to be used for the description of this phase. For models using matrix elements, a considerably bigger range has to be covered since the typical energy scale for a maximum number of four partons is larger than for parton shower models. The existing fragmentation models are based on different physical assumptions. In order to describe real data a lot of free paramters are introduced in these models which have to be adjusted. The model of *string fragmentation* is very successful in the description of experimental results [16].

The phenomenon of confinement leads to the idea of a string connecting two colour-charged partons which underlie this model. The energy density in a colour field is constant and is $\kappa \approx 1$ GeV/fm. This leads to a potential increasing linearly with the distance. The simplest configuration is composed of a $q\bar{q}$-pair whose constituents depart from each other (see figure 2.5). As soon as the energy accumulated in the colour field is large enough the string breaks, creating a $q\bar{q}$-pair. Here, the generated $q\bar{q}$-systems obtain a fraction z and $1-z$ respectively of the sum of energy and longitudinal momentum. These pairs can create a meson or repeat the whole process. The probability distribution for z is given by the longitudinal fragmentation function $f(z)$. This function is described by different empirical functions for light (u, d, s) and heavy quarks (c, b) in Monte Carlo generators. The parameters have to be extracted from data. But recent measurements give evidence that the fragmentation function for b-quarks can also be described by the same function as for light quarks [17].

The maximum of the fragmentation function of heavy quarks is clearly localised at higher values of z compared to the one of light quarks (see figure 2.6). This is called "hard fragmentation" and brings about the fact that the hadron containing the primary heavy quark holds a bigger part of the beam energy. Heavy quarks are almost only generated in the perturbative phase or in the weak decay chain $b \rightarrow c$ and hardly ever in the fragmentation. This is given by a quark mass dependent probability similar to the one in the tunnel effect since the quarks

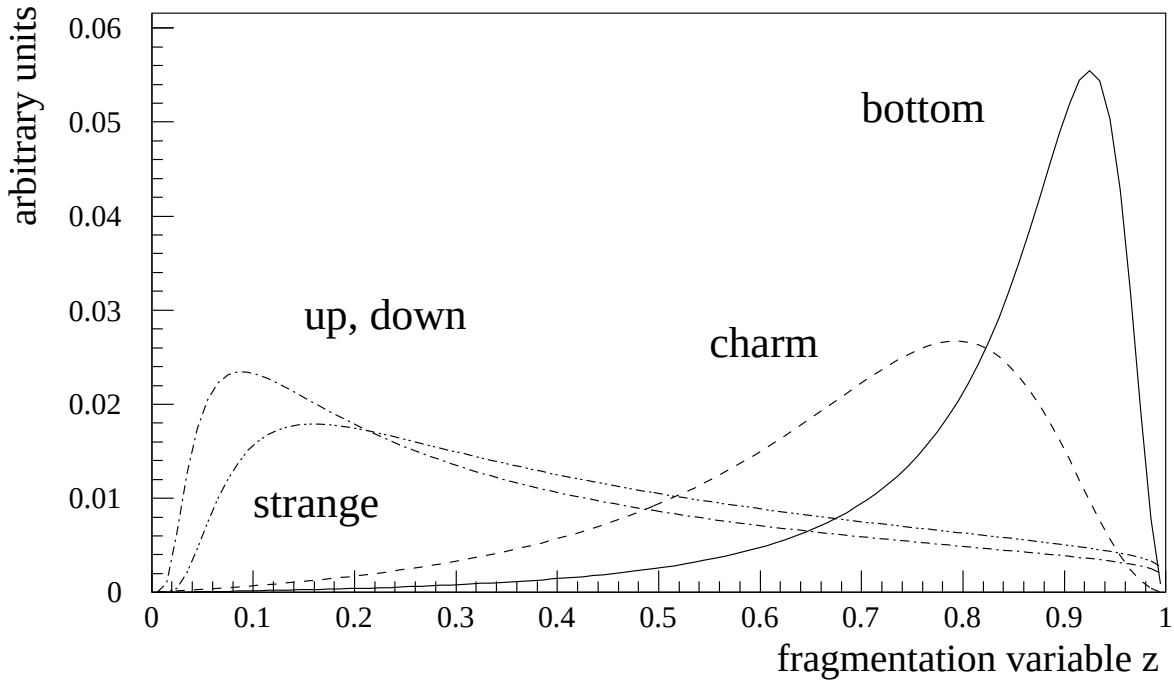

Figure 2.6: *Fragmentation function for different quark flavours.*

must be created in a certain distance from each other due to energy conservation [18]. The relative rates are approximately:

$$u : d : s : c : b \approx 1 : 1 : 0.3 : 10^{-11} : 10^{-100}. \tag{2.11}$$

In Monte Carlo models this is regulated by parameters adjusted to data. To generate baryons in this process the production of diquark pairs ($D\bar{D}=q_1q_2\bar{q}_1\bar{q}_2$) are introduced in the model. A baryon-antibaryon pair is created by combining these diquarks with neighbouring quarks. The production of diquark pairs is also controlled by parameters. In addition to the creation of adjacent baryons in the string it is possible to generate a $q\bar{q}$-pair and thus produce a meson in between the diquark pair so that the baryon pairs are not next to each other in the fragmentation chain. This process is called *popcorn effect*.

Gluons are treated as transverse excitations of the string in the string model. They are situated at the end of two strings due to their colour composition. In a $q\bar{q}g$-configuration one string goes from the quark to the gluon and a second one from the gluon to the antiquark.

2.3.4 Particle Decays

The hadrons created during the fragmentation are either stable or they decay (directly or in cascades) to such particles. Known experimental results are used in the Monte Carlo generators. For states with unknown decay channels, predictions and measurements in similar systems are consulted. This is especially true for hadrons containing a b-quark. Decays of short-living particles are simulated in the Monte Carlo generator, particles with a longer lifetime decay in the detector and are simulated in the simulation of the detector response.

Chapter 3

B-Spectroscopy

For a meson consisting of a heavy (in this case a b-) and a light quark, the first takes on the part of the nucleus and the latter the part of the electron in a hydrogen atom. The hyperfine splitting in an atom occurs due to the interaction of the magnetic moment of the nucleus with the magnetic moment of the electron. In heavy-light mesons the reason for the splitting is the different orientation of the heavy quark's spin. HQET predicts the separated conservation of this spin and the total angular momentum of the light quark j_q for $m_Q \to \infty$. Each energy level of the $\bar{\mathrm{Q}}\mathrm{q}$ meson thus consists of a pair of states labelled by j_q and the total angular momentum J. In the heavy quark limit, the pair is degenerate in mass and the states have the same strong interaction width. The degeneracy of the states is expected to be broken by hyperfine splitting effects. This leads to the following mass formula for the states within a doublet [10] which are denoted by H_+ and H_- respectively,

$$m_{H_{(\pm)}} = m_Q + \bar{\Lambda} - \frac{\lambda_1}{2m_Q} \pm \frac{n_{\mp}\lambda_2}{2m_Q} + \mathcal{O}\left(\frac{1}{m_Q^2}\right) \quad , \tag{3.1}$$

where $n_{\mp} = 2J_{\mp} + 1$ denotes the number of spin components for $H_{\mp}$. $\bar{\Lambda}$ is the energy of the light degrees of freedom in the $m_Q \to \infty$ limit. It is the same for both members of a spin symmetry doublet but of course different for different doublets. λ_1 denotes the kinetic energy term and λ_2 is the contribution of the chromo-magnetic interaction which is responsible for the hyperfine splitting within the doublet. λ_1 is independent of the heavy quark mass, λ_2 has a weak logarithmic dependence on m_Q. The spin averaged mass

$$\bar{m}_H = \frac{n_+ m_{H_{(+)}} + n_- m_{H_{(-)}}}{n_+ + n_-} \tag{3.2}$$

is independent of λ_2. The hyperfine splitting, i.e the difference in mass between the two members of a doublet determines λ_2:

$$m_{H_{(+)}} - m_{H_{(-)}} = \frac{n_+ + n_-}{2m_Q}\lambda_2 = \frac{2j_q + 1}{m_Q}\lambda_2 \tag{3.3}$$

3.1 Ground State B-Mesons

The total angular momentum of the light quark in the ground state is $j_q = 1/2$, and therefore J can be either 0 or 1. Thus, one gets a pseudoscalar ($J_P = 0^-$) and a vector meson

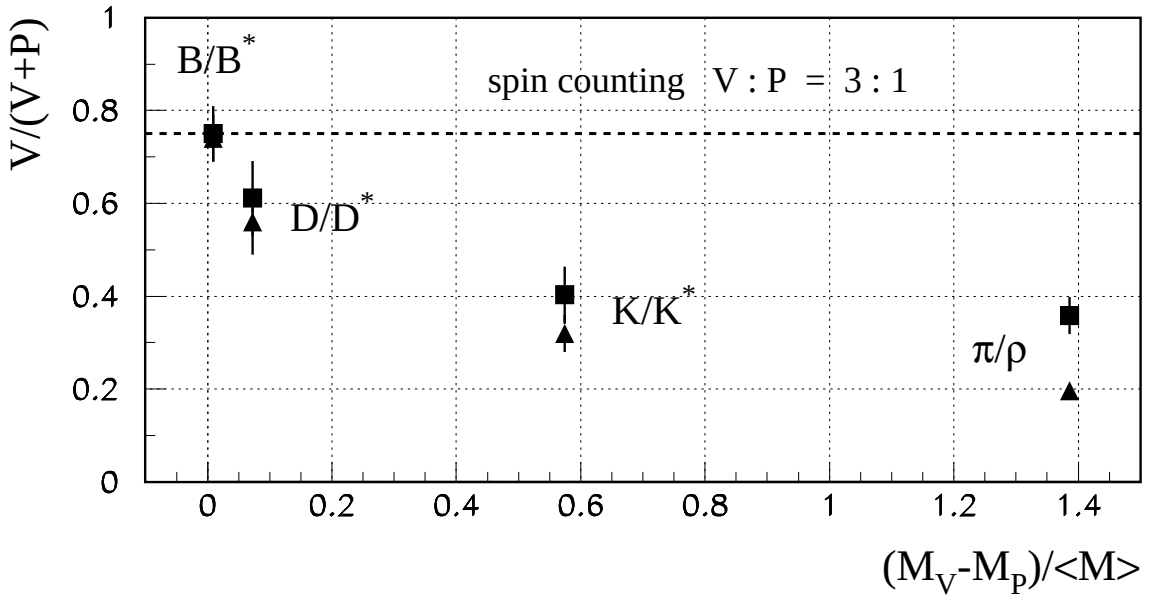

Figure 3.1: *The production fraction $V/(V+P)$ of the vector (V) and pseudoscalar mesons (P) as function of the ratio of the mass difference and the averaged mass at* LEP*. The triangles show the total production fraction of the primary and secondary produced mesons [4]. The squares indicate the same but the secondary mesons are subtracted using the JETSET 7.3 model [19] with the* DELPHI *tuning [20]. A suppression of the vector mesons can be observed for light mesons.*

($J^P = 1^-$). The vector meson has three possible spin orientations and is denoted as B* while the pseudoscalar meson is a spin singlet and denoted as B. Therefore simple spin counting (i.e. counting the possible spin states) predicts a production fraction of primary B*-mesons to B-mesons of 3:1. However, this method fails for light mesons (see figure 3.1). A suppression of the production of vector mesons can be observed for them.

The B*-meson decays electromagnetically as the mass difference between it and the B-meson is not large enough that a pion can be created [4]. The main decay channel is thus:

$$\mathrm{B}^* \to \mathrm{B}\gamma \quad . \tag{3.4}$$

The B-meson is the lightest meson containing a b-quark. Therefore it decays weakly, mainly into a D-meson[1] plus one or more other mesons. See [4] for the different possible decay modes.

3.1.1 HQET PREDICTIONS

For the ground state pseudoscalar and vector meson, one can parametrise the contributions from the kinetic energy and the chromo-magnetic interaction in the following way [21],

$$\Delta m^2 \;=\; -\lambda_1 + 2\left[J(J+1) - \frac{3}{2}\right]\lambda_2 \tag{3.5}$$

Thus, the parameters λ_1 and λ_2 can be determined by measuring the masses of B- and B*-mesons.

[1] A D-meson is a meson containing a c-quark and a light quark.

That the heavy-quark expansion can be applied is shown by experimental results: it predicts e.g. for the $SU(3)_F$ spin averaged mass splitting that [9]

$$\begin{aligned} \bar{m}_{\mathrm{B}_s} - \bar{m}_{\mathrm{B}_d} &= \bar{\Lambda}_s - \bar{\Lambda}_d + \mathcal{O}\left(\frac{1}{m_b}\right), \\ \bar{m}_{\mathrm{D}_s} - \bar{m}_{\mathrm{D}_d} &= \bar{\Lambda}_s - \bar{\Lambda}_d + \mathcal{O}\left(\frac{1}{m_c}\right), \end{aligned} \tag{3.6}$$

where it is indicated that the value of $\bar{\Lambda}$ depends on the flavour of the light quark. Thus, to the extent that the charm and the bottom quarks can both be considered sufficiently heavy, the mass splitting should be similar in the two systems. This prediction is confirmed experimentally, since

$$\begin{aligned} \bar{m}_{\mathrm{B}_s} - \bar{m}_{\mathrm{B}_d} &= 98.0 \pm 2.7 \text{ MeV/c}^2, \\ \bar{m}_{\mathrm{D}_s} - \bar{m}_{\mathrm{D}_d} &= 101.6 \pm 0.7 \text{ MeV/c}^2, \end{aligned} \tag{3.7}$$

using the masses given in [4].

As a second example, consider the spin splittings between the vector and pseudoscalar mesons for which HQET predicts:

$$m_{B^*}^2 - m_B^2 = m_{D^*}^2 - m_D^2 . \tag{3.8}$$

Using $m_{B^*} + m_B = 2m_b$ and $m_{D^*} + m_D = 2m_c$ respectively this can be rewritten as:

$$\frac{m_{B^*} - m_B}{m_{D^*} - m_D} = \frac{m_c}{m_b} . \tag{3.9}$$

Using the averaged splitting for the D-mesons of 141.4±0.1 MeV and the averaged splitting of the B-mesons of 45.78 MeV±0.35 [4], this is fulfilled quite well since the ratio of the quark masses $\frac{m_c}{m_b}$ is assumed to be approximately 1/3 [10, 22–24]. In this thesis, an analysis is presented measuring this splitting for the first time separately for charged and neutral B-mesons.

The good agreement of the HQET predictions and data shows that both b-quarks and c-quarks can be considered heavy quarks but the expectations from the heavy quark limit may have to be changed by $1/m_Q$-corrections to be comparable with the experimental results.

Interestingly, one can observe that the variable $\Delta = m^2(1-) - m^2(0-)$, which should be constant in heavy-light systems, is actually also a constant for light-light systems [25]. This is shown in table 3.1.

System	Δ [GeV^2]
(B^*,B)	0,53
(D^*,D)	0,54
(K^*,K)	0,55
(ρ,π)	0,57

Table 3.1: *The hyperfine splitting Δ for different meson systems. The table is taken from [25].*

Splitting	Exp. [4]	M1 [27]	M2 [28]	M3 [28]	M4 [29]
$K^0 - K^+$	3.995 ± 0.034 MeV	13.15 MeV	6.64 MeV	9.56 MeV	0.98 MeV
$K^{*0} - K^{*+}$	6.7 ± 1.2 MeV	1.55 MeV	1.36 MeV	1.28 MeV	0.15 MeV
$D^+ - D^0$	4.78 ± 0.10 MeV	5.37 MeV	3.78 MeV	-0.33 MeV	4.53 MeV
$D^{*+} - D^{*0}$	2.6 ± 1.8 MeV	2.44 MeV	2.74 MeV	-0.16 MeV	1.6MeV
$B^0 - B^+$	0.33 ± 0.28[a] MeV	-1.46 MeV	-1.29 MeV	-6.06 MeV	0.89 MeV
$B^{*0} - B^{*+}$	–	-2.04 MeV	-1.23 MeV	-5.26 MeV	-0.02 MeV

Table 3.2: *A comparison of isospin mass splittings for different potential models M1-M4.*

[a]Two out of four measurements are negative.

3.1.2 Predictions from Potential Models

The isospin splitting for different mesons and for different potential models is studied in [26]. The results are given in table 3.2. The models used are M1 [27], M2 (linear potential) [28], M3 (potential $\propto r^{2/3}$) [28] and M4 [29]. For the first three models, the mass difference of the u- and d-quark were fitted in such a way that the mass splitting in the proton-neutron system could be reproduced. Numerical calculations were used for the predictions of M4.

The results from QCD calculations on the lattice for the B^*-B splitting are not well compatible with the experimental results [30]. There is no lattice calculation known to the author where the B^{+*}-B^+ and B^{0*}-B^0-splittings are separately calculated.

3.2 Orbitally Excited B Mesons

Orbitally excited B-mesons are mesons with angular momentum $L = 1$. This gives a total angular momentum of the light quark of $j_q = 1/2, 3/2$. Combining the spin of the b-quark S_b with j_q leads to four different B^{**}-meson states with $J = 0, 1, 1$ and 2. Parity conservation limits the orbital angular momentum between the decay products L_p to be even values, and requiring that S_b and j_q are separately conserved results in the decay modes listed in table 3.3 for the four $B^{**}_{u,d}$-states. A similar pattern is expected for the B^{**}_s-states, although, in this case, isospin conservation demands that the only decay channels available are to $B^{(*)}K$ if the B^{**}_s-mass is above threshold. "(*)" denotes both the vector and the pseudoscalar ground states since both decays are possible depending on the particular B^{**}_s-state. The members

j_q	J^P	$B^{**}_{u,d}$-state	decay mode	width
1/2	0^+	B^*_0	$B\pi$	broad ($L_p = 0$, S-wave)
1/2	1^+	B^*_1	$B^*\pi$	broad ($L_p = 0$, S-wave)
3/2	1^+	B_1	$B^*\pi$	narrow ($L_p = 2$, D-wave)
3/2	2^+	B^*_2	$B^*\pi, B\pi$	narrow ($L_p = 2$, D-wave)

Table 3.3: *Properties of the four $B^{**}_{u,d}$-states. The same is valid for B^{**}_s-states. For these states the decay pion has to be replaced by a kaon if their mass lies above the BK-threshold.*

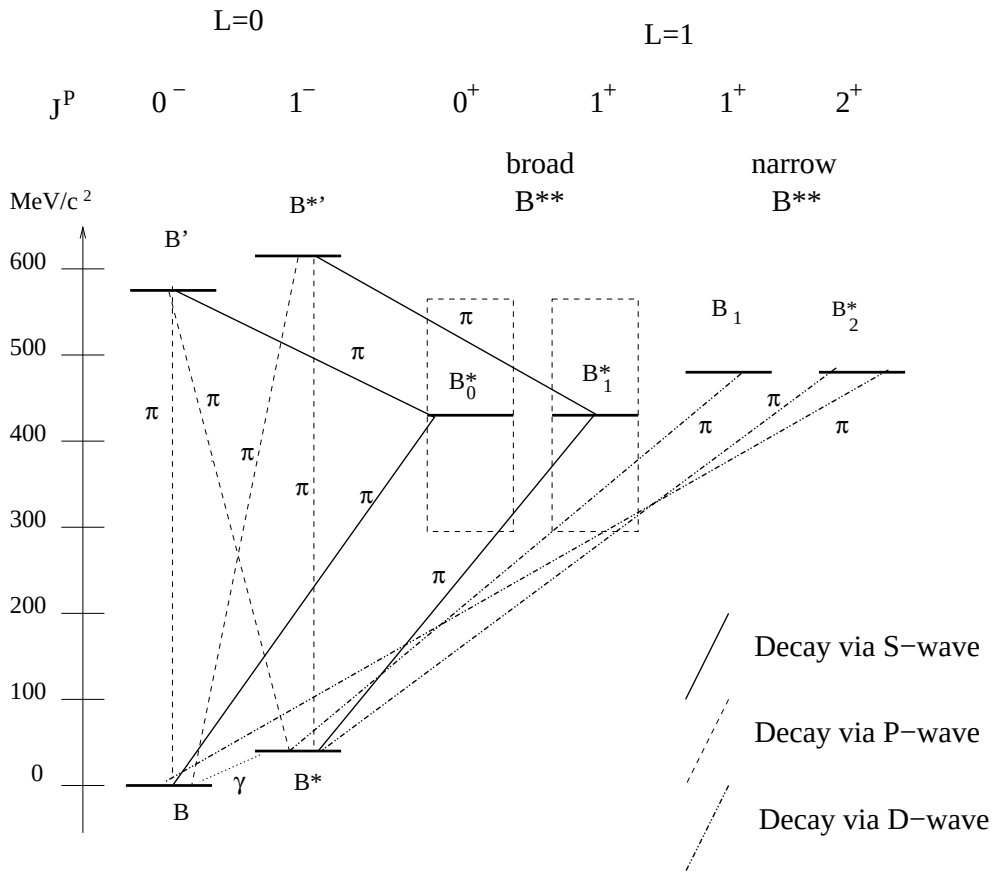

Figure 3.2: *Term diagram of $B_{u,d}$-mesons. Shown are the broad and narrow $B^{**}_{u,d}$-mesons and the radial excitations $B'_{u,d}$ and $B^{*\prime}_{u,d}$. Only the allowed decay modes via one pion and via S-waves ($L_p = 0$), P-waves ($L_p = 1$) and D-waves ($L_p = 2$) are shown. The possible decay modes via ρ-mesons and two pions have been omitted for clarity.*

of the $j_q = 3/2$ doublet are expected to be very narrow compared to typical strong decay widths since only the suppressed $L_p = 2$ (D-wave) transitions are allowed. They are called "narrow" states while the other two states are denoted "broad" states. In addition, counting the available spin states predicts the production ratio B^*_2:B_1:B^*_1:B^*_0 to be 5:3:3:1, while state counting predicts a production ratio of 1:1:1:1. The broad state with $J = 1$ is denoted B^*_1 throughout this thesis in order not to get confused with the corresponding narrow state although the proper notation is also B_1.

An overview over the different $B_{u,d}$-states is given in figure 3.2. It shows the decay modes via one pion for the first orbital and radial excitations of $B_{u,d}$- and $B^*_{u,d}$-mesons and their supposed or measured masses represented by the mass difference between the mass of the $B_{u,d}$-state considered and the B-mass. The B^{**}_s-mesons have been omitted for clarity in this figure. For them, the pion has to be replaced by a kaon. The narrow B^{**}_s-states should be placed around a mass difference of 570 MeV/c^2, the B_s-meson at 90 MeV/c^2 and the B^*_s-meson at approximately 135 MeV/c^2.

3.2.1 THEORETICAL EXPECTATIONS

The hyperfine splitting effect between the members of a B^{**}-doublet is supposed to be small. Various models (e.g. [23, 24, 31–36]) predict that the mass difference within the j_q=1/2 and the j_q=3/2 doublets should be approximately equal and in the range 5 – 20 MeV/c^2. This effect, together with the B^*-B-mass splitting, means that the narrow states are expected to produce three single peaks in the Q-value[2] space, since the B_2^*-state can decay in either $B^*\pi$ or $B\pi$ final states. The ratio of the branching fractions of the B_2^*-meson is proportional to the ratio of the corresponding pion momentum in the B_2^*-rest frame to the fifth power. It is expected to have a value around one for $B_{u,d}^{**}$ [31]. Since the B_{s2}^* is supposed to be near the threshold its ratio of the branching fractions is expected to be approximately equal to the ratio of the kaon momenta in the B_{s2}^*-rest frame to the fifth power, i.e. $\approx 1/10$.

Although the models roughly agree on the size of the narrow state mass splitting, they do not agree on the hierachy of the $B_{u,d}^{**}$-masses. Some models [32, 33] predict the broad states to lie lower in mass than the narrow ones. Here, the splitting between the B_1 and B_1^* is of order 10 MeV/c^2. Others [23, 34] predict a 'spin-orbit inversion' effect where the broad states are higher in mass than the narrow states. In these models, the B_1^* has a mass which is up to 150 MeV/c^2 higher than the one of the B_1. The widths of the broad states are predicted to be between 200 and 300 MeV/c^2 [31, 34] and supposed to be approximately equal to those of the broad D-states.

Lattice calculations exist for the mass splittings between the B_2^*- and B_0^*-states for both $B_{u,d}^{**}$- and B_s^{**}-mesons. The results are wide spread, some results are compatible with zero or give a slightly negative splitting, some give a splitting larger than 100 MeV/c^2 [30] for both meson types. The results of the lattice calculations for the mass difference $m(B_2^*) - m(B)$ are between 420 and 530 MeV/c^2, for $m(B_0^*) - m(B)$ between 370 and 480 MeV/c^2, for $m(B_{s2}^*) - m(B_s)$ between 420 and 540 MeV/c^2 and for $m(B_{s0}^*) - m(B_s)$ between 280 and 530 MeV/c^2.

3.3 EXPERIMENTAL RESULTS

3.3.1 B^*-MESONS

The challenge in reconstructing B^*-mesons is the detection of the low energetic photon (see section 4.7). L3 [37] use their calorimeter with an energy resolution of $\approx 5\%$ in the interesting energy range. ALEPH [38], DELPHI [39] and OPAL [40] reconstruct photon conversions in front of the track chambers providing an excellent energy ($\approx$ 1-2%) and Θ-, Φ-resolution ($\approx$ 1-2 mrad). The results are summarised in table 3.4.

There is an upper limit from DELPHI for $|\Delta m(B^{*+} - B^+) - \Delta m(B^{*0} - B^0)| < 6$ MeV/c^2 and $|\Delta m(B_s^* - B_s) - \Delta m(B_{u,d}^* - B_{u,d})| < 6$ MeV/c^2 @ 95% C.L.

3.3.2 ORBITALLY EXCITED STATES

RESULTS IN THE CHARM SECTOR

The narrow $D_{u,d}^{**}$- and D_s^{**}-states are well established [4]. For the broad states, there has recently been some progress. CLEO presented evidence for the broad state D_1^* in the region

[2] The Q-value is defined as the difference in mass between the original particle and its decay particles.

	Experiment	Measurement
Δm[MeV]	ALEPH	45,3 ± 0,4 ± 0,9
	DELPHI	45,5 ± 0,3 ± 0,8
	L3	46,3 ± 1,9
	OPAL	46,2 ± 0,3 ± 0,8
	LEP average	45,7 ± 0,5
$\frac{\sigma_{B^*}}{\sigma_B+\sigma_{B^*}}$	ALEPH	0,77 ± 0,03 ± 0,07
	DELPHI	0,72 ± 0,03 ± 0,06
	L3	0,76 ± 0,08 ± 0,06
	OPAL	0,76 ± 0,04 ± 0,08
	LEP average	0,75 ± 0,04
$\frac{\sigma_L}{\sigma_L+\sigma_T}$	ALEPH	0,33 ± 0,06 ± 0,05
	DELPHI	0,32 ± 0,04 ± 0,03
	L3	–
	OPAL	0,36 ± 0,06 ± 0,07
	LEP average	0,33 ± 0,04

Table 3.4: *Results of the LEP experiments for B^*-mesons. The first row shows the measurements for the mass splitting, the second one the production fraction of the vector mesons $V/(V+P)$ and the last row shows the production fraction of longitudinal polarised states. The uniform distribution between longitudinal and transverse polarised states can be observe here.*

of the narrow resonances [41]. BELLE confirmed this result and also gave evidence for the other broad state, D_0^*, lying approximately 150 MeV/c^2 lower in mass [42]. In addition, BABAR and CLEO have recent evidence for two narrow states lying under the DK-threshold and therefore decaying into $D_s^+\pi^0$ [43]. The likely interpretation for these states is that they represent the broad D_{s0}^{+*}- and D_{s1}^{+*}-states[3]. An overview over these states is given in table 3.5.

Additionally, there are measurements [4, 42, 44] of the relative branching fraction of the neutral and charged D_2^*-meson, $\Gamma(D^+\pi^-)/\Gamma(D^{*+}\pi^-)$ and $\Gamma(D^0\pi^+)/\Gamma(D^{*0}\pi^+)$ respectively (see table 3.6). These results are all in the range of theoretical predictions lying in the interval [1.5:3] [24, 31].

There are no observations of the decays $D^{**} \to D\rho$, $D\pi^+\pi^-$.

For the D_{s2}^*, only a limit exists: $\Gamma(D^{0*}K^+)/\Gamma(D^0K^+) < 0.33$ [45].

Implications for the Beauty Sector

Using the results listed in table 3.5 and the m_c/m_b-scaling of the mass splitting within a doublet (see section 3.2), one can predict the corresponding difference in the beauty sector. Thus, one gets for the difference a value of about 12 MeV/c^2 within the narrow $B_{u,d}^{**}$-doublet, the splitting of the broad doublet is of order 45 MeV/c^2 and the one of the narrow B_s^{**}-doublet is also about 12 MeV/c^2. The measurements do not support the idea of spin-orbit inversion.

[3] They would be broad if they could decay into DK

	Meson	Mass [MeV/c^2]	Width [MeV/c^2]
World Av.	D_2^0	2458.9 ± 2.0	23 ± 5
World Av.	D_2^+	2459 ± 4	25^{+8}_{-7}
World Av.	D_1^0	2422.2 ± 1.8	$18.9^{+4.6}_{-3.5}$
World Av.	D_1^+	2427 ± 5	28 ± 8
CLEO	D_1^{0*}	2461 ± 50	290 ± 100
BELLE	D_1^{0*}	2427 ± 36	384 ± 117
BELLE	D_0^{0*}	2308 ± 36	276 ± 66
World Av.	D_{sJ}^+	2572.4 ± 1.5	15^{+5}_{-4}
World Av.	D_{s1}^+	2535.34 ± 0.31	< 2.3

Table 3.5: *Current world results for masses and the widths of D^{**}-states.*

The results for the relative branching ratio of D_2^* can be used to make a prediction of the one of B_2^*, once the mass of it is known. The ansatz chosen for that calculation was:

$$\Gamma(D_2^* \to D\pi)/\Gamma(D_2^* \to D^*\pi) = F\left(\frac{k_D}{k_{D^*}}\right)^5 \quad (3.10)$$

$$\Gamma(B_2^* \to B\pi)/\Gamma(B_2^* \to B^*\pi) = F\left(\frac{k_B}{k_{B^*}}\right)^5 \quad (3.11)$$

where k_D and k_{D^*} denote the momentum of the pion in the rest frame of the D_2^* in the decay $D_2^* \to D\pi$ and $D_2^* \to D^*\pi$ respectively and analogously for the B-case. F denotes the ratio of the form factors of the two decays which is assumed to be equal for the D_2^*- and B_2^*-states [31]. With $k_B = 412$ MeV/c and $k_{B^*} = 367$ MeV/c (using a B_2^*-mass of 5730 MeV/c^2) and $F = 0.61 \pm 0.16$, this results in $\Gamma(B_2^* \to B\pi)/\Gamma(B_2^* \to B^*\pi) = 1.1 \pm 0.3$

The results from BABAR and CLEO give a strong hint that the broad B_s^{**}-states could also lie below the BK-threshold.

Results in the Beauty Sector

Evidence for the existence of narrow $B_{u,d}^{**}$-states first emerged in analyses at LEP in which a charged pion produced at the primary event vertex was combined with an inclusively reconstructed B-meson [46]- [48]. In a subsequent analysis, the ALEPH Collaboration performed

	Meson	Relative BR
World Av.	D_2^{*0}	2.3 ± 0.6
BELLE	D_2^{*0}	1.9 ± 0.5
CLEO	D_2^{*+}	$1.9 \pm 1.1 \pm 0.3$

Table 3.6: *Current world results for relative branching ratios of D_2^*. The world average has been done without the BELLE measurement [4].*

	$m(B^{**}_{u,d})$ [MeV/c^2]	$\sigma(B^{**}_{u,d})/\sigma_b$
OPAL incl.	5712 ± 11	0.21 ± 0.05
DELPHI incl.	$5732 \pm 5 \pm 20$	$0.27 \pm 0.02 \pm 0.06$
ALEPH incl. (all)	$5734 \pm 3 \pm 16$	$0.214 \pm 0.012 \pm 0.045^{+0.030}_{-0.045}$
ALEPH incl.(peak)	$5734 \pm 3 \pm 16$	$0.144 \pm 0.008 \pm 0.030$
L3 incl.	$B^*_2 : 5768 \pm 5 \pm 6$	$0.32 \pm 0.03 \pm 0.06$
CDF semi-excl.	$B_1 : 5710 \pm 20$	$0.22 \pm 0.05 \pm 0.02$
ALEPH excl.	$B^*_2 : 5739^{+8+6}_{-11-4}$	$0.24 \pm 0.07^{+0.05}_{-0.04}$

Table 3.7: *Current world results for masses and production rates of narrow $B^{**}_{u,d}$-states.*

an analysis combining a primary charged pion with a fully reconstructed B-meson [49] and measured the mass and rate in a fit to the mass spectrum with fixed mass differences, widths and relative rates of all spin states according to the predictions of [36]. Subsequently the L3 Collaboration presented an inclusive measurement of the mass and width of the B^*_1- and B^*_2-states by a fit imposing constraints that reflect the level of understanding regarding the widths and masses of the B^{**}-states circa 1999 [50]. More recently, the CDF Collaboration have presented the first results on $B^{**}_{u,d}$-production from a hadron collider [51] by combining a charged primary pion to a partially reconstructed B using semileptonic decays to charm.

Table 3.7 summarises these measurements for the narrow (and possibly part of broad) $B^{**}_{u,d}$-states. In order to make a comparison possible, published numbers have been adjusted where possible to be valid for a common set of input parameters [52].

Experimental evidence for the B^{**}_s is less compelling than for the $B^{**}_{u,d}$ and, to date, OPAL [48] is the only collaboration reporting a significant signal. They see an excess over background of $149 \pm 31\, B^+K^-$ pairs with an invariant mass of 5853 ± 15 MeV/c^2, which translates into,

$$\frac{\sigma(B^{**}_s)}{\sigma_b} = 0.020 \pm 0.006$$

No experimental results currently exist concerning broad states in the B-system.

3.4 Spectroscopy of b-Baryons

About 90% of the primary b-quarks give mesons, the other 10% baryons. These heavy baryons are formed by the b-quark and a light diquark. The spin-parity quantum numbers j^P_q of the light diquark system are determined from the spin and orbital degrees of freedom of the two light quarks that make up the diquark. From the spin degrees of freedom of the light quarks, one obtains both spin-0- and -1-states. Its total orbital state is characterised by two angular degrees of freedom. The angular momentum L_k describes the relative orbital excitation of the two light quarks, and L_K describes the orbital excitation of the centre-of-mass of the two light quarks relative to the heavy quark as shown in figure 3.3.

Heavy baryons without any orbital excitation ($L_k = L_K = 0$) are built up from a heavy Quark Q with spin-parity $J^P_Q = 1/2^+$ and a light diquark system with spin-parity 0^+ or 1^+ respectively. When one combines the diquark spin with the heavy quark's spin one obtains

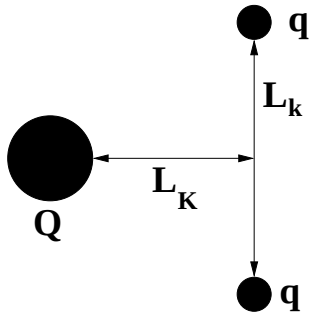

Figure 3.3: *Orbital angular momenta of a light diquark system bound to a heavy quark Q. L_k describes the relative orbital momentum of the two light quarks and L_K describes the orbital momentum of the centre-of-mass of the light quark relative to the heavy quark.*

the ground state heavy baryon Λ_b (which is quite well-known [4]) and the two excited states Σ_b/Σ_b^* according to the following coupling scheme:

$$\begin{aligned} 0^+ \otimes \frac{1}{2}^+ &\rightarrow J^P = \tfrac{1}{2}^+ \ : \ \Lambda_Q \\ 1^+ \otimes \frac{1}{2}^+ &\rightarrow J^P = \tfrac{1}{2}^+ \ : \ \Sigma_Q \\ &\rightarrow J^P = \tfrac{3}{2}^+ \ : \ \Sigma_Q^* \end{aligned}$$

3.4.1 Theoretical and Experimental Results

The two states Σ_Q and Σ_Q^* are exactly degenerate in the heavy quark limit since the heavy quark possesses no spin interaction with the light diquark system as $m_Q \rightarrow \infty$ (see sections 2.2.4, 3.1.1). First order corrections to this limit would be proportional to $1/m_Q$. A part of this thesis will focus on the search for the charged Σ_b- and Σ_b^*-baryons, with quark content (uub) for the $\Sigma_b^{(*)+}$ and (ddb) for the $\Sigma_b^{(*)-}$ and their antiparticles. They are expected to decay strongly:

$$\Sigma_B^{(*)\pm} \rightarrow \Lambda_b \pi^\pm \tag{3.12}$$

CLEO has measured the masses and widths of all $\Sigma_c^{(*)}$-baryons [54, 55]. The results are summarised in table 3.8. According to these results the splitting between the $\Sigma_c^{(*)}$-baryons is

Observable	$\Sigma_c^{0(*)}$	$\Sigma_c^{+(*)}$	$\Sigma_c^{++(*)}$
$m(\Sigma_c) - m(\Lambda_c^+)$[MeV/c^2]	167.2±0.1±0.2	166.4±0.2±0.3	167±0.1±0.2
$\Gamma(\Sigma_c)$[MeV/c^2]	2.4±0.2±0.4	< 4.6 (90% CL)	2.5 ±0.2±0.4
$m(\Sigma_c^*) - m(\Lambda_c^+)$[MeV/c^2]	232.6±1.0±0.8	231.0±1.1±2.0	234.5±1.1±0.8
$\Gamma(\Sigma_c^*)$[MeV/c^2]	$13.0^{+3.7}_{-3.0}$±4.0	<17 (90% CL)	$17.9^{+3.8}_{-3.2}$±4.0

Table 3.8: *CLEO results for $\Sigma_c^{(*)}$-baryons. The table is from [54].*

around 66 MeV/c^2. Thus, the splitting between the $\Sigma_b^{(*)}$-baryons is expected to be approximately 22 MeV/c^2 in the framework of HQET. Predictions from potential models [56] are also in the order of 30 MeV/c^2 but with a comparably huge error. They predict a difference in mass between the $\Sigma_b^{(*)}$- and Λ_b-baryon of about

$$m(\Sigma_b) - m(\Lambda_b) = 200 \pm 20 \text{ MeV/c}^2 \quad (3.13)$$

$$m(\Sigma_b^*) - m(\Lambda_b) = 230 \pm 20 \text{ MeV/c}^2. \quad (3.14)$$

Lattice calculations for the splitting between the two $\Sigma_b^{(*)}$-baryons come to similar results with values around 20 /MeV/c^2 [30].

Currently, there are no confirmed signals reported for $\Sigma_b^{(*)}$-states. DELPHI reported a signal for both states in 1995 with a production rate per b-jet of [18, 53]:

$$\frac{\sigma(\Sigma_b) + \sigma(\Sigma_b^*)}{\sigma_b} = 0.048 \pm 0.006(\text{stat}) \pm 0.015(\text{syst})$$

at a mass of 5797$\pm$17 MeV/c^2 and 5853$\pm$12 MeV/c^2 respectively and with a mass splitting of 56$\pm$17 MeV/c^2. One motivation for the $\Sigma_b^{(*)}$-analysis was to verify or falsify that observation by using improved and newly developed techniques.

Chapter 4

Experimental and Analysis Tools

Important tools and algorithms used in the analyses presented in this thesis are shortly described in this chapter as well as the experiment and the detector which took the data utilised in the years 1994 to 1998. The algorithms for inclusive B-reconstruction are discussed in chapter 5.

4.1 Artificial Neural Networks

To combine several variables in an appropriate way for separating two or more classes is an important task in most analyses. One way is to use linear, sequential cuts on each variable. But this does not take care of possible correlations between the variables. A better way is to define a single variable, which exploits all the existing information and correlations. This can be done by artificial neural networks, The most important type, also used in the analyses presented in this thesis, is the *multi-layer feed forward network* [57].

4.1.1 Multi-Layer Feed Forward Network

The functionality of this network type is shortly drafted in this section. More details as well as the description of other network types can be found in textbooks, e.g. in [57], or on the internet [58].

A multi-layer feed forward network consists of an input layer, an output layer and an arbitrary number of hidden layers (see figure 4.1). Each input node is assigned to an input variable. The nodes of two consecutive layers are catenated with each other by weighted connections. A weighted sum is calculated from the values of the previous layer. It is given to the transfer function whose value determines the output. The functionality of a node is shown in figure 4.2. Usually, a sigmoid function[1] is used as transfer function. The following output results for the output node i with the input vector $\vec{x}$ for a network with one hidden layer:

$$O_i(\vec{x}) \;=\; g\left(\sum_j W_{ij}\, g\left(\sum_k w_{jk}x_k + \Theta_j\right) + \Theta_i\right) \quad . \tag{4.1}$$

Here, w_{jk} denotes the weights from the input layer to the hidden one, Θ_j the threshold for the j-th node in the hidden layer, W_{ij} the weights from the hidden to the output layer,

[1] A sigmoid function is kind of a smooth step function with values in the interval $[-1, 1]$ or $[0, 1]$.

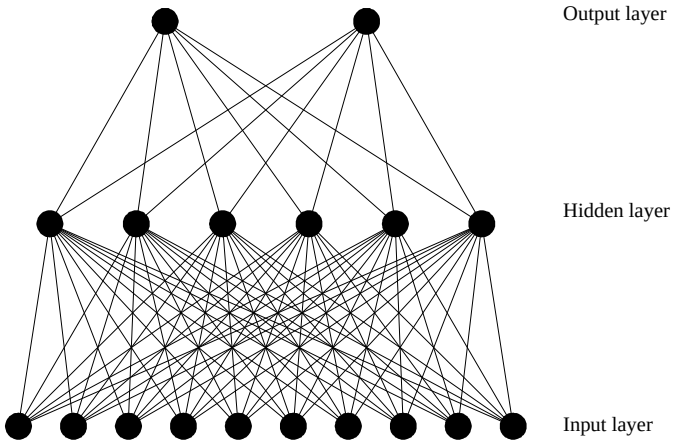

Figure 4.1: *Draft of a multi-layer feed forward network with ten nodes in the input layer, six nodes in the hidden layer and two output nodes.*

Θ_i the threshold of the output node i and g the transfer function. (The thresholds can be implemented by an additional node with a fixed value connected to each node in the consecutive layer, the bias node.) The output values represent discriminators for the different classes. For two classes, one output node is sufficient. The actual information is contained in the weights of the connections. Both these and the thresholds have to be determined in a training. This is made by the use of patterns for which it is known to which class an event belongs to (e.g. in Monte Carlo simulations). The target values of each output node are defined for each class. The weights are adjusted by minimisation of an error function. Widely used functions are the sum-of-squares error function, which is essentially given by summing up the square of the difference between the output and the target value assigned to the pattern considered, and the entropy error function, which is essentially given by the sum of the logarithms of the output values. The exact argument of the logarithm is a function of the target values assigned, but this function always has the advantage that the contribution of a totally wrong classification[2] of a pattern leads to an infinite contribution to the sum. To update the weights in every connection the contribution of each node to the total error has to be calculated. This is done with two formulae consolidated as the *general δ-rule* [59]. From that follows the change in the weights to minimise the total error. This algorithm is called *backpropagation algorithm*. See [59] for the exact functionality.

If the neural network is well trained the output is a measure for the probability that a pattern belongs to a certain class. It can be shown [60] that under certain conditions the network output corresponds to the a posteriori probability $f(C_i|x)$ that a pattern belongs to the class i for which follows with *Bayes' Rule*:

$$f(C_i|x) = \frac{f(x|C_i) \cdot f(C_i)}{f(x)}. \tag{4.2}$$

Here, $f(C_i)$ denotes the a priori probability for the class i, $f(x)$ is the class independent probability for the occurance of the pattern x and $f(x|C_i)$ the appropriate conditional probabilities for the class i. This means that the available information contained in the used

[2] e.g. target value is 0 but 1 is assigned.

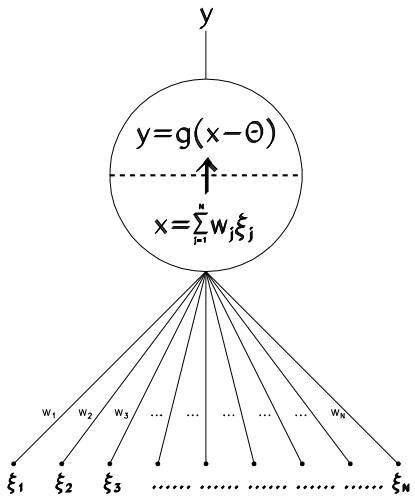

Figure 4.2: *The functionality of a node in a neural network.*

variables have been optimally utilised. Usually, the target values chosen for the output node are 0/1 or −1/1 for the class 1/2. Does one get a value near 0 (−1) or 1 then the probability is high that the pattern belongs to the adequate class.

4.1.2 Probability Density Reconstruction

Not only classification is possible by applying trained neural networks but it is also possible to reconstruct probability density distributions. Once this is done it is possible to calculate interesting quantities as mean or median value and even error estimators can be determined with this method. The general idea behind this application is to discretise the cumulated probability distribution of the whole dataset into N bins with variable width but same amount of statistics inside. For each of the bins, a separate output node is trained to the binary classification problem "the true value is above the threshold value" vs. "the true value is below the threshold value" [61], i.e. the target of the output nodes is e.g. -1 for the first and $+1$ for the latter case. The thresholds are defined by the single bins. As an example, consider the estimation of a quantity whose physical values lie in the range $[0, 1]$ and are equally distributed. Let the true value of it be 0.54 for an event and the number of bins $N = 9$. Then the target vector is: $\vec{T} = (-1, -1, -1, -1, -1, 1, 1, 1, 1)$ with the thresholds $\vec{\Theta} = (0.1, 0.2, 0.3, 0.4, 0.5, 0.6, 0.7, 0.8, 0.9)$. Of course, the number of bins (and thus nodes) should be matched to the obtainable resolution as every value in $]0.5, 0.6[$ results in the same target vector. The aim is to achieve a smooth estimate of the conditional probability density $f(t_i|\vec{x_i})$ event-by-event for a given measurement $\vec{x_i}$, t_i here denotes the true value for the event i. A similar ansatz without this aim is presented in [62].

The Procedure

The first step to this aim is a flattening of the inclusive distribution $f(t)$ by a monotonous variable transformation $F : t \to s$ such that the transformed variable s is distributed uniformly

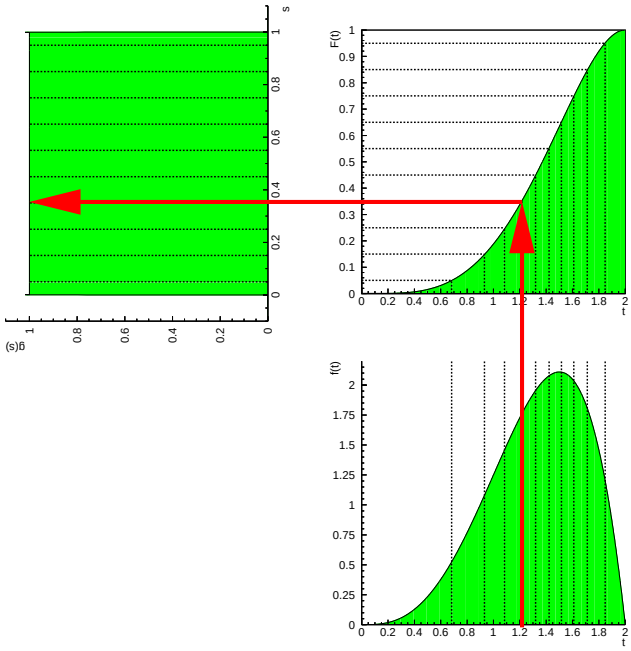

Figure 4.3: *Variable transformation $F : t \to s$ (upper right) leading to a flat output distribution $g(s)$ (upper left) when t is distributed according to $f(t)$ (lower plot).*

in the interval $[0, 1]$ with $s(t_{min}) = 0$ and $s(t_{max}) = 1$:

$$s = F(t) = \int_{t_{min}}^{t} f(t')\mathrm{d}t' \tag{4.3}$$

s measures the fraction of events that has lower values of t than the actual t. The probability density in the transformed variable $g(s)$ is simply constant 1 in the interval $[0, 1]$. s is therefore the cumulative probability density of its own distribution [61]:

$$s = G(s) = \int_{0}^{s} g(s')\mathrm{d}s' \tag{4.4}$$

This procedure is illustrated in figure 4.3 for $N = 10$.

From the Output to the Probability Density

In this framework, the neural network is trained on the variable s: Is s_{true} larger or smaller than the threshold of a certain node? Here, the thresholds are equally distributed, similar to the example mentioned above. The output of the N nodes plotted against their thresholds gives the distribution $G(s_i, \vec{x_i})$. A cubic B-spline fit [63] with variable bin size can be applied through the end points $(0, 1)$, $(1, -1)$ and the points given by the neural network. In this way one gets a closed functional form and is able to calculate, at any value of s, the value of

this distribution and its derivative and the probability density $g(s_i, \vec{x_i})$. $g(s|\vec{x})$ can then be calculated analytically from the spline parametrisation. In order to get the original variable t the backtransformation F^{-1} has to be applied. Smooth distribution functions can be achieved by a regularisation procedure which has to be applied and, additionally, some constraints must be fulfilled to be able to interprete $F(t|\vec{x})$ as cumulated probability distribution, namely monotonicity, positivity and a maximum value of 1 have to be satisfied. For these and other technical details see [61]. This procedure together with a useful pre- and postprocessing and several other features are implemented in the package NeuroBayes® [64] which has been used for some neural networks described later in this thesis.

4.2 Experiment and Detector

The DELPHI detector was located at the electron positron collider LEP which had a cirumference of 26.7 km and was situated near Geneva, Switzerland, in a tunnel 50 to 175 m below ground. Four of the eight interaction points were equipped with detectors, namely ALEPH, DELPHI, L3 and OPAL.

A complete overview of the DELPHI detector [65] and its performance [66] have been described in detail elsewhere. What follows is a short description of the elements most relevant for the analyses presented in this thesis.

Charged particle tracking was performed by the Vertex Detector (VD), the Inner Detector, the Time Projection Chamber (TPC) and the Outer Detector. A highly uniform magnetic field of 1.23 T parallel to the e^+e^- beam direction was provided by the superconducting solenoid throughout the tracking volume. The momenta of charged particles (tracks) were reconstructed with a precision of $\sigma_p/p \leq 1.5\%$ in the polar angle region $\theta > 40^\circ$ and for $p < 10$ GeV/c. The VD consisted of three layers of silicon micro-strip devices with an intrinsic resolution of about 8 μm in the $R\phi$-plane transverse to the beam line. In addition, the inner and outer-most layers were instrumented with double-sided devices providing coordinates of similar precision in the Rz-plane along the direction of the beams. For tracks with hits in all three $R\phi$ VD-layers the impact parameter resolution was $\sigma^2_{R\phi} = ([61/(p\sin^{3/2}\theta)]^2 + 20^2)\ \mu\text{m}^2$ and for tracks with hits in both Rz layers and with a polar angle of $\theta \approx 90^\circ$, it was $\sigma^2_{Rz} = ([67/(p\sin^{5/2}\theta)]^2 + 33^2)\ \mu\text{m}^2$.

Calorimeters detected photons and neutral hadrons by total absorption of their energy. The High-density Projection Chamber (HPC) provided electromagnetic calorimetry coverage in the polar angle region $46^\circ < \theta < 134^\circ$ giving a relative precision on the measured energy E of $\sigma_E/E = 0.32/\sqrt{E} \oplus 0.043$ (E in GeV). In addition, each HPC module essentially worked as a small TPC charting the spatial development of showers and so providing an angular resolution exceeding that of the detector granularity alone. For high energy photons the angular precision were ± 1.7 mrad in the azimuthal angle ϕ and ± 1.0 mrad in the polar angle θ.

The Hadron Calorimeter was installed in the return yoke of the DELPHI solenoid and provided a relative precision on the measured energy of $\sigma_E/E = 1.12/\sqrt{E} \oplus 0.21$ (E in GeV).

Powerful particle identification was made possible by the combination of dE/dx information from the TPC (and to less extent from the VD) with information from the Ring Imaging CHerenkov counters (RICH) in both the forward and barrel regions (see section 4.6). The RICH devices utilised both liquid and gas radiators in order to optimise coverage across a

wide momentum range: liquid was used for the momentum range from 0.7 GeV/c to 8 GeV/c and the gas radiator for the range 2.5 GeV/c to 25 GeV/c.

4.3 Selection of Multihadronic Events

The data was taken with the DELPHI detector at centre-of-mass energies around the Z^0-pole. Multihadronic Z^0 decays are selected by the following requirements:

- at least 5 reconstructed charged particles with a momentum greater than 0.2 GeV/c and a polar angle Θ in the range $20^\circ < \Theta < 160^\circ$ have to be in the event,
- the total energy of these particles has to be larger than 12% of the centre-of-mass energy, with at least 3% of it in each of the forward and backward hemispheres defined with respect to the beam axis.

This selection gives 1.4 million multihadronic events for 1994 data, 0.7 million for 1995 and 0.1 million for 1996-1998 data. The same selection is applied to the Monte Carlo samples used consisting of $Z \to q\bar{q}$ and $Z \to b\bar{b}$ events generated with Jetset 7.3 [19] (with tunings optimised for DELPHI data [20]). The Monte Carlo sample of 1994 could also be used for describing the b-events taken in the years 1996-1998. Multihadronic events are selected by these cuts with an efficiency of more than 95%. The remaining background is less than 1% [66].

4.4 Definition of Jets

The assignment of particles to jets is done by the LUCLUS algorithm [68]. The distance between two clusters[3] is defined as:

$$d_{ij}^2 = \frac{4 \cdot |\vec{p}_i|^2 \cdot |\vec{p}_j|^2 \cdot \sin^2(\Theta_{ij}/2)}{(|\vec{p}_i| + |\vec{p}_j|)^2} \tag{4.5}$$

Two clusters are merged for $d_{ij} < d_{join}$. d_{join} is chosen to have a value of 5 GeV at LEP energies. To define the orientation of an event the variable *thrust* is used:

$$T = \max_{|\vec{n}|=1} \frac{\sum_i |\vec{n} \cdot \vec{p}_i|}{\sum_i |\vec{p}_i|} \tag{4.6}$$

The thrust axis is given by the unity vector $\vec{n}$ for which T becomes maximal. T lies between 1/2 and 1. $T \approx 1$ means a 2-jet event and $T \approx 1/2$ means an isotropic, sphere-shaped event.

4.5 Track Parameters

A charged particle in an homogenous magnetic field parallely aligned to the z-axis moves along a helix, whose projection on the $R\Phi$-plane is a circle. Plotting the arc length versus z gives a straight line. Thus, five parameters are needed to parametrise the trajectory of a charged particle, three of which describe a circle in the $R\Phi$-plane. In DELPHI, the parameters are defined at the point lying in the $R\Phi$-plane nearest to the origin (*perigee parameters*). The parameters in $R\Phi$ are:

[3] A cluster consists of one or more particles.

- the signed impact parameter $\epsilon = -\text{sign}(Q) \cdot (|R| - M)$ where sign(Q) is the sign of the charge, R is the signed radius of curvature ($R < 0$ for positively charged particles) and M the distance from the centre of the circle to the origin,
- the azimuthal angle ϕ of the tangent to the circle at this point and
- the curvature $\kappa = 1/R$.

The parameters used in in the Rz-plane are:

- the z-impact parameter Z which is defined as the distance in z-direction between the closest point to the origin in $R\Phi$ and the origin itself and
- the polar angle Θ with $\tan\Theta = \sqrt{p_x^2 + p_y^2}/p_z$.

The helix is therefore described by $(\epsilon, \phi, \kappa, Z, \Theta)$. These parameters can be calculated for any point. This is important if one wants to know if a particle originates from a certain vertex because the measured impact parameters ϵ and Z have small values. (They are zero per definition in the ideal case of an exact reconstruction of vertex and track.)

4.6 Identification of Charged Hadrons

The identification of stable[4], charged particles (pions, kaons and protons) is done by a measurement of the specific ionisation loss in the TPC and of the averaged Cherenkov angles in both RICH detectors (liquid and gas radiators). The dependance of the specific ionisation loss $\mathrm{d}E/\mathrm{d}x$ on the momentum for different particles is shown at the top of figure 4.4. Three variables are used for particle identification: the measured value for $\mathrm{d}E/\mathrm{d}x$, its expected value and the expected error of measurement. The two last variables are evaluated for different particle hypotheses. So it is possible to assign to a track a probability for each hypothesis. See [66] for details.

Charged particles are identified in the RICH detectors by detecting the Cherenkov radiation which is emitted by the first in a dielectric medium if their velocity is larger than the speed of light in this medium. The determined variables are the averaged emission angle, the number of photons and the expected error. These can also be evaluated for different particle hypotheses. The dependance of the Cherenkov angle on the momentum for different particles is shown in figure 4.4 in the middle and at the bottom plot. Detailed descriptions of the algorithms can be found in [77]- [79].

4.6.1 Particle Identification by a Neural Network

All the information available from the different detectors and algorithms can be combined best by a neural network. Three different networks have been trained with respect to the existing information for both kaon and proton identification:

- momentum $p > 0.7$ GeV/c with full RICH information,
- $p > 0.7$ GeV/c without information from the liquid RICH and

[4] "Stable" means here that the particles live long enough to be detected.

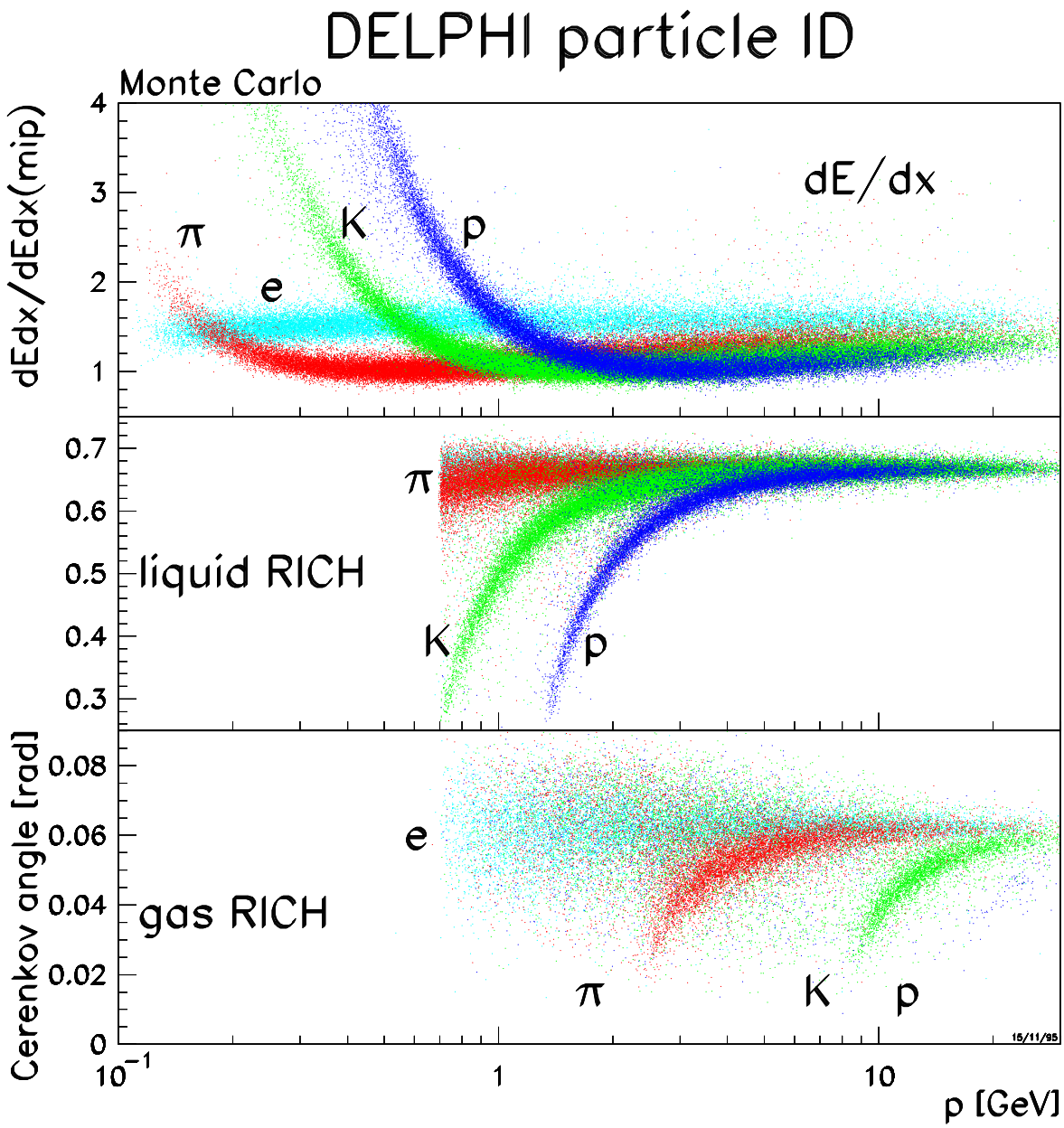

Figure 4.4: dE/dx- *and RICH information for particle identification in the simulation: the specific energy loss* dE/dx *in the TPC (top) as well as the Cherenkov angle in the liquid (middle) and gas radiator (bottom) for different particles.*

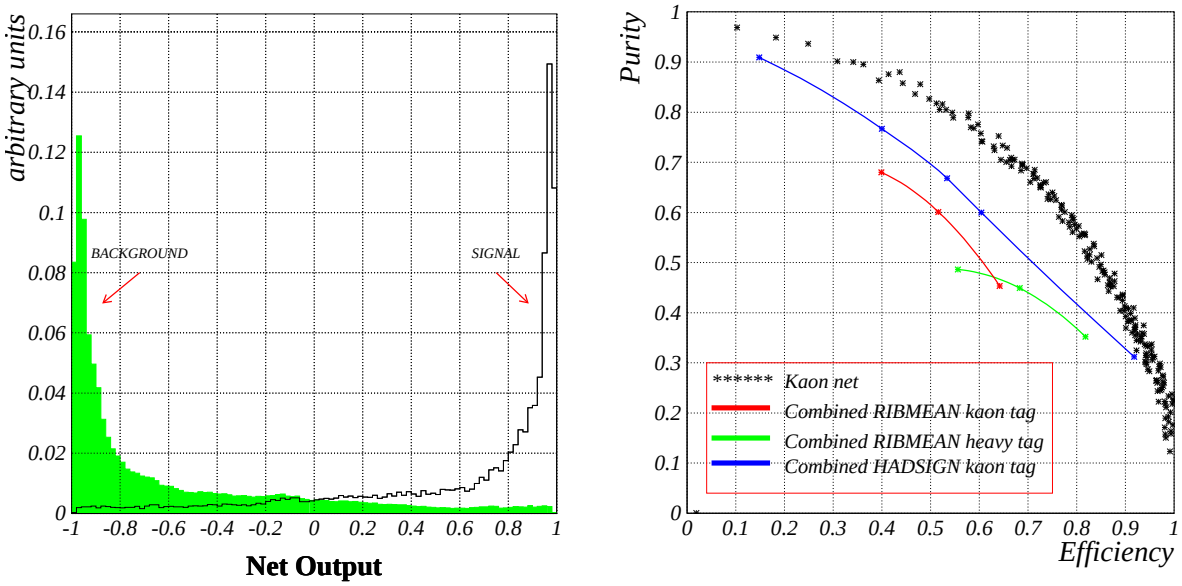

Figure 4.5: *Left: Separation of signal and background for the kaon network with full RICH information. The signal is around +1, the background around −1. Right: Purity versus efficiency averaged over all momenta for the same network compared with the combined particle information of other algorithms used in DELPHI [77, 78]. 'Heavy' tag means that kaons and protons are not separated from each other.*

- $p < 0.7$ GeV/c with combined $\mathrm{d}E/\mathrm{d}x$ measurements from the TPC and the VD respectively.

Figure 4.5 shows the performance of the kaon network with full RICH information. An accurate description of all networks, especially of their input variables, and their performance can be found in [80].

4.7 Reconstruction of Low Energetic Photons

The energy spectrum for the photons from $B^* \to B\gamma$ decays lies not in a favorable region for reconstruction in the HPC. At LEP energies, the photon spectrum goes up to about 800 MeV. The low-energy acceptance of the HPC would limit the range of accessible photon energies, and the detected photons are reconstructed with an inherent resolution that goes as $1/\sqrt{E}$. In order to overcome these difficulties, this analysis is restricted to photons converted to e^+e^- in material before the TPC. This means that the photon interacts with a nucleus and an electron-positron pair is created. Photon conversions in the outer wall of the TPC and in the RICH cannot be reconstructed because of the limited track reconstruction. In general, 40% of all photons convert into electron-positron pairs before they reach the HPC, 7% convert in front of the TPC, where they produce reconstructable $\mathrm{e^+e^-}$-pairs.

There are two types of reconstructed converted photons: double and single electron conversions [67]. In the case of double electron conversions both the electron and the positron are reconstructed in the TPC. All tracks that have a conversion radius R, i.e. the distance between the primary vertex and the conversion point[5], which is more than one standard

[5]The point, in the $R\Phi$-plane, at which a tangent to the electron track points directly back to the primary

deviation away from the primary vertex, as defined by the beam spot, are considered to be conversion candidates. This selection is necessary to keep background at a tolerable level, but it limits the efficiency at high energies. If two oppositely charged candidates are found with compatible decay point parameters, they are linked together to form a converted photon. The following selection criteria are imposed:

- the reconstructed mean conversion radius is below 34 cm,
- at least one of the tracks has no associated point in front of the reconstructed mean conversion radius,
- the Φ-difference between the two conversion points is 30 mrad at most,
- the difference between the polar angles Θ of the two conversion points is 15 mrad at most.

The energy of these reconstructed converted photons has an accuracy of $\pm 1\%$, the direction in Θ as well as in Φ has one of ± 1.5 mrad. The conversion radius can be accurately determined up to ± 5 mm. At very low energies the acceptance drops for asymmetric conversions since the TPC could only reconstruct electrons with a transverse momentum with respect to the beam above 50 MeV/c. In order to reconstruct these single electrons, tracks are only used if they have not been paired with another candidate. They are accepted as single only when the following conditions are satisfied:

- the conversion radius is between 28 and 33 cm,
- the conversion point is at least 4 standard deviations away from the beam crossing (in the $R\Phi$-plane),
- no hits are measured in front of the reconstructed conversion point,
- the z-coordinate of the conversion point and the one from the angular extrapolation from the reconstructed primary vertex towards the conversion point must coincide within 1 cm.

Finally, an energy correction is applied to account for the unseen electron. After this correction, an energy resolution of approximately 10% can be achieved. The single-electron conversion represents 25% of all converted photons in data and lowers the acceptance threshold from 250 MeV to 100 MeV. More details about the reconstruction of converted photons can be found in [67].

4.8 Tagging of $b\bar{b}$-Events

A primary $b\bar{b}$-pair is produced in approximately 22% of the multihadronic events. In order to study these events it is necessary to discriminate these decays of the Z^0-bosons from those into light quarks[6]. One possibility is the detection of a high energetic lepton from semileptonic

vertex position.

[6]For simplicity, u-, d-, s-, and c-quarks are denoted as light quarks here.

decays of a b-hadron. These leptons, relatively to the jet axis, have a high transverse momentum due to the b-hadron's large mass. This can be used to suppress background events. Unfortunately, semileptonic decays have a branching fraction of about 10% each.

Using vertex detectors with high resolution make a more efficient tagging of b$\bar{\text{b}}$-events possible. This method has been pioneered by the ALEPH collaboration [69] and adapted for DELPHI [70]. A complete overview of b-tagging in DELPHI can be found in [71].

4.8.1 The Impact Parameter Method

Because of the proper lifetime of $\langle\tau\rangle \approx 1.55$ ps and the high energies of $\langle E_B\rangle \approx 0.7 \cdot E_{beam} \approx 30$-35 GeV due to the hard fragmentation b-hadrons fly an average distance of 3 mm before they decay. A b$\bar{\text{b}}$-event in the vertex detector with good separated primary and secondary vertices is shown in figure 4.6. Together with the high mass of $m_b \approx 5$ GeV/c^2 of the b-hadrons this leads to large impact parameters of the decay products with respect to the primary vertex. This can be used for tagging b$\bar{\text{b}}$-events but for a precise measurement of the impact parameter, an accurate knowledge of the primary vertex is needed.

Primary Vertex Reconstruction

The primary vertex is reconstructed for every hadronic event using the average beam spot position of 200 consecutive events as constraint. This method is sufficient to account for a possible movement of the particle bunches and gives a good precision [72]. The position can be measured with an accuracy of about 10 μm in x and 5 μm in y. The beam spot size is about 100 μm in x-direction and < 10 μm in y-direction. The spread in y is smaller because there is no broadening caused by synchrotron radiation. The primary vertex is determined by an iterative vertex fit using only tracks with at least two hits in the vertex detector to minimise biases by decay products of long-living particles (e.g. neutral kaons and Λ^0). There had been an Rz-readout of the vertex detector since 1994, and the primary vertex could be determined in all three dimensions. Previously it was only possible in the $R\Phi$-plane. The resolution with Rz-readout is about 22 μm in light quark events and about 35 μm in b$\bar{\text{b}}$-events. The worse resolution in the latter events is due to the fact that tracks from secondary decays cannot be fully eliminated and that the multiplicity at the primary vertex is smaller.

Determination of the Impact Parameter

The impact parameter of a track is defined at the point with the shortest distance to the primary vertex in the $R\Phi$-plane (see section 4.5) as the resolution of the vertex detector is clearly better in this plane than in Rz. The $R\Phi$- and the Rz-impact parameters are equal to the distances of this point to the primary vertex in the accordant projections. The sign of the impact parameter is defined as positive if the vector from the primary vertex to the point of closest approach and the jet to which the track belongs, include an angle smaller than 90°. The decay products of long-living particles therefore have a positive impact parameter. The impact parameter of tracks originating from the primary vertex is zero by definition. Due to the limited detector resolution, these tracks have equally likely negative and positive values for the impact parameter. Another important variable is the significance of the impact parameter. It is defined as the ratio of the impact parameter to its error. Figure 4.7 shows the distribution of the significance for data and simulation as well as the contributions of the different flavours. The clearly visible excess at positive values is used for b-tagging. The

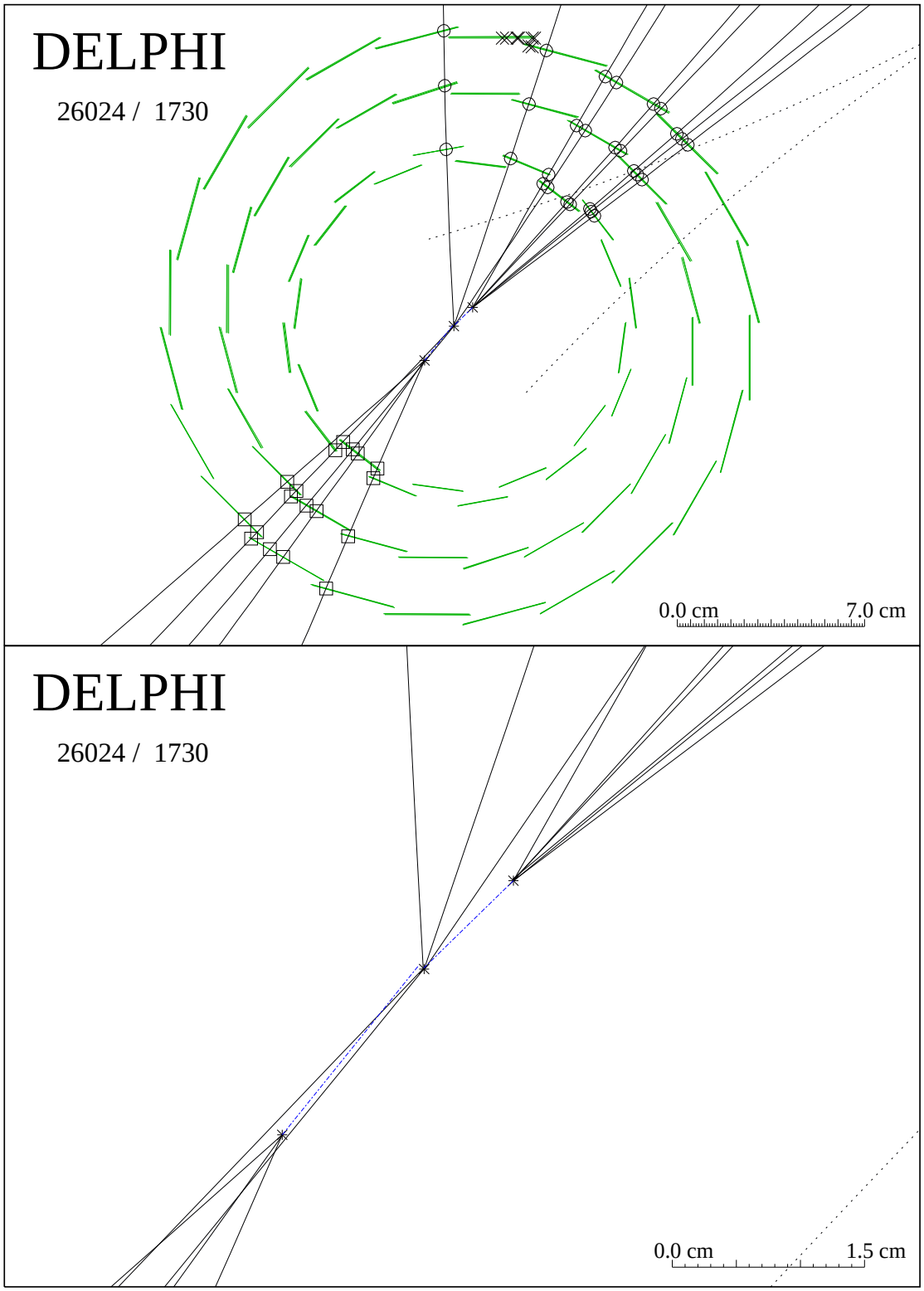

Figure 4.6: *A $b\bar{b}$-event in the vertex detector (top) and in magnification (bottom). Both decay vertices of the b-hadrons are clearly visible and are separated well from the primary vertex.*

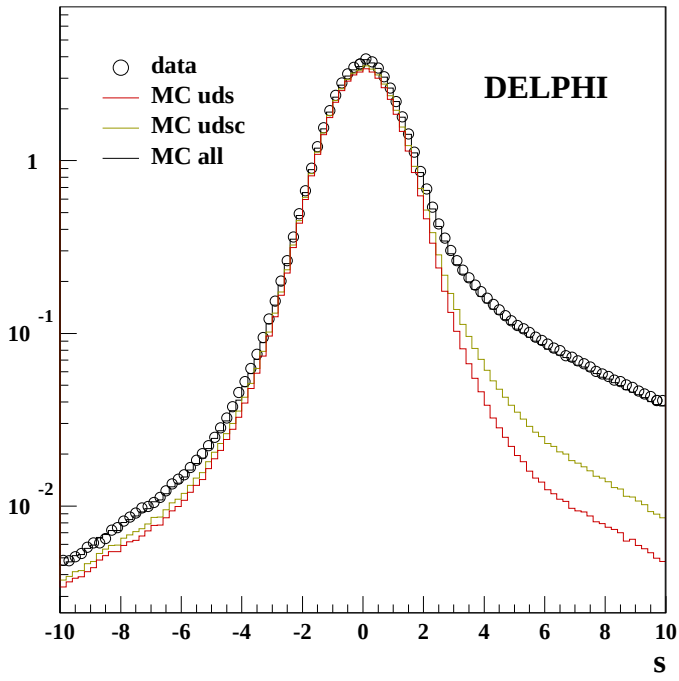

Figure 4.7: *The significance of the impact parameter. The distribution in data as well as in the simulation are shown together with the contributions of the different quark types. The surplus at positive values is used for b-tagging.*

negative side of the distribution mainly reflects the detector resolution and is used to build the track probability function $P(S_0)$:

$$P(S_0) \quad = \quad \begin{cases} \int_{S<S_0} f(S)dS, \text{ for } S_0 < 0 \\ P(-S_0), \text{ for } S_0 > 0. \end{cases} \tag{4.7}$$

which is by definition the probability for a track from the primary vertex to have a significance with absolute value S_0 or greater. $f(S)$ denotes the probability density of the significance distribution and is directly extracted from data. By using the track probability function, the probability for a group of N tracks that all N tracks originate from the primary vertex can be computed:

$$P_N = \Pi \cdot \sum_{j=0}^{N-1} (-\ln \Pi)^j / j! \quad , \text{ with } \Pi = \prod_{i=1}^{N} P(S_i), \tag{4.8}$$

where S_i denotes the measured significance of track i. This lifetime probability can be evaluated for arbitrary groups of tracks, e.g. for all tracks of an event, of a hemisphere or of a jet. By construction, its distribution is flat for a group of tracks originating from the primary vertex, provided the significance of these tracks is uncorrelated, while tracks from b-hadron decays should have a sharp peak at zero. When the z-impact parameter is measured, the probability $P_z(S_0)$ is computed in the same way as for the $R\Phi$-impact parameter. The lifetime probability is then given by a combination of both $P_{R\Phi}$- and P_z-probabilities. In order to get a good agreement between data and simulation the impact parameters and their errors are corrected in the simulation [71, 73]. With this approach, the deviation of the b-tag efficiencies between data and simulation is reduced to $\lesssim 3\%$.

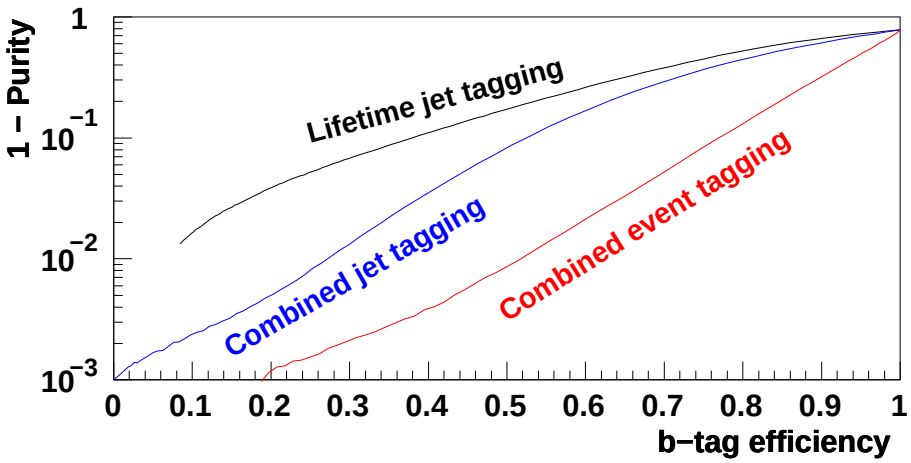

Figure 4.8: *Comparison of lifetime and combined b-tagging for multihadronic* Z^0*-events.*

4.8.2 Combined Tagging

The separation of $b\bar{b}$-events from events with light quarks or of b-jets from gluon jets provided by the impact parameter method can be improved by including other variables containing information on the presence of a b-hadron. To combine them in a single variable a likelihood ratio method is used in DELPHI [74, 75]. This is possible because the variables are almost independent. For independent variables, this approach achieves optimal tagging, i.e. the best possible background suppression for a given signal efficiency [76]. The description of the method as well as the discriminating variables used in the likelihood ratio can be found in [71].

b-hadrons are almost always produced in pairs and the presence of the second one improves the event b-tagging significantly. The information about the presence of two b-hadrons can be well combined within the likelihood ratio method as each flavour is produced independently of all other flavours. Figure 4.8 compares the performance of event tagging and of jet tagging for Z^0-events. It can be seen that a strong suppression of background can be achieved, depending on the desired efficiency.

4.9 Standard Particle Selection

Charged particles used in the algorithms and analyses presented in the following chapters must have passed the following track selection criteria:

- impact parameter, with respect to the origin, in the $R\Phi$-plane $|\delta_{R\Phi}| < 4.0$ cm,
- impact parameter, with respect to the origin, in the Rz-plane $|\delta_z| < 6.0$ cm,
- cosine of the track's polar angle $|\cos\Theta| < 0.94$,
- significance of the track's energy $\frac{\Delta E}{E} < 1.0$,
- at least one track hit in $R\Phi$ in the vertex detector and

- tracks must not have been flagged as originating from material interactions [81].

Neutral particles are only used if they have been identified as a photon, π^0, K_s^0, a Λ^0 or a neutron.

Chapter 5

Inclusive Reconstruction and Identification of b-Hadrons

The algorithm used for the inclusive reconstruction of b-hadrons is described in this chapter. These tools are all implemented in the BSAURUS package [82]. Moreover, the routines for identifying the weakly decaying and the excited b-hadron respectively are described. These routines are mainly based on newly developed and optimised neural network techniques (see section 4.1.2).

5.1 Inclusive Reconstruction of b-Hadrons

In analyses using exclusive reconstruction all particles originating from a decay of a hadron (*daughter particles*) are reconstructed and thus the hadron itself. Inclusive reconstruction means that one uses a certain criterion which should only be fulfilled for daughter particles of the considered hadron. This method is used for the reconstruction of b-hadrons in the analyses presented in this thesis as these hadrons have a lot of different decay modes with small branching fractions. This would complicate an exclusive reconstruction, especially due to the high combinatorial background.

5.1.1 The Rapidity Algorithm

The variable used as criterion to identify the daughter particles of a b-hadron is the rapidity y, which is defined as:

$$y = \frac{1}{2}\log\left(\frac{E + p_{long}}{E - p_{long}}\right), \tag{5.1}$$

where E denotes the energy of the particle and p_{long} its longitudinal momentum with respect to the jet axis. This axis is defined via the routine LUCLUS [68] with the transverse momentum as a distance measure and the cut-off parameter $d_{join} = 5.0$ GeV/c, which gives the best reconstruction of the initial b-hadron direction according to simulation studies. Particles originating from a b-hadron have a higher rapidity than particles from fragmentation. Monte Carlo studies showed, that the distribution for B-decay products are peaked at $y = \pm 2.4$ with a tail to smaller (in terms of absolute value) rapidities because of hard gluon radiation (see figure 5.1).

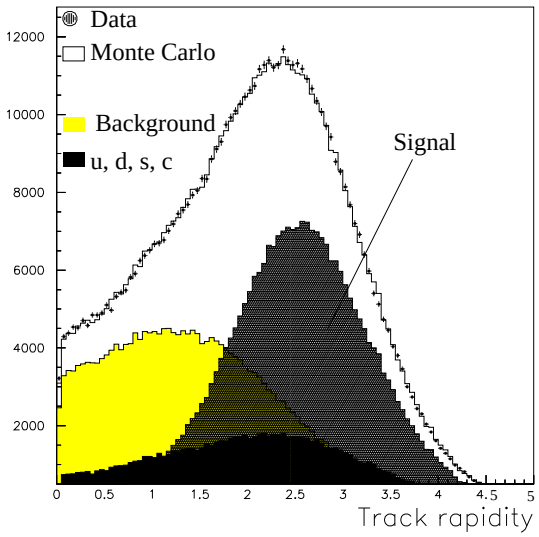

Figure 5.1: *Rapidity distributions from 1994 data and simulation normalised to the number of entries. Using simulated events, tracks originating from the primary vertex and tracks from the b-hadron decay chain are also plotted.*

Each event is divided into two hemispheres, which are defined by the plane perpendicular to the thrust axis that contains the primary vertex. The rapidity of each reconstructed particle is calculated with respect to a reference axis, where pion mass is assumed for the charged and photon mass for the neutral ones. The reference axis is a jet axis selected in the following way:

- when the event is a two jet event, the reference axis for the hemisphere is the jet axis of that hemisphere.
- When a hemisphere contains two or more jets:
  - when one of the jets is the one with the highest energy in the event, that jet axis forms the reference axis.
  - When the highest energy jet is in the opposite hemisphere, the combined probability for the tracks in a jet to have originated from the event primary vertex (P_{jet}) is formed (via the AABTAG package algorithms [70, 71, 73]). The jet with the smallest probability, i.e. the one which is most 'B-like', is then selected as reference axis if $P_{jet} < 0.05$.
  - When no jet in the hemisphere satisfies the above criteria, the jet with the highest energy is selected to form the reference axis.

With this scheme the probability to correctly select the two b-jets in a three-jet event was about 70%. In addition, internally in the algorithm, the hemispheres are numbered as 1 or 2 with the convention that the jet forming the reference axis for hemisphere 1 is of higher energy than that for hemisphere 2.

Additionally to the standard particle selection explained in section 4.9 particles have to pass a cut on the rapidity: Those with a rapidity greater than 1.6 are assumed to come from the decay of a b-hadron.

The four-momenta of the particles selected this way are added together to obtain a first estimate of the energy E_{raw} and the momentum components p^i_{raw} of the b-hadron. This method is called *rapidity algorithm* and serves as a first step for the reconstruction of the secondary vertex.

5.1.2 Reconstruction of Secondary Vertices

One attempt to fit a secondary vertex per hemisphere is made. A first estimate of the flight direction of the weakly decaying b-hadron is obtained by the direction of the particle's momentum. As it is important for fitting a secondary vertex to reject as many particles originating from the primary vertex as possible additional criteria are applied to those tracks. There must be a minimum of two tracks for the vertex fit to be attempted and the selection criteria are as follows:

- the highest energetic muon or electron candidate if its energy is greater than 3 GeV,
- tracks with $\frac{L}{\sigma_L} > 2$ or
- tracks with $\frac{L}{\sigma_L} < 2$ but $|y| > 2.5$ and $L > 0.1$ cm.

L is determined in the following way: The crossing point of each track with the estimated B-candidate's direction vector is found and then L is the distance between the primary vertex and this crossing point; σ_L denotes the error in L. If less than two particles remain after this selection further attempts are made to add tracks to the fitting procedure, depending on the number of surviving tracks. If one track is left after these cuts, tracks with $y > 3$ are added to the particle list. If still only one track is selected, the track with highest rapidity from the remaining track list in the hemisphere is added. If there is no track left, a search is made for the best kaon candidate in the hemisphere based on the kaon probability defined in section 4.6.1. If this kaon candidate has $y > 2$ it is added to the track in the remaining track list of the hemisphere with the highest rapidity. This pair alone will then form the starting track list for the vertexing procedure. Finally, if no kaon candidate exists in the hemisphere the two tracks of highest rapidity are selected. Using the tracks picked out by this selection, a secondary vertex fit is performed in three dimensions constrained to the direction of the B-candidate momentum vector. The event primary vertex is used as a starting point and if the fit does not converge[1], the track making the largest χ^2-distribution is stripped away in an iterative procedure and the fit is repeated. In this procedure the primary vertex position is also fitted and the B-candidate direction is updated according to the vector joining the primary and secondary vertex points.

Once a convergent fit has been attained, the final stage of the secondary vertex fitting involves an attempt to add tracks into the fit that failed the initial track selection criteria but nevertheless are consistent with originating from that vertex. These tracks are identified on

[1]Here, non-convergence means the fit took more than 20 iterations. A further iteration is deemed necessary if the χ^2 is above 4 standard deviations during the first 10 iterations or above 3 standard deviations during the next 10 iterations

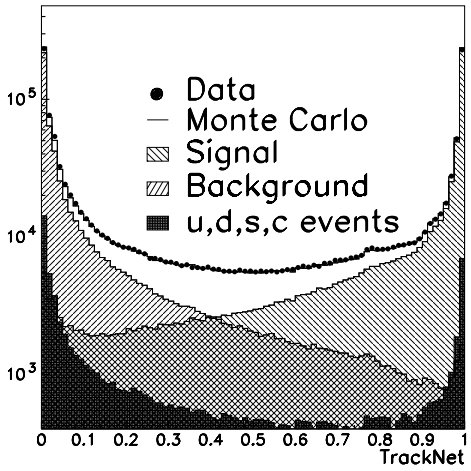

Figure 5.2: *Distributions of the Track Net output from 1994 data and simulation normalised to the number of entries.*

the basis of an intermediate version of the Track Net. This is a neural network dedicated for discriminating between tracks originating from the primary vertex and those likely to have come from a secondary vertex. It is described in section 5.1.3. A preliminary version of the Track Net is constructed, specifically for the purpose of use in this final stage of fitting. It is based on secondary vertexing information available before this final stage has run. In general, secondary vertex tracks have a Track Net output of ≈ 1. Tracks from the primary vertex have values close to zero. The track with the largest Track Net output in the hemisphere is added to the existing track list and retained if the resulting fit converges. This process continues iteratively for all tracks with a Track Net output > 0.5.

5.1.3 The Track Net

The aim of the Track Net is to discriminate between the class of tracks originating from the weak decay of a b-hadron and all other tracks in a hemisphere of a $b\bar{b}$-event. The network relies on the presence of a reconstructed secondary vertex providing an estimate of the b-hadron decay position in the event hemisphere. The b-hadron four-vector is reconstructed by the rapidity algorithm described above. The most important inputs to the neural network were:

- the magnitude of the particle momentum in the laboratory frame,
- the magnitude of the particle momentum in the B-candidate rest frame,
- the track helicity angle, defined as the angle between the track vector in the B-candidate rest frame and the B-candidate momentum vector in the lab frame,
- a flag to identify whether the track is in the secondary vertex fit or not,
- the primary vertex track probability from AABTAG and BSAURUS respectively,

- the secondary vertex track probability from AABTAG and BSAURUS respectively and
- the particle rapidity.

Figure 5.2 shows the distribution of the Track Net output for real and simulated data after the event selection cuts have been applied. The simulation distribution is divided into background originating from (u, d, s, c)-events, 'background' and 'signal' from b-events. The signal consists of tracks stemming from the b-hadron's weak decay chain. This class formed the target of the network training. The background compounds of everything else in b-events such as fragmentation tracks and decay products of excited b-hadrons. The figure illustrates the possible separation of these tracks from the b-hadron decay products and shows a good overall agreement in shape between data and simulation.

5.1.4 Separation of Secondary and Tertiary Vertices

In selection tracks for inclusion in the secondary vertex fit, there inevitably is some background from tracks that do not originate from the B-decay vertex directly but from the subsequent cascade D-decay. When such tracks are present the vertex is in general reconstructed somewhere in the region between both decay points. Thus, the reconstructed decay length will be biased to larger values and also the flight direction of the B-meson is biased towards the D-decay vertex. The resolution is therefore improved if these tracks can be identified and removed from the secondary vertex. In order to identify these tracks a neural network (BD-Net) has been developed. The network has been trained to recognise tracks originating from the decay chain $B \to D \to X$ (signal) compared to all other tracks in b-events with Track Net output larger than 0.5. The list of input variables, the discrimination power of the net and its performance can be found in [82]. Its output lies in the interval $[-1, 1]$.

The result of the BD-Net is used in four algorithms [85] in order to minimise any bias described above, starting from the standard secondary vertex introduced in section 5.1.2. In the following, only tracks with Track Net output larger than 0.5 are considered.

1) In the *Strip-down* method candidate tracks are selected if a BD-Net value lower than 0.0 is assigned to them. A secondary vertex fit is made if there are two or more tracks selected. If the fit fails to converge[2] and more than two tracks have been originally selected, the track with the highest χ^2-contribution is removed and the fit is repeated. This procedure continues iteratively until convergence is reached or less then two tracks are left.

2) In the *D-rejection* method a cascade D-candidate vertex is built first by fitting a common vertex for the two tracks with the largest BD-Net values in the hemisphere. If the invariant mass of the combination is below the D-meson mass, an attempt is made to also include the track with the next largest BD-Net value into the fit. This process continues iteratively until either the mass exceeds the D-mass or there is no track left or the fit fails to converge. The secondary vertex is then fitted using the Strip-down method without using those tracks already selected for the tertiary vertex.

[2] as defined in section 5.1.2

3) In the *Build-up* method the two tracks with the smallest BD-Net values are chosen to form a seed vertex. If the invariant mass of the remaining tracks exceeds the D-mass the track with the next lowest BD-Net output is fitted to a common vertex together with the two seed tracks. This process continues iteratively until either the fit fails to converge or the invariant mass of the remaining tracks drops below the D-meson mass.

4) The last method has been designed to improve the vertex resolution for semileptonic b-hadron decays where energy has been carried away by the associated neutrino. It is only mentioned for completeness but it is not used in the analyses presented in this thesis. When there is a clear lepton candidate (i.e. electron or muon) in the hemisphere, a cascade D-candidate vertex is reconstructed using the D-rejection method but without including the lepton. The tracks assigned to the D-decay vertex are combined to reconstruct the flight direction of the D-candidate. This 'particle' together with the lepton is used to fit the secondary vertex if the opening angle between them satisfies $|\cos\Theta_{Dl}| < 0.99$.

The choice which method to use to calculate the secondary vertex and hence to reconstruct the flight direction of the b-hadron is made by optimising the error on the direction. First the Strip-down method is used if it is successful. Then the D-rejection method is applied to get the secondary vertex. If this method also fails the B-decay vertex from the Build-up algorithm is used. If this one is not succesful either the standard secondary vertex is used for estimating the B-direction.

5.1.5 DETERMINATION OF THE B-ENERGY

Simulation studies show a strong correlation between the generated energy of a b-hadron, $E_{\mathrm{B}_{true}}$, and the initial estimated energy E_{raw}. Further correlations exist between the energy resolution $\Delta E = E_{raw} - E_{\mathrm{B}_{true}}$ and both the reconstructed mass m_{raw} of the b-hadron and the hemisphere energy scaled with the beam energy, $x_h = E_{hem}/E_{beam}$, which reflects inefficiencies and neutral energy losses. To improve the energy resolution the reconstructed energy is corrected in such a way that the existing correlations are taken into account. In doing so, one has to pay attention to the fact that m_{raw} and x_h are not independent of each other.

Separate correction functions are derived for 2-jet and >2-jet events using simulated events. Within these two classes, the hemispheres 1 and 2 are treated seperately due to the explicit energy ordering of the hemispheres. To be used in the correction procedure, hemispheres must pass the following cuts:

- E_{raw} is at least 20 GeV,
- m_{raw} lies within two standard deviations of the total data sample median value $\overline{m}_{raw}$ (i.e. ± 2.4 GeV/c^2),
- $0.6 < x_h < 1.1$.

According to studies, the starting points E_{raw} and m_{raw} are chosen in the following way: For events with > 2-jets these variables are taken from the result of the rapidity algorithm, for 2-jet events they are derived from a weighted sum of the track four-vectors. This involves weighting (via a sigmoid threshold function) of the energy and the momentum components

of charged tracks by the Track Net output (see section 5.1.3) and those of the neutral ones by their rapidity. In this way, the effects of tracks from the B-decay are enhanced and those of tracks from the primary vertex are suppressed. The latter procedure is also performed for hemispheres failing the cut on x_h to regain those B-decays.
The correction proceeds in the following way: the data are divided into several samples according to the measured ratio x_h and for each of these classes the B-energy residual ΔE is plotted as a function of m_{raw}. The median value of ΔE in each bin of m_{raw} is calculated and their m_{raw}-dependence is fitted by a third order polynomial

$$\Delta E(m_{raw}; x_h) \quad = \quad a + b(m_{raw} - \overline{m}_{raw}) + c(m_{raw} - \overline{m}_{raw})^2 + d(m_{raw} - \overline{m}_{raw})^3 \quad (5.2)$$

The four parameters a, b, c and d in each x_h-class are then plotted as a function of x_h and their dependence is fitted with third and second order polynomials respectively. Thus one obtains a smooth correction function describing the mean dependence on m_{raw} and on x_h as determined from Monte Carlo simulations. Finally, a small bias correction is applied for the remaining mean energy residual as a function of the corrected energy.

To improve this estimate of the B-energy two neural networks have been built, separately for 2-jet and $>$ 2-jet events, using similar input variables. The NeuroBayes® package [64] has been used for these networks. The following 19 input variables are used:

- the corrected energy described above,
- E_{raw},
- m_{raw},
- x_h,
- the total hemisphere energy normalised by an estimate of the centre-of-mass energy E_{cm}, obtained by considering the Z^0 to decay into the two-body final state of a b-hadron jet with mass $M_{\text{B-}jet}$ recoiling against all other particles in the event with mass M_{recoil}, i.e. in the rest frame of the Z^0,

$$E_{cm} \quad = \quad \frac{M^2_{Z^0} - M^2_{recoil} + M^2_{\text{B-}jet}}{2M_{Z^0}}\,, \quad (5.3)$$

- an estimate of E_{cm} as given by equation 5.3 where M_{recoil} is based on charged tracks only; in the hemisphere containing the B-candidate, only tracks likely to have originated from the fragmentation process are selected (by use of the Track Net (see section 5.1.3)) but all tracks are used in the opposite hemisphere,
- a further estimate of E_{cm} as given by equation 5.3 where neutrals from the opposite hemisphere are also included in the formulation of M_{recoil},
- an estimate of the missing p_T between the B-candidate direction and the thrust axis calculated using only fragmentation tracks in the same hemisphere as the B-candidate (via use of the Track Net) and all tracks in the opposite hemisphere; the calculation is repeated for two different definitions of the b-hadron's direction: one being the vector pointing from the reconstructed primary vertex to the reconstructed secondary vertex and the other given by the vector $\vec{p}_{raw}$,

- the mass of the reconstructed secondary vertex,
- the polar angle of the B-candidate momentum vector,
- the difference between the number of tracks in the hemisphere passing the selection cuts and the number of such tracks that, in addition, pass a Track Net cut of 0.5,
- the total number of all charged and neutral particles,
- the number of particles passing a Track Net cut of 0.5,
- the probability that the best electron or muon candidate in the hemisphere, with the correct charge correlation, originates from the B-candidate,
- the gap in rapidity between the track of highest rapidity with a Track Net value less than 0.5 and the track of lowest rapidity and Track Net value greater than 0.5,
- the (binomial) error of the vertex charge measurement Q_v, defined as

$$\sigma_{Q_v} = \sum_{i}^{tracks} \sqrt{P_{\mathrm{B}}(i)(1 - P_{\mathrm{B}}(i))} \tag{5.4}$$

  where $P_{\mathrm{B}}(i)$ is the Track Net value for track i,

- a hemisphere 'quality flag' constructed by counting the number of tracks in the hemisphere likely to be badly reconstructed, i.e. the number of tracks failing the standard selection cuts.

5.2 IDENTIFICATION OF b-HADRONS

Important tools for the identification of b-hadrons are neural networks. For the networks described next, the JETNET neural network package [84] is used inside BSAURUS. It is almost always run in a feed-forward mode with three layers and a sigmoid function as the transfer function. The hidden layer typically contains one more node than the input layer. The subsequent description follows the one in [82] where more details, e.g. the distribution of input variables and information about the performance, can be found.

5.2.1 THE FLAVOUR NET

In an attempt to optimally use the information available, the BSAURUS approach for tagging the flavour, i.e. b- or $\bar{\mathrm{b}}$-quark, works by first constructing a probability per track and then combining these to give a probability at hemisphere level. Separate neural networks are trained to tag the underlying quark charge for the cases when there was a B^+, B^0, B_s or b-baryon[3] produced in the hemisphere. In addition, two sets of such networks are built, one trained only on tracks originating from the fragmentation process and the other one trained only on tracks from the weak b-hadron decay.

[3]The charge conjugate states are always implied.

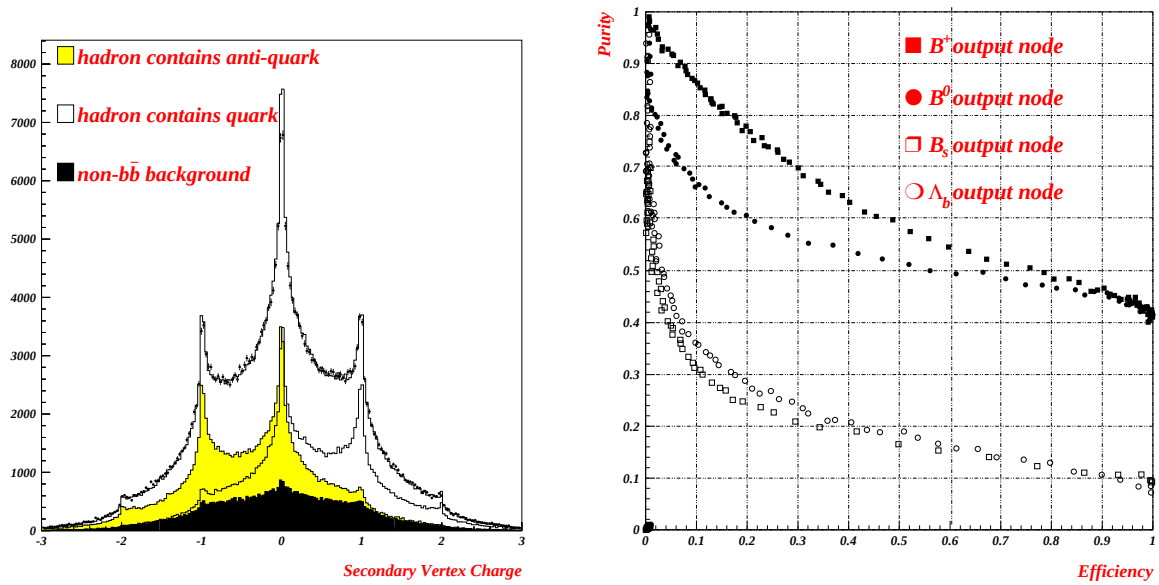

Figure 5.3: *The vertex charge comparing data (points) to simulation (histogram) and showing the single contributions (left). The performance of the BHBN neural network for enriching the various b-species (right).*

The basis of the Flavour Net is to construct the conditional probability for each track to have the same charge as the b-quark in the b-hadron both at the moment of production and of decay. These probabilities are separately constructed for each of the b-hadron types. A neural network is used with a target output of value -1 (+1) if the track charge is correlated (anticorrelated) with the b-quark charge. See [82] for the list of input variables and the conditional probability distributions obtained. Finally, these probabilities are combined to a likelihood ratio in order to attain a flavour tag at hemisphere level. Two further networks are built to combine these probabilities and likelihood ratios together with other estimators[4] for the quark flavour for an optimal tagging of the production and decay flavour. For details, see [82].

5.2.2 The b-Species Net

A neural network has been trained for identifying the different types of weakly decaying b-hadrons, B^+, B^0, B_s and b-baryon per hemisphere. An important input variable is a vertex charge formed by weighting the charge Q of each particle with its probability P_B to originate from the b-hadron decay vertex which is delivered by the Track Net,

$$Q_V = \sum_i^{tracks} P_B(i) \cdot Q(i)\,. \tag{5.5}$$

Its distribution is illustrated in figure 5.3 on the left side. Further important input variables are the number of charged pions, variables indicating a charged kaon next to the b-hadron in the fragmentation chain and the total energy deposited in the hemisphere by charged

[4] jet charge and vertex charge

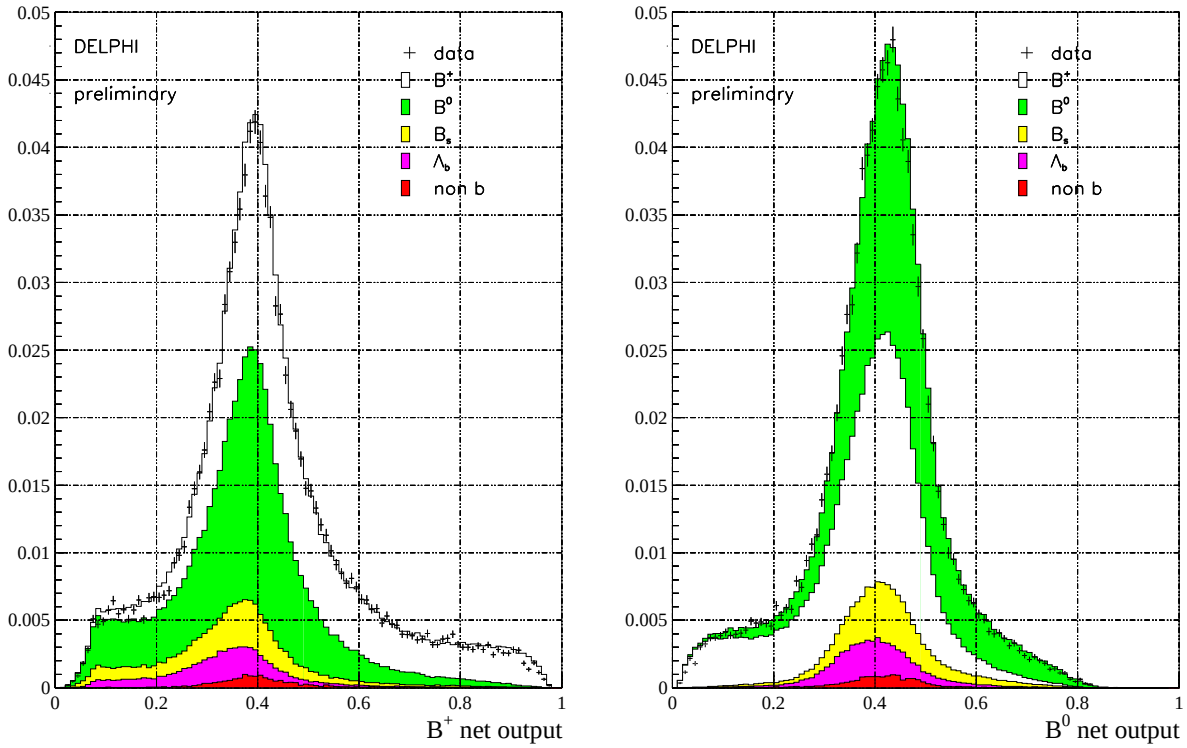

Figure 5.4: *A comparison between data and Monte Carlo for the BHBN B^+- and B^0- net outputs for B^+ (left) and B^0 (right) after applying some selection cuts. The areas of the data and the Monte Carlo histogram are normalised to one.*

and neutral particles respectively, scaled by the LEP beam energy. A complete list of the input variables and the performance of the network can be found in [82]. The performance of the network is improved by including charge correlation information from the opposite hemisphere to form a separate neural network (*BHBN*) by using the output of the same-hemisphere information network. Again, see [82] for a complete list of the input variables. The performance of the BHBN is illustrated in figure 5.3 on the right side. The network outputs of the B^+- and B^0-nodes are shown in figure 5.4. The comparison with Monte Carlo and the single contributions of the different b-species to the distributions are illustrated as well. These methods were successfully applied in a precise measurement of the B^+-, B^0- and mean b-hadron lifetime [85]. The distribution of the B_s- and b-baryon node can be found in [82].

5.2.3 IDENTIFYING EXCITED b-HADRON STATES

Two different neural networks have been trained for $B^{**}_{u,d}$- and B^{**}_s-enrichment. Special sets of Monte Carlo simulations have been produced with a flat distribution in the Q-value of the narrow $B^{**}_{u,d,s}$-mesons to keep the network from learning the generated Q-value. They have been generated by using JETSET 7.3 [19]. The background used in the training has been taken from the standard DELPHI $b\bar{b}$-Monte Carlo which has been generated with the same generator. NeuroBayes® has been used to train these networks.

$B^{**}_{u,d}$-Enrichment

B^{**+}_{u}- and B^{**0}_{d}-mesons are treated in the same way as both are supposed to have the same properties and decay into a $B^{+0}_{u,d}$-meson and a pion. A network with one output node and 20 hidden nodes has been trained with 25 input variables altogether to identify pions originating from a $B^{**}_{u,d}$-decay. Its output is in the interval $[-1, 1]$. The input variables are:

- the norm of the momentum of the B^{**}-decay pion candidate,
- its rapidity as defined in section 5.1.1,
- its rank in a track list sorted by the momentum,
- its rank in a track list sorted by the rapidity,
- the probability of the track to be a kaon,
- a proton and
- an electron,
- the number of fragmentation particles,
- the opening angle between the direction of the B-momentum and the decay pion candidate in the lab frame (the connection between the primary and the best available reconstructed secondary vertex have been used as an estimate of the flight direction),
- the cosine of the angle between the momentum of the track in the rest frame of the B^{**}-candidate and the momentum of this candidate in the lab frame (the *helicity angle*),
- the output of the Track Net,
- the probabilities from the BHBN to have a B^+ or a B^0 in the hemisphere and
- the ones to have a B_s or a b-baryon in the hemisphere

for discriminating $B^{**}_{u,d}$-mesons, and some quality variables to tell the network how good and reliable the input variables are:

- the distance between the primary and the secondary vertex,
- the error on this distance,
- the difference of the Track Net output between the track with the lowest output above 0.5 and the one with the highest output below 0.5,
- the hemisphere and event b-tags (see section 4.8),
- the value of the energy weighted rapidity distributions for the B-decay product, fragmentation and leading fragmentation hypothesis, which have been assigned to the track,
- the quality variable on hemisphere and
- track level provided by BSAURUS [82].

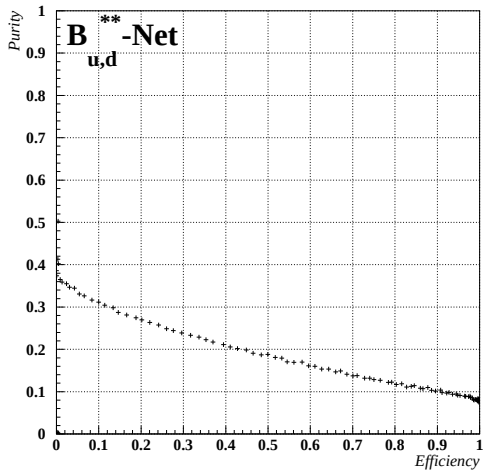

Figure 5.5: *The performance of the $B^{**}_{u,d}$-network evaluated on a $q\bar{q}$-Monte Carlo sample.*

Some precuts have been applied before the training improving the performance of the network:

- the Q-value should be lower than 1 GeV/c^2,
- the momentum of the B**-decay pion candidate should lie between 1 and 14 GeV/c,
- the rapidity of the track should be greater than 1.6,
- the Track Net output should be lower than 0.5,
- the cosine of the helicity angle should be greater than -0.75 and
- the opening angle should be lower than 0.6 rad.

The performance of this network is shown in figure 5.5. It was evaluated on an independent q$\bar{\text{q}}$-Monte Carlo sample with natural track and event composition after applying the precuts by successively cutting on the net output [90].

B^{**}_s-ENRICHMENT

The B^{**}_s-network has been trained to classify kaons originating from a B^{**}_s-decay. It consists of 40 input nodes (including the bias node), 13 nodes in the hidden layer and one output node. Some precuts have been applied before the training:

- the reconstructed Q-value should be lower than 0.5 GeV/c^2,
- the rapidity of the B^{**}_s-decay kaon candidate should be greater than 1.6,
- the momentum of the track should lie between 1 and 10 GeV/c,

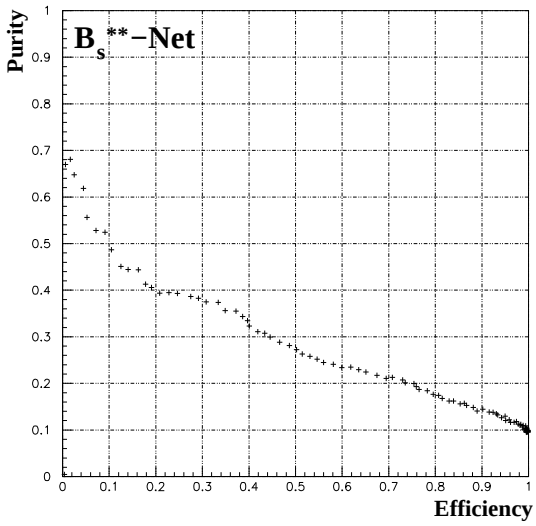

Figure 5.6: *The performance of the B_s^{**}-network evaluated on a $q\bar{q}$-Monte Carlo sample.*

- the Track Net output should be lower than 0.5,
- the cosine of the helicity angle should be greater than -0.75,
- the opening angle between the weakly decaying B-candidate and the track should be lower than 0.6 rad and
- the probability of the track to be a kaon delivered by the kaon net (see section 4.6.1) should be higher than a value corresponding to a kaon purity of approximately 42%.

In contrast to the $B_{u,d}^{**}$-net, charge correlation information between the flavour of the weakly decaying B-candidate and the kaon candidate is also given to the network. The input variables are the same ones given to the $B_{u,d}^{**}$-net replacing the pion by the kaon candidate, and additionally:

- the information which vertex algorithm is used for the secondary vertex, coded by an integer variable,
- the kaon net output for the three fragmentation particles (i.e. with Track Net output lower than 0.5) with the highest rank in the rapidity list (rank one means highest rapidity),
- the total number of tracks from the B-decay,
- the sum of the kaon net output transformed from the interval $[-1, 1]$ to $[0, 1]$ for all fragmentation tracks and
- all B-decay particles, determined by the Track Net output,
- for K_s-mesons, the sum of the rapidity distribution function parametrised for neutral leading fragmentation particles,

- the difference of this hemisphere's jet charge with the one of the opposite hemisphere, multiplied by the charge of the kaon candidate, which is also the case for all the following variables,
- the decay flavour net combining the information of both hemispheres,
- the sum of pion (i.e. excluding the kaon candidate) charges weighted by the track's probability to originate from 'beyond' or from 'this side' of the secondary vertex w.r.t. the B-candidate's flight direction,
- the likelihood-ratio based production flavour tag for B^0 and
- B_s (see section 5.2.1) and
- the same-hemisphere B^+-decay flavour net output combined with the same-hemisphere production flavour net of the opposite hemisphere.

The last item has the advantage of excluding the B_s^{**}-decay kaon candidate from the determination of the B^+-decay flavour since it excludes fragmentation tracks [90]. The performance of the B_s^{**}-net, evaluated on a $q\bar{q}$-Monte Carlo sample after applying the precuts, is illustrated in figure 5.6. The better performance compared to the one of the $B_{u,d}^{**}$-enrichment network is explained by the inclusion of the charge correlation information in the first network.

$\Sigma_b^{(*)}$-BARYON IDENTIFICATION

Another neural network has been trained for $\Sigma_b^{\pm(*)}$-baryons ientification. Special sets of Monte Carlo simulations have been produced as well for this task analogous to the ones generated for $B_{u,d,s}^{**}$-enrichment (see section 5.2.3). NeuroBayes® was used for its training, too. The precuts applied before the training were:

- the reconstructed Q-value should be lower than 0.3 GeV/c^2,
- the Track Net output of the decay pion candidate should be lower than 0.5,
- the cosine of the helicity angle should be greater than -0.9 and
- the track should have most likely been originated from the primary vertex (using the probabilities calculated by the AABTAG package algorithms [70, 71, 73]).

The network consists of 30 input nodes, 20 nodes in the hidden layer and one output node. The output is in the interval $[-1, 1]$. The input variables are:

- the probabilities of the BHBN to have a B^+, a B^0 or a B_s in the hemisphere and
- the one to have a b-baryon in the hemisphere,
- the energy of the $\Sigma_b^{(*)}$-candidate scaled by the beam energy,
- the momentum of the Λ_b-candidate scaled by the momentum of the $\Sigma_b^{(*)}$-candidate,
- the momentum of the decay pion candidate scaled by the momentum of the $\Sigma_b^{(*)}$-candidate,

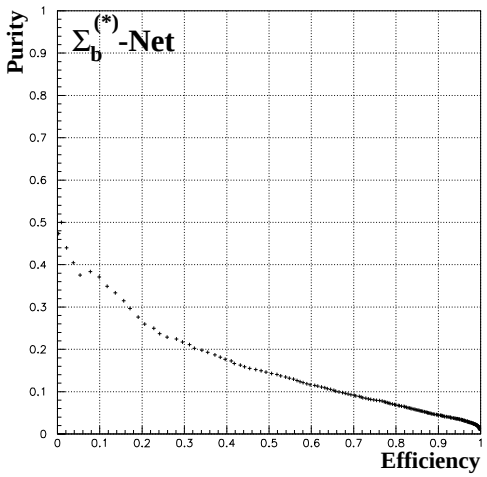

Figure 5.7: *The performance of the $\Sigma_b^{(*)}$-network evaluated on a $q\bar{q}$-Monte Carlo sample.*

- the rapidity of the pion candidate
- its rank in a track list sorted by the momentum and
- its rank sorted by the rapidity,
- the cosine of the helicity angle,
- the cosine of the opening angle between flight directions of the Λ_b-baryon and the pion,
- the probabilities from the DELPHI b-tagging package that the pion comes from the primary or secondary vertex and
- the ones from BSAURUS respectively,
- the Track Net output for the pion track
- the value of the energy weighted rapidity distributions for the B-decay product, fragmentation and leading fragmentation hypothesis, which have been assigned to the pion,
- a variable telling which secondary vertex algorithm has been used,
- the difference of the Track Net output between the track with the lowest output above 0.5 and the one with the highest output below 0.5,
- the event b-tag,
- the quality variable on hemisphere and
- track level provided by BSAURUS.

The performance of the network is shown in figure 5.7. It was evaluated on an independent $q\bar{q}$-Monte Carlo sample with natural track and event composition after applying the precuts.

Chapter 6

Measurement of Mass Splittings in the $(B^*\text{-}B)_{u,d}$-System

6.1 Analysis Procedure

The mass difference between the B^* and the B is reconstructed by combining the weakly decaying B-candidate, described in section 5.1, with the converted photon, described in section 4.7, and calculating the invariant mass of the combination minus an assumed B-mass value of 5.279 GeV/c^2. The resulting mass difference distribution for all selected B^*-meson candidates is shown in figure 6.1.

6.1.1 Event Selection

Multihadronic events are selected by applying the cuts listed in section 4.3. Hemispheres are then accepted if the following criteria are satisfied:

- $|\cos\Theta_{thrust}| < 0.7$ (Θ_{thrust} is the the angle between the thrust axis and the beam direction),
- there are only 2 jets in the event, clustered with LUCLUS and $d_{join} = 5$ GeV/c (see section 4.4),
- the RICH detectors and the vertex detector worked efficiently,
- the event is tagged as a $Z \to b\bar{b}$ event by the standard DELPHI b-tagging package 4.8.2 with a selection of >1.0 in this quantity,
- the secondary vertex fit from the BSAURUS package fulfills the internal conditions for convergence (see section 5.1.2),

These cuts select $b\bar{b}$ events with a purity of 98% and an efficiency of 35% as estimated from the simulation.

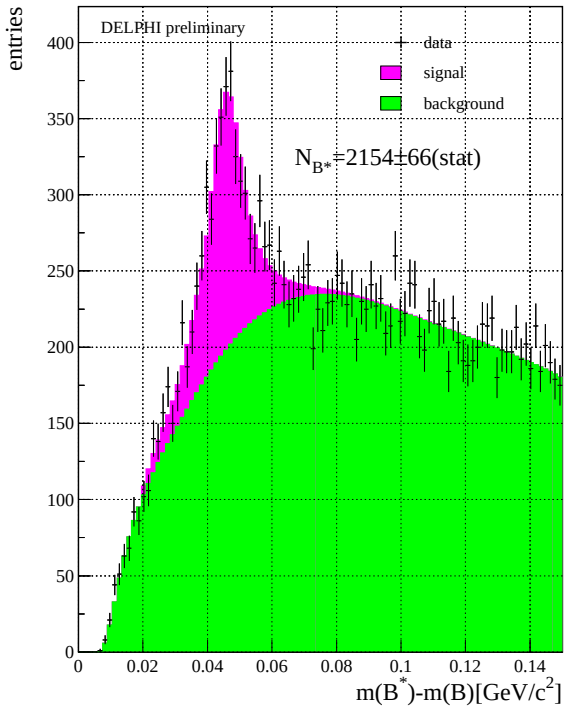

Figure 6.1: *The sum of all B^*-signal and background. Crosses are data. The signal is clearly visible.*

6.1.2 SELECTION OF B^+- AND B^0-ENHANCED SAMPLES

After a selection on the estimated B-energy[1] to reject poorly reconstructed hemispheres of $E_B > 20$ GeV, samples enhanced in B^+- and B^0-mesons are obtained by cutting on the output of the BHBN as follows:

- B^+ probability > 0.4 and
- B^0 probability < 0.3

defining the B^+ sample and,

- B^0 probability > 0.45 and
- B^+ probability < 0.25

defining the B^0 sample. An additional selection is made in the reconstructed mass difference of $\Delta m_{rec} < 150$ MeV/c^2 (i.e. the reconstructed B^*-B mass difference for data and simulation with a generated mass splitting of 46 MeV/c^2). These cuts select 7,400 (4,300) hemispheres in the $B^+(B^0)$ samples corresponding to a purity of 75% (66%) and an overall selection efficiency of 5.5% (3.2%).

[1]The one corrected by the polynomial is used here.

	B^+ sample	B^0 sample	left over
B^+	75.2%	15.7%	40.7%
B^0	18.6%	66.0%	44.0%
B_s	2.7%	11.1%	6.5%
b baryons	2.7%	6.7%	6.9%
others	0.8%	0.5%	1.9%

Table 6.1: *The composition of the three Monte Carlo samples.*

The hemispheres that do not pass the enhancement cuts, totalising 41,500, are put into a third sample and are also included in the fit. This approach is found to optimise the statistical error. The composition of the three Monte Carlo samples is shown in table 6.1. The data are divided into three samples following the same procedure.

Additional weighting factors are applied to the Monte Carlo in order to account for known sources of discrepency between data and simulation:

There is one for the current world average measurements of B^+, B^0, B_s and Λ_b lifetimes and b-species production fractions. The actual values taken can be found in [86, 87]. Another weight has been constructed to correct the fragmentation function in the Monte Carlo data to agree with the measurement [88].

There was a further weight accounting for imperfect detector modelling, based on a hemisphere quality factor from BSAURUS. This was coded as an integer word flagging: the number of tracks rejected by the standard track selections, the number of *ambiguous*[2] tracks, the number of reconstructed hadronic interactions [81] and the number of tracks failing the quality selections of the DELPHI b-tagging package. The weight was constructed by taking the ratio of suitably normalised distributions of hemisphere quality in data and simulation. This was repeated separately for 12 different classes of hemisphere track multiplicity leaving the overall track multiplicity essentially invariant under the application of the hemisphere quality weight.

6.1.3 The Fit Procedure

The DELPHI simulation data set was originally generated with a B^*-B mass difference of 46 MeV/c^2 for all B-meson types but can be used to test mass differences for B^+ and B^0 individually in the following way. The first step is to calculate the measurement residuals of the B-energy, photon energy, the angle between the B- and the B*-momentum vectors and the photon and B*-momentum vectors on an event-by-event basis. New 'true' values for the B-energy, the photon energy, and the two angles are calculated for other mass differences. The B*-momentum and the decay angle of the photon in the B*-rest frame are fixed during this process to the values taken from the original simulation. Finally the residuals are added to the new 'true' values for the energies and the angles to get new 'measured' values. This effectively calculates the B* mass distribution for each sample (including the non-Gaussian tails) for any value of $\Delta m = m(\mathrm{B}^*) - m(\mathrm{B})$.

In order to obtain, in the simulation, reconstructed B*-mass distributions that vary in a smooth and well behaved way as a function of the generated mass splitting value, it has

[2] An ambiguous track is defined to have reconstructed hits that could equally well be associated with a neighbouring track.

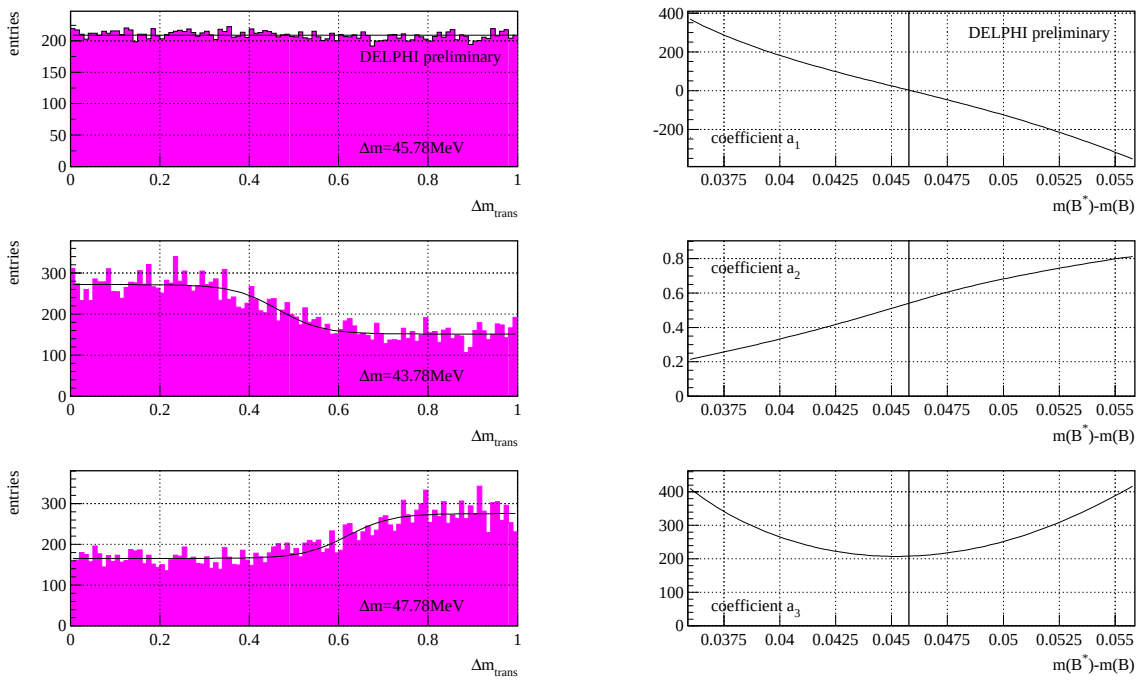

Figure 6.2: *The transformed mass splitting distribution for B^* and the result of the sigmoid fits for three different splittings (left). The coefficients a_i of the sigmoid function in dependence of the mass splitting (right). The line shows the chosen mass splitting value for determing the transformation.*

been found necessary to apply a transformation to the mass distributions before the fit. The signal (i.e. B* candidate) mass distribution valid for the world average mass splitting value of 45.78 MeV/c^2 [4] is first transformed into a uniformly distributed variable Δm_{trans} in the range [0,1] applying the method described in section 4.1.2. This transformation function is applied to all other distributions, i.e. the signal mass distribution for other splitting values, the background distribution and the data distribution. The transformed signal distributions are then fitted by the following sigmoid function:

$$s(\Delta m_{trans}) = a_1 \cdot \left(\frac{2}{1 + \exp[(-a_2 + \Delta m_{trans})/0.05]} - 1 \right) + a_3 \,. \tag{6.1}$$

In a final step, the resulting coefficients a_i are fitted by B-splines [63] as a continuous function of the mass splitting Δm (see figure 6.2). In doing so, smooth mass distributions can be generated for any input mass splitting value, thus ensuring a stable behaviour at each step of the final measurement fit as the mass splitting value is scanned over.

6.2 RESULTS

The transformed data distributions are fitted to the transformed simulation backgrounds and simulated B* signals by a log-likelihood fit. In total, two fits are performed. In the first fit, the flavour-averaged mass splitting is measured by fitting the sum of all samples to the data

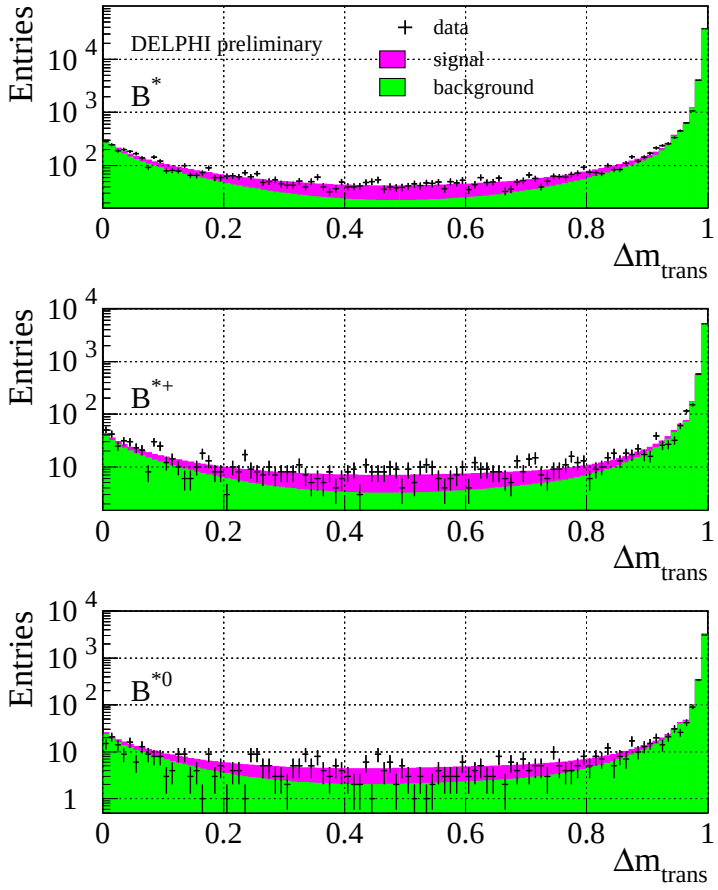

Figure 6.3: *Plots showing the best fits to the data for the case of the the flavour-averaged sample(top), the B^+ enriched(middle) and B^0 enriched sample(bottom).*

distribution. The fit parameters are the flavour-averaged mass splitting plus the signal and background normalisations with the following result,

$$m(\mathrm{B}^*) - m(\mathrm{B}) = 45.83^{+0.36}_{-0.31}(\mathrm{stat})\ \mathrm{MeV/c^2}$$

In the second fit, the isospin mass splitting $\Delta_m^{+0} = m(\mathrm{B}_u^{*+}) - m(\mathrm{B}_d^{*0}) - m(\mathrm{B}_u^{+}) + m(\mathrm{B}_d^{0})$ is measured by fitting the three data samples (i.e. B^{*+}-enhanced, B^{*0}-enhanced and the remaining) separately to the corresponding distributions in the simulation. The fit parameters are the mass splitting, the signal and background normalisations and Δ_m^{+0}. The mass splitting of the B_s-meson is fixed to the measurement of [4, 89]. The fit result was:

$$\Delta_m^{+0} = -0.2 \pm 1.4(\mathrm{stat})\ \mathrm{MeV/c^2}$$

These fit results are displayed in figure 6.3.

varied quantity	variation	error[MeV/c^2] for flavour-averaged	error[MeV/c^2] for isospin splitting
enhancement cuts	± 0.05	-	0.5
mass splitting of B_s	47.0$\pm$2.6 MeV/c^2	-	0.4
method	see section 6.2	0.31	0.4
B energy distribution	weight on/off	0.06	0.4
production fractions	see [87]	0.10	0.3
purity	$\pm 10\%$	-	0.1
b-tag variable	± 1.0	0.08	0.1
hemisphere quality	weight on/off	0.05	0.1
B energy selection	± 10 GeV	0.02	0.1
lifetimes	see [86]	0.03	-
detector resolution	smearing on/off	0.03	-
total		0.35	0.9

Table 6.2: *Summary of systematic uncertainties.*

Table 6.2 lists the assigned systematic contributions to the two measurements. The b-hadron lifetimes and production fractions, that formed part of the Monte Carlo weight described in section 6.1.2, are varied within the one standard deviation errors on their assigned values [4]. The other components of the Monte Carlo weighting, due to the B-fragmentation function and hemisphere quality, are independently switched off and the resulting change observed is assigned as a systematic uncertainty.

Selection values in the analysis applied to the BHBN b-species enhancement network, the event b-tagging and the weakly decaying B-energy estimate, are varied within the ranges given in table 6.2. Half of the full variation in the result is assigned as a systematic uncertainty. All these ranges have been determined by a scan over the variable considered. The value of the cut where the measurement started to give at least twice the error at the working point chosen has been taken to evaluate the systematic error due to this effect. This is not necessarily true for the lower and upper bound of the range since it has been decided to take symmetric ranges.

For the case of the isospin splitting measurement, where $m(B_s^*)$-$m(B_s)$ is fixed to the measurement of [4, 89], a systematic error is assigned based on the variation of Δm_s within the measured one standard deviation range.

The effect of the imperfect detector resolution modelling is estimated by an attempt to better match the track impact parameter and error (with respect to the primary vertex) between simulation and data according to the prescription detailed in [73]. The full variation in the result is assigned as a systematic uncertainty.

The effect of under- and overestimating the B^+ and B^0 purities in the enhanced samples is accounted for by varying the purity within its uncertainty of $\pm 10\%$. This is twice the value used in [85] and is conservative. The fixed B-mass is varied within its error. The effect is negligible for both measurements.

Systematic uncertainties due to the method itself are accounted for as follows: The un-

derlying mass difference value Δm_{ref}, valid when the signal distribution is transformed to a uniform distribution (and thus the point at which the transformation is determined), is varied by ± 1 MeV. In addition, the number of bins of the distributions and the step size for the determination of the sigmoid function coefficients are doubled and halved respectively. In all cases, half of the total change in the result has been assigned as a systematic uncertainty. As an extra check, the specific choice of the signal distribution transformation described in section 6.1.3, is examined and a systematic uncertainty of 0.3 MeV/c^2 is assigned. The method errors were added in quadrature and are denoted 'method' in table 6.2.

6.2.1 Discussion of the Result

For the samples of Z^0 decays collected by DELPHI in 1994 the flavour-averaged and the isospin mass difference of B^* and B have been measured, the latter for the first time. The analysis isolated b hadron candidates with neural network techniques which were used to exploit the physical properties of inclusive b-hadron decays. Based on enhanced samples of $B^+(B^0)$ containing 7,400 (4,300) hemispheres a maximum likelihood fit yielded the following preliminary results: for the flavour-averaged mass difference

$$m(\mathrm{B}^*) - m(\mathrm{B}) = 45.83^{+0.36}_{-0.31}(\mathrm{stat}) \pm 0.35(\mathrm{syst})\ \mathrm{MeV/c^2}$$

and for the isospin splitting of the mass difference

$$\Delta^{+0}_m = -0.2 \pm 1.4(\mathrm{stat}) \pm 0.9(\mathrm{syst})\ \mathrm{MeV/c^2}$$

The measurement of the flavour-averaged mass splitting is consistent both with the previous DELPHI measurement and the current world average. The isospin splitting lies within the limit given by the previous DELPHI analysis [67].

These results give a hyperfine splitting of the charged B-meson of

$$m(\mathrm{B}^{+*}_u) - m(\mathrm{B}^+_u) = 45.7 \pm 0.9\ \mathrm{MeV/c^2}$$

and for the non-strange neutral B-meson

$$m(\mathrm{B}^{0*}_d) - m(\mathrm{B}^0_d) = 45.9 \pm 0.9\ \mathrm{MeV/c^2}$$

Together with the world average of $m(\mathrm{B}^0_d) - m(\mathrm{B}^+_u)$ of 0.33$\pm$0.28 MeV/c^2 [4] follows a mass splitting of

$$m(\mathrm{B}^{*0}_d) - m(\mathrm{B}^{*+}_u) = 0.5 \pm 1.7\ \mathrm{MeV/c^2}.$$

This is the first measurement where B^*_u- and B^*_d-mesons are discriminated.

6.3 Outlook

In principle, it should be possible to use the B_s-identification network of BSAURUS for enriching B^*_s-mesons in the same way as $\mathrm{B}^*_{u,d}$-mesons and thus to measure the splitting between the B^*_s- and B_s-meson. A combined measurement of all three splittings could possibly reduce the uncertainties on the measurement. The contamination of B_s-mesons in the B^0-enriched sample could be lowered by the use of the B_s-identification network as well. With this method, it would also be possible to search for b-baryons decaying electromagnetically by using the b-baryon identification network.

Chapter 7

Study of Excited b-Hadrons

7.1 Event Selection

Multihadronic events are selected by applying the cuts listed in section 4.3. Hemispheres are accepted if the following criteria are satisfied:

- $|\cos\Theta_{thrust}| < 0.7$ (Θ_{thrust} is the angle between the thrust axis and the beam direction),
- the RICH detectors and the vertex detector worked efficiently,
- the event is tagged as a $Z \to b\bar{b}$ event by the standard DELPHI b-tagging package 4.8.2 with a selection of >0.0 in this quantity,
- the secondary vertex fit from the BSAURUS package 5.1.2 fulfills the internal conditions for convergence and
- the hemisphere energy scaled by the beam energy is in the range of $[0.5, 1.1]$.

These cuts select $b\bar{b}$ events with a purity of 90% and an efficiency of 48%, as estimated from the simulation.

7.2 Q-value Reconstruction

The four-vectors of $B^{**}_{u,d}$-decay pion or B^{**}_s-kaon candidates are combined with the reconstructed four-vector of the B-candidate (see 5.1) to form the $B^{**}_{u,d}$- and B^{**}_s-candidate respectively. The Q-value is defined by

$$Q = m(B\pi) - m(B) - m(\pi) \tag{7.1}$$

in the case of $B^{**}_{u,d}$-mesons, where $m(B\pi)$ is the invariant mass of the $B^{**}_{u,d}$-candidate, $m(B) = 5.279$ GeV/c^2 is the mass of the B-candidate and $m(\pi) = 0.1396$ GeV/c^2 is the charged pion mass [4]. In the case of B^{**}_s-mesons, the Q-value is defined by

$$Q = m(BK) - m(B) - m(K) \tag{7.2}$$

where $m(BK)$ is the invariant mass of the B^{**}_s-candidate and $m(K) = 0.4937$ Gev/c^2 is the charged kaon mass. Due to the inclusive approach, there is a problem in the Q-value

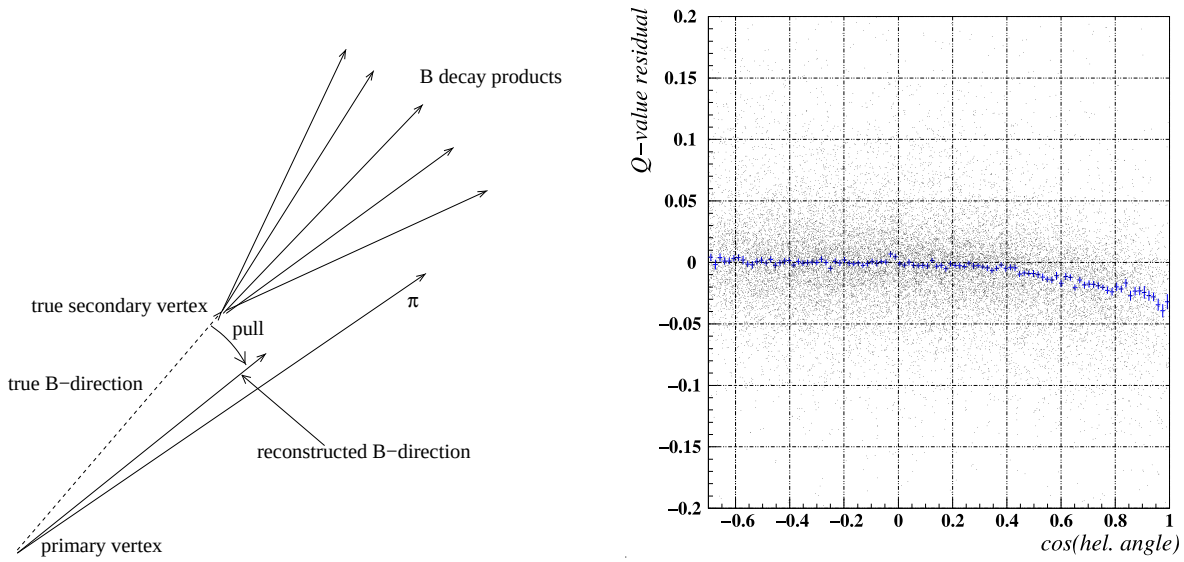

Figure 7.1: *The secondary vertex and hence the reconstructed B-direction is biased when the B^{**}-decay pion coming from the primary vertex is included in the reconstructed secondary vertex (left). This also leads to a bias of the reconstructed Q-value for small helicity angles as evaluated from the simulation(right). Crosses indicate the median of the distribution in each bin.*

reconstruction. The decay pion/kaon of the B^{**} has the same properties as the decay products of the weakly decaying b-hadron but it comes from the primary vertex. Thus, it can be assigned to the secondary vertex and to the primary vertex as well by the Track Net, especially for small helicity angles. If the decay pion/kaon is included in the secondary vertex the latter is biased towards the flight direction of the first as illustrated in figure 7.1 on the left side. Since the B-energy estimate is based on the standard BSAURUS secondary vertex it is also biased by that, with the consequence that the Q-value is also biased. This is shown on the right of figure 7.1 but is partially solved by using the algorithms described in section 5.1.4, as only tracks with a Track Net output larger than 0.5 are used for them, and for enriching B^{**}-mesons only tracks with a Track Net output lower than 0.5 are used. The direction of the B-momentum is estimated by the connection from primary to secondary vertex. This is used in the calculation of the Q-value. But there is still a bias in the B-energy and in the reconstructed secondary vertex for the case when the standard secondary vertex is used because the other algorithms have failed. To remove this bias a neural network has been trained to correct for it. In this case, the output of the network is not a probability for classifying but a full probability density function as described in section 4.1.2. This method also delivers an estimate of an error in the corrected Q-value giving the possibility only to use good resolution signal decay track candidates. The training of the Q-value neural network is done with the same special Monte Carlo as the $B^{**}_{u,d,s}$-enrichment networks, separately for $B^{**}_{u,d}$- and B^{**}_{s}-mesons by taking the adequate variables for pions and kaons respectively. Only signal pions have been used which have passed the same precuts that have been applied for the single enrichment networks. The networks consist of 42 input nodes (bias node included), 15 nodes in the hidden layer and 20 output nodes. They have been trained on the correction factor $\Delta Q = Q_{rec} - Q_{true}$, where Q_{rec} is the Q-value calculated from equations 7.1 and 7.2

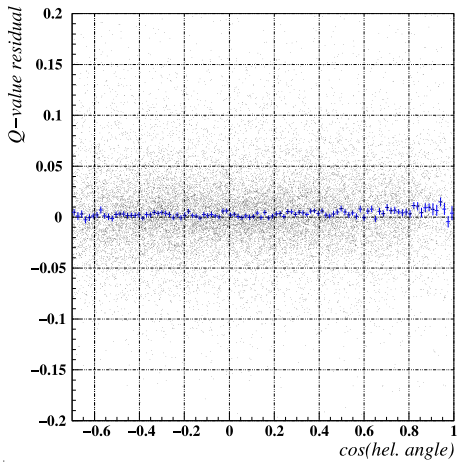

Figure 7.2: *The Q-value resolution versus the cosine of the helicity angle showing that the corrected Q-value is bias-free as evaluated from the simulation. Crosses indicate the median of the distribution in each bin.*

respectively and Q_{true} is the generated one. The input variables are:

- Q_{rec} as described above,
- four other Q-value estimates with different four-vectors of the b-hadron, namely from the rapidity algorithm, the direction of the momentum taken from the connection of primary to the standard BSAURUS secondary vertex, the corrected energy and the corrected energy by a neural network (see section 5.1.5),
- four corresponding Q-value estimates where the signal track is explicitly removed from the b-hadron by subtracting its four-vector from the one of the b-hadron,
- the square of the difference between these eight estimates and Q_{rec},
- the corrected B-energy,
- the B-energy from the rapidity algorithm,
- a Track Net output weighted B-energy estimate,
- the energy of the jet in the hemisphere most likely originating from a b-quark,
- the total reconstructed hemisphere energy scaled by the beam energy,
- an estimate of the centre-of-mass energy E_{cm} given by equation 5.3 where M_{recoil} is based on charged tracks only; in the hemisphere containing the B-candidate, only tracks likely to have originated from the fragmentation process are selected (by use of the Track Net (see section 5.1.3) but all tracks are used in the opposite hemisphere,
- a further estimate of E_{cm} as given by equation 5.3 where neutrals from the opposite hemisphere are also included in the formulation of M_{recoil},

- an estimate of the missing p_T between the B-candidate direction and the thrust axis calculated using only fragmentation tracks in the same hemisphere as the B-candidate (via use of the Track Net) and all tracks in the opposite hemisphere; the calculation is repeated for two different definitions of the b-hadron's direction: one being the vector pointing from the reconstructed primary vertex to the reconstructed secondary vertex and the other one given by the vector $\vec{p}_{raw}$,
- the mass at the reconstructed secondary vertex,
- the mass at the B-decay vertex estimated by the rapidity algorithm,
- the information if a lepton with high transverse momentum has been present in the hemisphere,
- the rapidity of the decay track,
- its Track Net output,
- the cosine of its helicity angle,
- its opening angle,
- the distance between the primary and the best existing secondary vertex,
- the error on that,
- the significance of that distance,
- a variable telling which secondary vertex algorithm has been used,
- the difference of the Track Net output between the track with the lowest output above 0.5 and the one with the highest output below 0.5,
- the error on the Θ- and
- the ϕ-component of the B-direction from the standard secondary vertex,
- the event thrust value and
- the hemisphere quality.

That this network works successfully is shown by the fact that the corrected Q-value is nearly bias free as illustrated in figure 7.2. Applying the network on the background leads to a shift in the background of the Q-value distribution. But this is not a problem as there is no peak in the corrected background distribution, thus not faking a signal [90].

7.3 Analysis of $B^{**}_{u,d}$-Mesons

The reconstruction of the Q-value and the enrichment of B^{**}_u- and B^{**}_d-mesons are the keys for the analysis presented in this chapter. This is done via neural network approaches: the Q-value is reconstructed via the network described in section 7.2 and the discrimination of the two different excited B-meson types is done with the help of the b-species network (see

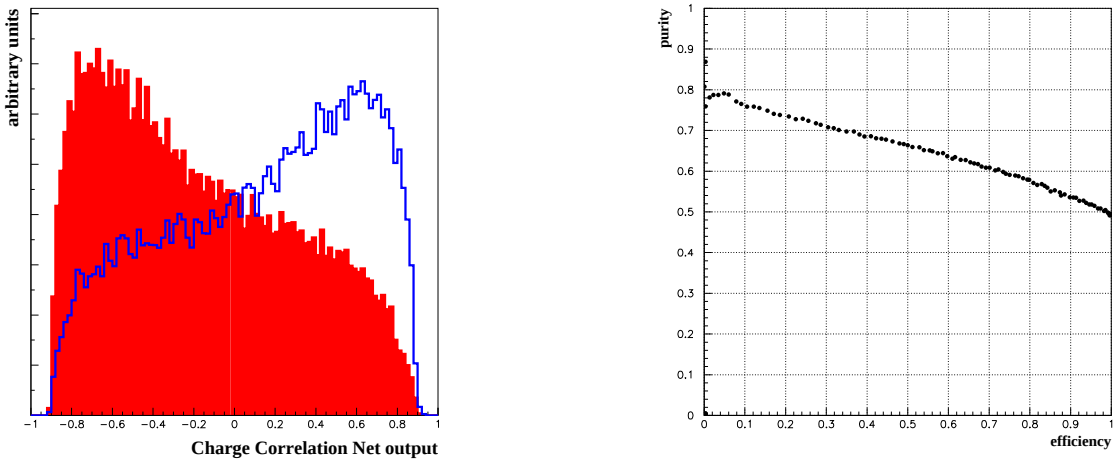

Figure 7.3: *Left: The separation of tracks with negative correlation (solid line) and for positive correlataion (filled area). Right: The performance of the charge correlation network.*

section 5.2.2 and by combining charge correlation information in another neural network (*ChCorr Net*). The enrichment is done with the network introduced in section 5.2.3. Only charged pions are considered, thus the decays $B_u^{+**} \to B_d^0\pi^+$, $B_d^{0**} \to B_d^+\pi^-$ and their charge conjugated decays. Therefore, the charge of the pion and the charge of the b-quark inside the B-meson are correlated with each other.

7.3.1 The Charge Correlation Network

The charge correlation network consists of 7 input nodes (including the bias node), 20 nodes in the hidden layer and one output node. It is trained on the correlation between the flavour of the b-quark in the weakly decaying b-hadron and the charge of the considered track using $b\bar{b}$-Monte Carlo events and NeuroBayes®. A negative correlation (i.e. charge of the b-quark contained in the b-hadron $\times$ pion charge < 0) is assigned a value of 1, a positive correlation a value of -1. Thus, signal pions from B_d^{**0}-meson decays should have a ChCorr Net output near 1 and signal pions from B_u^{**+}-meson decays near -1. The six input variables to the network are the following, each multiplied by the charge of the B^{**}-decay pion candidate:

- the difference between this hemisphere's jet charge and the one of the opposite hemisphere,
- the decay flavour net combining the information of both hemispheres,
- the sum of track charges (but excluding the decay pion candidate) weighted by the track's probability to originate from 'beyond' or from 'this side' of the secondary vertex w.r.t the B-candidate's flight direction,
- the same-hemisphere B^+-decay flavour net output combined with the same-hemisphere production flavour net of the opposite hemisphere and
- the likelihood-ratio based production flavour tag for B^0 and B_s (see section 5.2.1).

The separation power of the network is illustrated in figure 7.3.

7.3.2 CHOICE OF MODEL

The expectations and existing information is used to constrain some variables. The results from c-hadrons are used to fix some parameters in the fit, especially for the broad states as the sensitivity is not good enough to be able to freely fit their contribution from data.

Studies showed that the decays $B^{**} \to B\rho$, $B\pi^+\pi^-$ can be neglected from the signal parametrisation since there is no evidence for these decays [91], in agreement with the non-observation in the charm sector.

For the narrow $B^{**}_{u,d}$-states, three Gaussians are fitted, accounting for the two different decay modes of the B_2^* and for $B_1 \to B^*\pi$. For the mass splitting due to the decay into B^* and B respectively, $m(B^*) - m(B) = 45.78 \pm 0.35$ MeV/c^2 is used [4]. The mass splitting within the narrow doublet is left free in the fit. The relative ratio of $\Gamma(B_2^* \to B\pi^+)/\Gamma(B_2^* \to B^*\pi^+)$ is fixed to 1.1 ± 0.3 (see section 3.3.2). The two broad states are fitted by two relativistic Breit-Wigner functions. The mass difference between the B_1- and B_1^*-states is fixed to 0 ± 40 MeV/c^2. The splitting within the broad doublet is fixed to 45 ± 15 MeV/c^2. The relative fractions of the four $B^{**}_{u,d}$ -states are fixed by both spin and state counting.

There is a hint for a possible signal at a Q-value of about 500 MeV/c^2. This will be called '500-state' throughout this thesis. It is not interpreted as a broad $B^{**}_{u,d}$-state as the results from the charm sector do not support spin-orbit inversion (see section 3.3). Studies could not clarify whether this could be due to a resonant state, a wrong modelling of the fragmentation process, especially for the leading fragmentation particles, an analysis artefact or just statistical fluctuations. Therefore, two scenarios are considered in the fits: the first only fitted the narrow and broad $B^{**}_{u,d}$-states, the second additionally included the possible signal parametrised as a relativistic Breit-Wigner into the fit. In the following sections the results of both approaches are presented for both scenarios considered as well as their combinations.

7.3.3 SELECTION OF $B^{**}_{u,d}$-EVENTS

By applying the ChCorr Net and the b-species network a 'right-sign' (r.s.) and a 'wrong-sign' (w.s.) sample for B_u^{**+}- and B_d^{**0}-mesons are defined as follows:

1) $ChCorr > 0.0$, $\quad B_d^{**0} \to B^+\pi^-$, 'right $-$ sign'

2) $ChCorr < 0.0$, $\quad B_d^{**0} \to B^+\pi^+$, 'wrong $-$ sign'

3) $ChCorr > 0.3$, $\quad B_u^{**+} \to B^0\pi^-$, 'wrong $-$ sign'

4) $ChCorr < -0.3$, $B_u^{**+} \to B^0\pi^+$, 'right $-$ sign'

For the first two samples, only hemispheres are used which fulfill the cuts B^+-net > 0.4 and B^0-net < 0.4. For the last two samples the corresponding cuts are B^0-net > 0.4 and B^+-net < 0.4 leading to a B^+ (B^0) purity of 57% (48%) in the right-sign samples as estimated by the simulation. For this purpose only those B^{**}-candidates have been considered with a reconstructed Q-value lower than 1.0 GeV/c^2. This selection is applied to data and Monte Carlo events respectively. Additionally, a cut on the B^{**}-enhancement network is applied at 0.3. The relative composition of both right-sign samples is shown in table 7.1. The B_d^{0**} (B_u^{+**}) purity estimated by the simulation is approximately 21% (19%) with an efficiency

	B^{0**} r.s.	B^{+**} r.s.
B^+	71.3%	23.0%
B^0	20.0%	61.9%
B_s	2.4%	5.2%
b-baryons	2.0%	5.6%
others	4.3%	4.3%

Table 7.1: *The composition of right sign samples.*

of about 58% (49%) These values have been obtained by using all the background in the right-sign sample, i.e. the background over the whole considered Q-value range.

7.3.4 The Fit Procedure

Combined fits to the four samples defined above are performed according to the description given in section 7.3.2. The background shapes $BKG(Q)_i$ in each of the four samples $i = 1, ..., 4$ are taken from the Monte Carlo expectation and corrected with the following cubic form,

$$BKG(Q)_{\mathrm{fit},i} \quad = \quad BKG(Q)_{\mathrm{MC},i} \cdot N_i \cdot (a + b \cdot Q + c \cdot Q^2 + d \cdot Q^3)\,. \tag{7.3}$$

The parameters N_i, a, b, c and d are allowed to be free in the fit. a could be different for the B^0_d- and B^+_u-enhanced samples respectively; b, c and d are the same for all four samples. Studies have revealed that the Monte Carlo background shape is probably a reasonable model of the data over most of the Q-value spectrum but that differences are likely to occur particularly at the low and high Q-values. This is reflected in substantial improvements to both the fit quality and stability when the background shape is corrected in the form described above.

The full list of free parameters in the fits to the measured Q-value distribution is:

- the area of the Gaussian component for B^{0*}_{d2} decaying to $B\pi$. The corresponding B^{+*}_{u2}-area is then fixed by imposing the constraint that the production rates (i.e. the acceptance-corrected Gaussian areas) for B^{0*}_{d2} and B^{+*}_{u2} are equal. The areas of the two other Gaussian components are fixed according to section 7.3.2.
- The Gaussian mean (constrained to be the same for $B^{0*}_{d2} \to B^+\pi^-$ and $B^{+*}_{u2} \to B^0\pi^+$). The other means are fixed according to section 7.3.2 but
- the hyperfine splitting within the narrow doublet assumed to be the same for B^{0**}_d and B^{+**}_u.
- The Gaussian width for $B^{0*}_{d2} \to B^+\pi^-$ and for $B^{+*}_{u2} \to B^0\pi^+$. The widths of the other narrow components are assumed to be the same for B^{0**}_d and B^{+**}_u respectively.
- The background parameters N_i, a, b, c and d.

The relative fraction of $B^{0**}(B^{+**})$ in the depleted sample to the one in the enhanced sample is fixed to the Monte Carlo prediction (see table 7.2). When including the 500-state in the fit, the three additional parameters are:

	B^{0**}	B^{+**}
B^{0**} r.s.	1.0	0.390
B^{0**} w.s.	0.088	0.449
B^{+**} w.s.	0.136	0.374
B^{+**} r.s.	0.057	1.0

Table 7.2: *The relative fractions of $B^{**}_{u,d}$-mesons in the four samples normalised to the number of $B^{**}_{u,d}$-mesons in the corresponding right-sign samples.*

- the ratio of the 500-state's rate over the (fitted) rate of the B_1-state,
- the most probable Q-value of the Breit-Wigner and
- the full-width at half-maximum of the Breit-Wigner.

All these variables are assumed to be the same for the charged and neutral cases. An example for a fit including the 500-state is shown in figure 7.4.

7.3.5 RESULTS

For the 500-state, the fit results are listed in table 7.3. But this should not be interpreted as a physical state. Therefore the results for the two counting schemes have not been averaged.

The results for the $B^{**}_{u,d}$-states are presented for each of the four scenarios considered in the fit: with/without 500-state and spin/state counting. The fit result and the error is scaled by a factor of 1.5 to account for the unmeasured decays $B^{**}_{u,d} \to B^{+0}_{u,d}\pi^0$. The systematic uncertainties on these results are studied by considering effects due to the background correction and the $B^{**}_{u,d}$-enrichment. The first is obtained by varying the order of the polynomial, used in the correction, by $\mp$ one order and taking the full difference of both cases as uncertainty. This leads to the asymmetric error for the rate measurement. The latter is obtained by varying the cut on the $B^{**}_{u,d}$-enrichment network. For the Q-value, another systematic uncertainty has to be considered arising from the uncertainty in the energy scale of $< 1\%$ [88]. This translates into an error for the Q-value of the B^*_2 of 3 MeV and for the 500-state this uncertainty is 5 MeV. To get the total systematic error these uncertainties are added in quadrature. The values for all scenarios are listed in table 7.4, the average of the scenarios is given in table 7.5. The uncertainty denoted by 'scen.' contains the errors due to the choice of the scenario (i.e. with and without the 500-state) and the ones estimated by varying the parameters fixed in the fit within the 1σ-uncertainties given in section 7.3.2. The average of the two counting schemes is given as well. The uncertainty due to the model is the one due to the scenario and due to the counting scheme added in quadrature.

The Q-value of the decay $B^*_2 \to B\pi$ corresponds to a B^*_2-mass of 5742 ± 12 MeV/c^2. This is in good agreement with the results listed in table 3.7. From this and the result from the splitting, a B_1-mass of 5727 ± 19 MeV/c^2 follows.

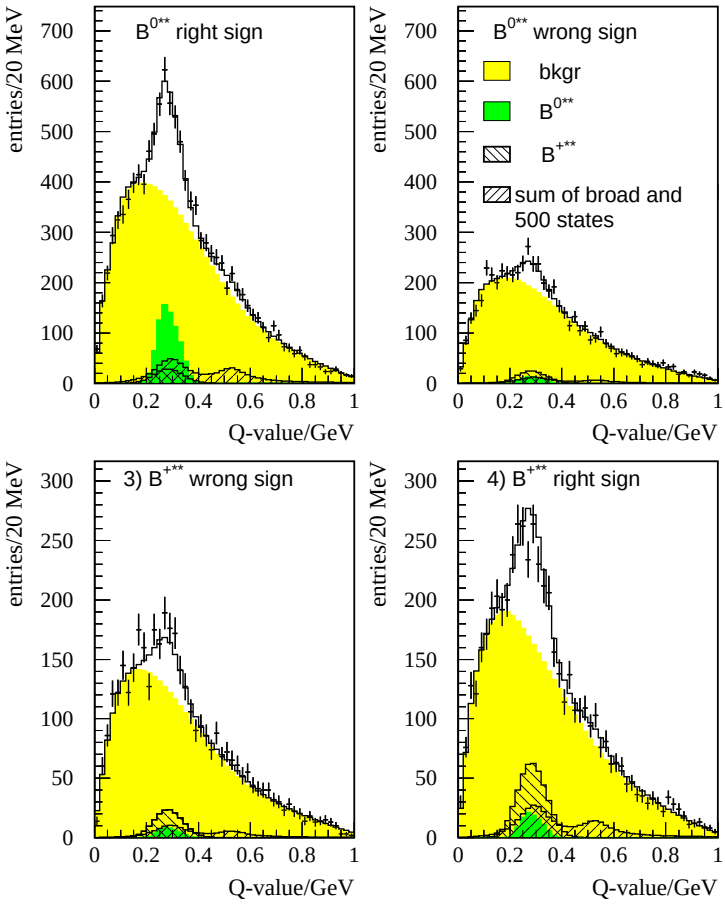

Figure 7.4: *An example for a fit result for the B^{**}_{ud}-analysis including the 500-state. The points are data, the open histogram shows the fit result. The other components are explained in the plot.*

Counting	500-state rate	Q(500-state)/(MeV/c^2)	FWHM/(MeV/c^2)
Spin	0.030±0.014±0.022	531±21±18	260±170±140
State	0.031±0.018±0.016	532±18±13	250±160±100

Table 7.3: *Fit results for the 500-state. FWHM denotes the full-width at half-maximum of the Breit-Wigner.*

Scenario	Counting	χ^2/ndof	Total $B^{**}_{u,d}$-rate	narrow $B^{**}_{u,d}$-rate	$Q(B^*_2 \to B\pi)/(MeV/c^2)$	$(m(B^*_2)-m(B_1))/(MeV/c^2)$
500 out	Spin	199/186	$0.132\pm0.014^{+0.030}_{-0.008}$	$0.088\pm0.009^{+0.019}_{-0.006}$	$319 \pm 7 \pm 5$	$13 \pm 13 \pm 4$
	State	199/186	$0.150\pm0.014^{+0.027}_{-0.008}$	$0.075\pm0.007^{+0.013}_{-0.004}$	$322 \pm 11 \pm 7$	$11 \pm 15 \pm 6$
500 in	Spin	187/183	$0.153\pm0.021^{+0.055}_{-0.011}$	$0.102\pm0.014^{+0.037}_{-0.006}$	$321 \pm 8 \pm 6$	$16 \pm 14 \pm 4$
	State	187/183	$0.174\pm0.020^{+0.043}_{-0.011}$	$0.087\pm0.010^{+0.022}_{-0.006}$	$328 \pm 10 \pm 7$	$17 \pm 14 \pm 6$

Table 7.4: *$B^{**}_{u,d}$-fit results for the different scenarios. The first error is the statistical one, the second is the systematical one. The systematics quoted for the rates are due to physics effects, i.e. background correction and enrichment, only. The ones for the Q-value also contain the error due to the uncertainty in the energy scale.*

	Total $B^{**}_{u,d}$-rate	narrow $B^{**}_{u,d}$-rate	$Q(B^*_2 \to B\pi)/(MeV/c^2)$	$(m(B^*_2)-m(B_1))/(MeV/c^2)$
Spin	0.143 ± 0.014(stat.) $^{+0.030}_{-0.008}$(syst.)±0.012(scen.)	0.095 ± 0.009(stat.) $^{+0.019}_{-0.006}$(syst.)±0.008(scen.)	320 ± 7(stat.) ±6(syst)±9(scen.)	15 ± 13(stat.) ±4(syst.)±5(scen.)
State	0.162 ± 0.014(stat.) $^{+0.027}_{-0.008}$(syst.)±0.016(scen.)	0.081 ± 0.007(stat.) $^{+0.013}_{-0.004}$(syst.)±0.008(scen.)	325 ± 10(stat.) ±7(syst.)±9(scen.)	14 ± 14(stat.) ±6(syst.)±6(scen.)
Average	0.153 ± 0.014(stat.) $^{+0.027}_{-0.008}$(syst.)±0.015(model)	0.088 ± 0.007(stat.) $^{+0.013}_{-0.004}$(syst.)±0.011(model)	323 ± 7(stat) ±6(syst)±9(model)	15 ± 13(stat.) ±4(syst.)±5(model)

Table 7.5: *Average of the two scenarios from table 7.4 for both spin and state counting. The uncertainty due to the scenarios is denoted as 'scen.' and also includes the variations due to changes in the fixed parameters (see section 7.3.2). Additionally, the average over the two counting schemes is given. The model error is given by the uncertainties due to the scenario and the counting scheme, added in quadrature.*

7.4 Analysis of B_s^{**}-Mesons

A search for B_s^{**}-states was made within the same framework as for the B_{ud}^{**}-reconstruction. The analysis reconstructed the decay channel $B_s^{0**} \rightarrow B^+K^-$ so that, to first order, the situation is analogous to the B_{ud}^{**}-search with the identification of a decay-K^- instead of a negatively charged pion.

7.4.1 Selection of B_s^{**}-Events

Hemispheres containing a B_s^{**}-meson are selected by applying the precuts to the training sample of the B_s^{**}-enhancement network. The training has been done with various cuts on the kaon network corresponding to kaon purities of approximately 42%, 66% and 80% to evaluate the working point. The first purity has been chosen. Further enrichment is done with the B_s^{**}-enhancement network. Selection cuts are applied to the data sample which optimise the statistical error on the B_s^{**}-rate determination. A cut is made in the $\sigma(Q)$ versus Q-space such that the best 40% of all reconstructed Q-values are retained for the fit. From a certain B_s^{**}-purity on, a single working point cannot be chosen as the errors are very similar on the measurement (see below).

7.4.2 The Fit Procedure

Although as mentioned in Section 3.3 we might expect to see up to three separate peaks in the Q-value distribution of the B_s^{**}, data show only one significant feature at a Q-value of around 80 MeV/c^2 (see figure 7.6). Further, the characteristic width of this feature is consistent with the expected resolution at this Q-value, suggesting that we are looking at a single *narrow* resonance state or two states with a mass splitting between them that is small enough that it cannot be resolved. A complication to this picture comes from studies in the simulation of the Q-value residual (i.e. the difference between the true and the reconstructed Q-value) of a single narrow resonance which have revealed that: (a) the resolution improves with harder cuts on the B_s^{**}-Enhancement Network output (and hence with increasing B_s^{**}-purity) and (b) the shape of the residuals contains a significant component from non-Gaussian tails. To accomodate this information in the fit to the data Q-value distribution, the B_s^{**}-signal shape is fixed to be that of the residual distribution obtained from a delta-function resonance centered at 80 ± 10 MeV/c^2. Double Gaussian parametrisations are found to reproduce the shape well and the procedure is repeated for different cuts on the B_s^{**}-Enhancement Network. In the following discussion, this parametrisation is refered to as 'signal'.

The background shape is parametrised by the following form [92]:

$$BKG(Q) \quad = \quad P_1 \left[Q(P_4 - Q)\right]^{P_2} \cdot \exp\left[-P_3\left(Q - \frac{P_4}{2}\right)\right], \tag{7.4}$$

with four free parameters P_1, P_2, P_3 and P_4. This choice is prefered over taking the shape from the simulation (as was the case for the B_{ud}^{**}-analysis) since for this analysis it was assumed that the background describes every component of the Q-distribution apart from the contribution from the narrow B_s^{**}-states. It is unlikely that the simulation can provide a reliable model of this background given the current lack of knowledge about the broad states, the contribution of three body decays of B_s^{**}-mesons, $L = 2$ radial excitations etc.

The signal plus background parametrisation was fitted to the Q-value distribution reconstructed in the data with the following quantities left free in the fit:

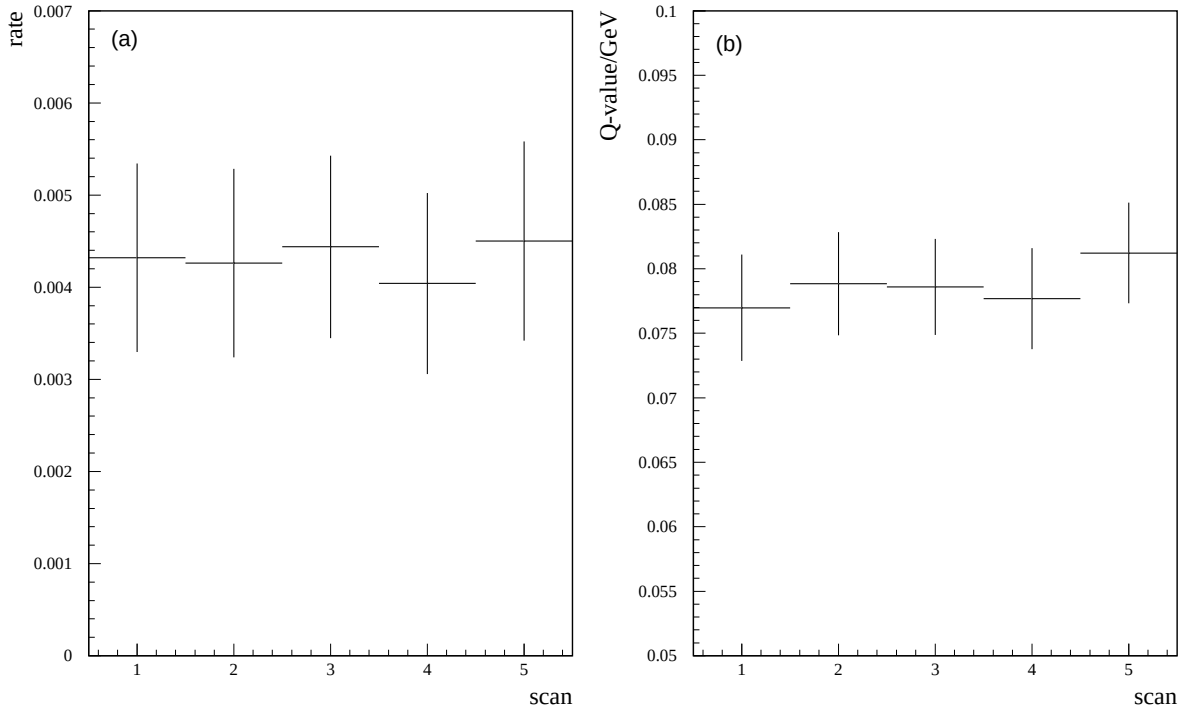

Figure 7.5: *Results for the signal rate (a) and mean Q-value (b) as a function of a scan over cuts on the value of the B_s^{**}-Enhancement Network.*

- the signal area
- the signal mean
- the four background parameters P_1 to P_4.

7.4.3 RESULTS

Figure 7.5 presents results for (a) the signal rate and (b) the mean Q value as a function of the cut value on the B_s^{**}-Enhancement Network. The overall stability of the results over a range of purities is evidence that the ansatz used to describe the signal and background components is reasonable.

Systematic uncertainties of the fit results are studied as a function of:

- replacing the background model by the shape found in the simulation and leaving the normalisation free in the fit,
- varying the Gaussian widths of the signal parametrisation by $\pm$ 10%,
- varying the areas of the narrow and broad Gaussian components of the double Gaussian signal parametrisation by $\pm$ 20% and $\mp$ 20% respectively,

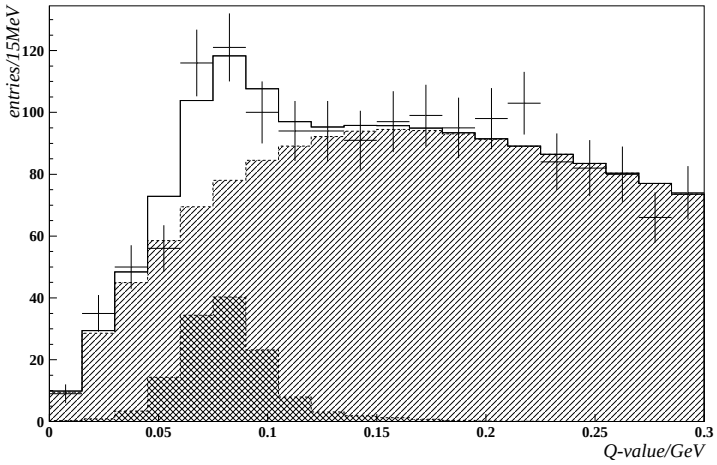

Figure 7.6: *An example fit to the data, corresponding to scan value 2 in figure 7.5. The points are data and the open histogram is the fit result. The hatched histogram shows the background component of the fit and the cross-hatched histogram shows the signal contribution.*

- energy scale and
- changing the kaon efficiency by -10%.

The last point is estimated by comparing the kaon efficiency for different cuts on the kaon net output in data and Monte Carlo for kaons from $D^{*+} \to D^0\pi^+$, $D^0 \to K\pi$ in a sample as pure as possible. This is done in the same momentum region where the B_s^{**}-decay kaons are expected. It is found that the MC efficiency overestimates the efficiency in data by at most 10%. This variation results in a change in the rate of +0.0011. A possible systematic error from a mismatch in the kaon purity between data and MC is included in the background systematic as the background is parametrised by an analytic function.

Since the extracted rates and Q-values are stable with respect to the B_s^{**}-purity and have very similar statistical errors point-to-point over the scan, central values are determined by

Systematic source	Uncertainty in Q [MeV/c^2]	Uncertainty in rate
Background shape	1.8	0.0008
Signal width	+0.2	+0.0006
Signal area	+0.3	−0.0005
Energy scale	0.8	-
Kaon efficiency	-	0.0006
Total	2.0	0.0013

Table 7.6: *Systematic errors on the Q value and the rate determination of B_s^{**}. The signs refer to the direction of the change induced by an upwards variation in the error source.*

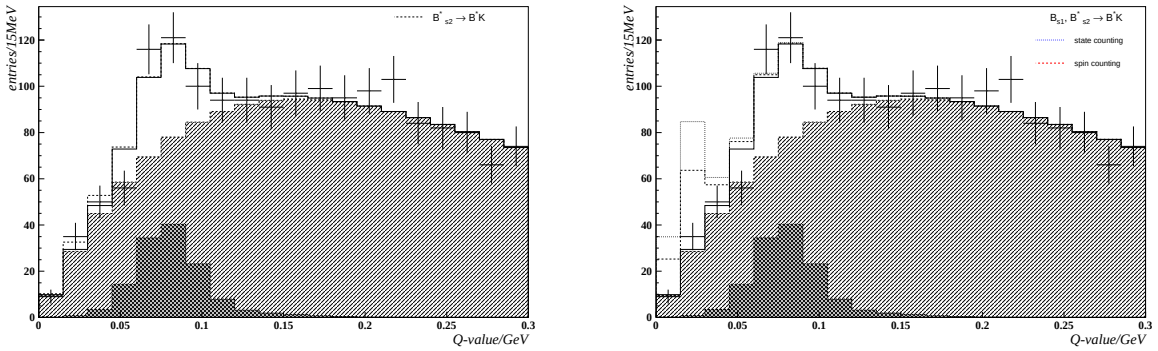

Figure 7.7: *The expected signals for the decay $B^*_{s2} \to B^*K$ (left) and for the decays B_{s1}, $B^*_{s2} \to B^*K$ predicted by HQET for spin and state counting (right). For both cases, the observed signal is interpreted as coming from the decay $B^*_{s2} \to BK$.*

averaging over the results in figure 7.5:

$$\begin{aligned} Q &= 79.0 \pm 4.0(\text{stat}) \pm 2.0(\text{syst})\,\text{MeV/c}^2 \\ \text{Rate} &= 0.0093 \pm 0.0020(\text{stat}) \pm 0.0013(\text{syst}) \end{aligned}$$

The rate value and errors have been scaled by a factor of two to account for the unmeasured channel $B^{**}_s \to B^0K^0$. The rate value is changed by half of the change due to the systematic error from the kaon efficiency. The systematic uncertainties resulting from the changes given above are listed in table 7.6. The significance of the reconstructed signal follows from the fitted area of the signal and the measured error on this quantity. As an example, the result for the fit shown in figure 7.6 is: signal size $= 134 \pm 32(stat.) \pm 12(syst.)$ i.e. a significance of 3.9σ.

7.4.4 Discussion of Results

As already mentioned in section 3.3 at least two peaks from B^{**}_s are expected. If the signal is interpreted as originating from the decay $B_{s1} \to B^*K$, one expects a signal from the decay $B^*_{s2} \to BK$ at a Q-value around 140 MeV/c^2. The precise Q-value depends on the B^*_{s2}-B_{s1} mass splitting. This peak should clearly be visible in the data as the reconstruction efficiency increases as a function of the Q-value. This interpretation is not supported by data.

If the signal comes from the decay $B^*_{s2} \to BK$ the decay mode $B^*_{s2} \to B^*K$ should be seen at a Q-value of about 33 MeV/c^2. But this decay mode is expected to be suppressed by a factor 1/10 compared to the first decay, in addition to the suppression of the observable signal due to the lowered acceptance for small Q-values. This interpretation gives a reasonable description of the data as shown in figure 7.7 on the left. However, the question remains where the signal from the decay $B_{s1} \to B^*K$ is. One would expect a signal at Q-values lower than 33 MeV/c^2. If a mass splitting of 13 MeV/c^2 is assumed a peak at a Q-value of 20 MeV/c^2 should be observable. The reconstruction efficiency at this Q-value is reduced by a factor of about 45%. This scenario is illustrated for the hypothesis of spin and state counting in figure 7.7 on the right and is not favoured by the data. However, the isospin forbidden decay channel $B_{s1} \to B^*_s\pi^0$ might be enhanced against the allowed decay mode near threshold and

therefore effectively reducing the expected signal. An evaluation similar to the one for the B_2^*-state given with equation 3.11 leads to a relative enhancement of this decay compared to the decay into B*K. The decays into $B_s^{(*)}\gamma$ may also be non-neglible. Thus, it seems to be quite reasonable that the B_{s1}-state decays mainly into $B_s^{(*)}$-mesons [93].

For these reasons, the most likely interpretation is that the observed signal originates from the decay $B_{s2}^* \to BK$. In this case, the measured Q-value corresponds to a mass of $m(B_{s2}^*) = 5852 \pm 4$ MeV/c^2. This result is in agreement with the OPAL measurement with a mass of 5853 ± 15 MeV/c^2 and with a production rate of 0.020 ± 0.006 [48].

The statistics are not high enough for the analysis to be sensitive to the broad B_s^{**}-states. In the current fit procedure, broad B_s^{**}-mesons decaying into $B^{(*)}K$ would be included in the background if they are above the threshold at all. But the results from strange D-meson decays give a strong hint that the broad B_s^{**}-mesons are below threshold, too (see section 3.3).

7.5 Search for $\Sigma_b^{(*)}$-baryons

The Q-value for $\Sigma_b^{(*)}$-baryons is defined in the following way

$$Q \;=\; m(\Lambda_b\pi) - m(\Lambda_b) - m(\pi) \tag{7.5}$$

where $m(\Lambda_b\pi)$ is the invariant mass of the $\Sigma_b^{(*)}$-candidate, $m(\Lambda_b) = 5.624$ GeV/c^2 [4] is the mass of the Λ_b-candidate and $m(\pi) = 0.1396$ GeV/c^2 is the charged pion mass. A neural network has been trained for correcting the reconstructed Q-value in the same manner as for the $B_{u,d}^{**}$-mesons (see section 7.2) by replacing the variables describing the weakly decaying B-mesons by the analogous ones describing the Λ_b-baryon, and also the same precuts have been used.

Since both decays $\Sigma_b^{+(*)} \to \Lambda_b\pi^+$ and $\Sigma_b^{-(*)} \to \Lambda_b\pi^-$ exist[1], there is no charge correlation between the charge of the b-quark inside the $\Sigma_b^{(*)}$-baryon and the charge of the decay pion. Thus, these baryons can only be enriched by the use of the Λ_b- and $\Sigma_b^{(*)}$-identification networks.

7.5.1 Selection of $\Sigma_b^{(*)}$-Events

Hemispheres containing a $\Sigma_b^{(*)}$-baryon are selected by applying the precuts to the training sample of the $\Sigma_b^{(*)}$-identification and Q-value correction networks. A loose cut is applied on the Λ_b-enrichment network corresponding to an efficiency of about 90% and a purity of about 12% (after applying the standard selection cuts mentioned in section 4.9) as estimated from the simulation. An additional cut is applied on the rank in a track list of the considered hemisphere sorted by the rapidity. This rank has to be smaller than 5. A cut on the $\Sigma_b^{(*)}$-identification network is applied at a value of 0.4. These cuts give a $\Sigma_b^{(*)}$-purity of about 12% in the Q-value range up to 150 MeV/c^2 as estimated from simulation.

7.5.2 Limit for $\Sigma_b^{(*)}$-Baryon Production

No signal can be observed in data in the Q-value range smaller than 0.3 GeV/c^2. But it is possible to extract a limit on the production rate of the $\Sigma_b^{(*)}$-baryons with the following

[1] The charge conjugated decays are included.

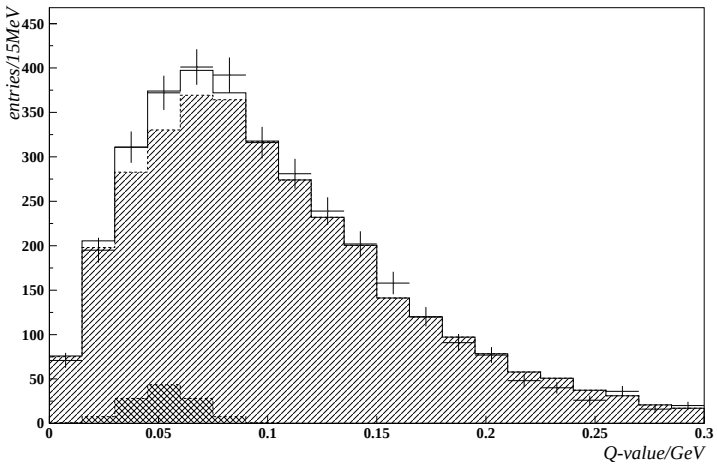

Figure 7.8: *The Q-value distribution used to extract the upper limit for the production rate of $\Sigma_b^{(*)}$-baryons. The crosses are data and the open histogramm is the fit result. The hatched histogram shows the fitted background and the cross-hatched histogram the signal.*

procedure. A possible narrow signal is described by a Gaussian with a width fixed to the expected resolution in each bin of the Q-value, the background is parametrised according to equation 7.3 but with the four free parameters a, b, c and d. With this ansatz, it is scanned over the Q-value and the measured Q-value distribution is fitted to determine the following upper limit on the production rate of a narrow $\Sigma_b^{(*)}$-resonance:

$$\frac{\sigma(\Sigma_b^{(*)}) \cdot \mathrm{BR}(\Sigma_b^{(*)} \to \Lambda_b \pi)}{\sigma_b} \quad < \quad 0.0124 \ @ \ 95\% \, \mathrm{CL}$$

This upper limit includes the charged and neutral $\Sigma_b^{(*)}$-baryons and the systematic uncertainties coming from variations in the $\Sigma_b^{(*)}$-purity and uncertainty in the background parametrisation similar to the uncertainties in the $\mathrm{B}_{u,d}^{**}$-analysis. The fit result used to extract this limit is shown in figure 7.8. Thus, the previous DELPHI measurement (see section 3.4) cannot be confirmed and is excluded by this limit.

7.6 OUTLOOK

By combining the reconstruction of B*-mesons described in chapter 6 and the methods explained in this chapter it could be possible to distinguish the different decay modes of the B**-mesons. At least, the reconstruction of the decays $\mathrm{B}_{u,d}^{**} \to \mathrm{B}^* \pi$ should be possible but maybe not with sufficient statistics. An analysis like this could clarify the situation with respect to the composition of the Gaussian signal describing the narrow states. But it is doubtful that this method would be more sensitive to the broad states.

Combining B*-mesons with a kaon could clarify the situation for B_s^{**}-mesons and if the interpretation of the observed signal, which is presented in this thesis, is right. But again, if statistics are sufficiently high for this is questionable.

The observation of broad $B^{**}_{u,d}$-states, Σ_b-baryons and other decay modes of B^{**}_s-mesons, and thus answering the open questions in this field, could be possible at hadron colliders, namely the Tevatron[2] or the LHC[3]. But in this environment, it is a difficult task to properly identify the decay tracks from excited b-hadrons. This would be much easier in a linear electron-positron collider which is planned for the future. This machine should at the latest be able to provide the answers to the open questions concerning excited b-hadrons.

[2] A proton-antiproton collider near Chicago/IL USA.
[3] A proton-proton collider scheduled to start 2007/2008 and replacing LEP.

Chapter 8

Conclusion

B*-mesons and excited b-hadrons have been studied in multihadronic Z^0-decays with the DELPHI detector at LEP. These measurements help to test the predictions of non-perturbative models based on HQET or the particular choice of a potential and so help to make progress in understanding the true nature of the QCD potential. Heavy hadrons are well appropriate for this since they can be considered the QCD equivalent to hydrogen. These measurements can be used as input for calculations on the lattice to improve their 'measurements'. Additionally, measuring the production rate of excited b-hadrons helps to minimise the uncertainty on the production rate of weakly decaying b-hadrons primarily produced in the e^+e^--annihilation process and can help to better understand the hadronisation process. Moreover, excited states can be used in tagging the b-quark flavour (i.e. b or $\bar{b}$) of a b-hadron at the time of its production. This is important for $B^0_{d,s}$-oscillation and CP violation studies at high energy colliders.

It was necessary for these measurements to separate B^+- and B^0-mesons from each other and from the other b-hadrons. The weakly decaying b-hadrons were reconstructed inclusively for this purpose. Besides, their reconstructed energy was corrected to take into account losses and inefficiencies. The separation of the hadrons was done by the use of neural networks.

The B*-mesons were reconstructed by combining the B^+- and B^0-mesons reconstructed in the way described above with the photons converted in front of the time projection chamber of DELPHI. Thus, one could get samples enriched with B^{+*}- and B^{0*}-mesons respectively and a depleted sample. By fitting the simulation to data, the isospin splitting of the ground state doublet's hyperfine splitting has been measured for the first time to be

$$m(B_u^{+*}) - m(B_d^{0*}) - m(B_u^+) + m(B_d^0) = -0.2 \pm 1.4(\text{stat}) \pm 0.9(\text{syst}) \text{ MeV/c}^2.$$

This results in a hyperfine splitting of the charged B-meson of

$$m(B_u^{+*}) - m(B_u^+) = 45.7 \pm 0.9 \text{ MeV/c}^2$$

and for the non-strange neutral B-meson of

$$m(B_d^{0*}) - m(B_d^0) = 45.9 \pm 0.9 \text{ MeV/c}^2.$$

Together with the world average of $m(B_d^0) - m(B_u^+)$ of 0.33±0.28 MeV/c^2 [4] follows a mass splitting of

$$m(B_d^{*0}) - m(B_u^{*+}) = 0.5 \pm 1.7 \text{ MeV/c}^2,$$

which herewith has been determined for the first time.

Orbitally excited B-mesons were reconstructed by combining the B^+- and B^0-mesons with pions and kaons respectively originating from the primary vertex. Neural networks were used to get enhanced and depleted samples of these mesons and to reconstruct a bias-free Q-value. Since the sensitivity was not high enough for observing broad $B^{**}_{u,d}$-states some assumptions about their mass splittings and production rates relative to the narrow states were made, based on HQET predictions and recent measurements from the charm sector. This leads to the following total production rate per b-jet for $B^{**}_{u,d}$-mesons:

$$\frac{\sigma(B^{**}_{u,d}) \cdot \mathrm{BR}(\mathrm{B^{**}_{u,d}} \to \mathrm{B}^{(*)}\pi)}{\sigma_b} = 0.153 \pm 0.014(\mathrm{stat})^{+0.027}_{-0.008}(\mathrm{syst}) \pm 0.015(\mathrm{model}).$$

The narrow $B^{**}_{u,d}$-production rate per b-jet has been extracted to be

$$\left(\frac{\sigma(B^{**}_{u,d}) \cdot \mathrm{BR}(\mathrm{B^{**}_{u,d}} \to \mathrm{B}^{(*)}\pi)}{\sigma_b}\right)_{\mathrm{narrow}} = 0.088 \pm 0.007(\mathrm{stat})^{+0.013}_{-0.004}(\mathrm{syst}) \pm 0.011(\mathrm{model}).$$

This is the first time that the production rate of the narrow resonances has been determined. The combined measurement of both the total and the narrow $B^{**}_{u,d}$-production rate together with the low background significantly improves the error on the first compared with existing measurements, thus leading to the best single measurement of the total production rate.

The mass of the B^*_2-meson has been measured to

$$m(\mathrm{B}^*_2) = 5742 \pm 12 \text{ MeV/c}^2.$$

The mass splitting between the two narrow states B^*_2 and B_1 has been determined to

$$m(\mathrm{B}^*_2) - m(\mathrm{B}_1) = 15 \pm 13(\mathrm{stat}) \pm 4(\mathrm{syst}) \pm 5(\mathrm{model}) \text{ MeV/c}^2,$$

leading to a B_1-mass of

$$m(\mathrm{B}_1) = 5727 \pm 19 \text{ MeV/c}^2.$$

This is the first measurement of the hyperfine splitting within the narrow $B^{**}_{u,d}$-doublet.

For B^{**}_s-mesons, only one peak could be observed. The improved resolution compared to the previous observation of B^{**}_s-states leads to a clear interpretation of that signal, namely that it originates from the decay $B^*_{s2} \to BK$. The production rate per b-jet has been measured to

$$\frac{\sigma(B^*_{s2}) \cdot \mathrm{BR}(\mathrm{B^*_{s2}} \to \mathrm{BK})}{\sigma_b} = 0.0093 \pm 0.0020(\mathrm{stat}) \pm 0.0013(\mathrm{syst}).$$

The B^*_{s2}-mass has been extracted to

$$m(\mathrm{B}^*_{s2}) = 5852 \pm 4 \text{ MeV/c}^2$$

improving the previous measurement significantly.

A search for $\Sigma_b^{(*)}$-baryons was made by combining inclusively reconstructed Λ_b-baryons with a charged pion originating from the primary vertex to form a $\Sigma_b^{(*)}$-candidate. No sigificant signal could be observed. An upper limit for the production rate per b-jet of a narrow resonance of

$$\frac{\sigma(\Sigma_b^{(*)}) \cdot \mathrm{BR}(\Sigma_b^{(*)} \to \Lambda_b\pi)}{\sigma_b} < 0.0124 \text{ @ } 95\% \text{ CL}$$

has been extracted in the Q-value range smaller than 300 MeV/c^2.

Bibliography

[1] M. Gell-Mann, Y. Ne'emem, *The Eightfold Way*, W. A. Benjamin inc., New York 11 (1994).

[2] M. Gell-Mann, California Institute of Technology Synchrotron Laboratory Report **No. CTSL-20** (1961);
Y. Ne'emen, Nucl. Phys, **26** (1961) 222.

[3] M. Gell-Mann, Phys. Lett. **8** (1964) 214;
G. Zweig, CERN Report, **No. 8182/TH 401** (1964).

[4] Particle Data Group, K. Hagiwara et al, Phys. Rev. **D 66** (2002) 010001.

[5] P. Schmüser, *Feynman-Graphen und Eichtheorien für Experimentalphysiker* (in German), Springer Verlag (1995).

[6] F. Halzen, A. D. Martin, *Quarks and Leptons: An Introductory Course in Modern Particle Physics*, John Wiley & Sons Inc., New York, (1984).

[7] V. Kopeliovich, *Exotic baryon states in topological soliton models*, plenary talk given at QUARKS 2004, Pushkinskie Gory, Russia, 2004.

[8] B. Grinstein, Nucl. Phys **B339** (1990) 253;
H. Georgi, Phys. Lett. **B240** (1990) 447;
A. Falk, H. Georgi, B. Grinstein and M. Wise, Nucl. Phys. **B343** (1990) 1.

[9] M. Neubert: 'B Decays and the Heavy-Quark Expansion'. In: *Heavy Flavours II*, Advanced Series on Directions in High Energy Physics - Vol. 15, eds A. J. Buras, M. Lindner (World Scientific, 1998), 239.

[10] M. B. Wise, *Heavy Quark Physics: Course*, Talk given at Les Houches Summer School in Theoretical Physics, Session 68: Probing the Standard Model of Particle Interactions, Les Houches, France, 28 Jul - 5 Sep 1997, published in Les Houches 1997, Probing the standard model of particle interactions, Pt. 2 105 (1997), e-Print Archive: hep-ph/9805468.

[11] N. Isgur and M. Wise, Phys. Lett. **B232** (1989) 113 and **B237** (1990) 527;
M. Voloshin and M. Shifman, Sov. J. Nucl. Phys. **45** (1987) 292 and **45** (1987) 292.

[12] E. Eichten, K. Gottfried, T. Kinoshita, J. Koghut, K. D. Lane and T.-M. Yan, Phys. Rev. Lett. **34** (1975) 369;
E. Eichten, K. Gottfried, T. Kinoshita, K. D. Lane and T.-M. Yan, Phys. Rev. **D17**

(1978) 3090 and **D21** (1980) 313(E);
E. Eichten, K. Gottfried, T. Kinoshita, K. D. Lane and T.-M. Yan, Phys. Rev. **D21** (1980) 203.

[13] C. Quigg and J. L. Rosner, Phys. Lett. **B71** (1977) 153.

[14] A. Martin, Phys. Lett. **B93** (1980) 338 and **B100** (1981) 511.

[15] W. Buchmüller, G. Grunberg and S.-H. H. Tye, Phys. Rev. Lett. **45** (1980) 103.

[16] B. Anderson, G. Gustafson, G. Ingelman and T. Sjöstrand, Phys. Rep **97** (1983) 31.

[17] U. Kerzel, *First Measurement of the b-Quark Fragmentation function $f(z)$ in Z^0 decays with the DELPHI detector at LEP I*, Diploma Thesis, EKP Report IEKP-KA/2002-3, Universität Karlsruhe 2002, available at
http:///www-ekp.physik.uni-karlsruhe.de/pub/web/thesis/diplomathesis_kerzel.ps.gz.

[18] C. Kreuter, *Observation of Orbitally Excited B Mesons with the DELPHI detector at LEP*, PhD-Thesis, EKP Report IEKP/96-02, Universität Karlsruhe 1996,
available at http:///www-ekp.physik.uni-karlsruhe.de/pub/web/thesis/kreuter.ps.gz.

[19] T. Sjöstrand, Computer Phys. Com. **39** (1986) 347;
T. Sjöstrand and M. Bengtson, Computer Phys. Comm. **43** (1987) 367.

[20] DELPHI Collab., P. Abreu et al., Z. Phys **C73** (1996) 11.

[21] A. F. Falk and M. Neubert, Phys. Rev **D47** (1993) 2965 and 2982.

[22] M. B. Wise: 'Heavy Flavor Theory: Overview'. In: Proceedings of the 16th International Symposium on Lepton and Photon Interactions, 1993, Ithaca, NY, pp 253-273, eds P. Drell, D. Rubin, AIP Conference Proceedings 302;
N. Isgur, M. B. Wise: 'Heavy Quark Symmetry'. In: *B Decays*, 2nd edition, ed. S. Stone (World Scientific, 1994), 231.

[23] D. Ebert, V. O. Galkin and R. N. Faustov, Phys. Rev. **D 57** (1998) 5663;
Erratum-ibid. **D 59** (1999) 019902.

[24] A. F. Falk, M. E. Peskin, Phys. Rev. **D 49** (1994) 3320.

[25] T. Mannel, Acta. Phys. Pol. **B 29** (1998) 1413.

[26] M. Genovese et al., Phys. Rev. **D59** (1999) 014012.

[27] R. K. Bhaduri et al., Nuovo Cimento **A 65** (1981) 376.

[28] C. Semay and B. Silvestre-Brac, Nucl. Phys. **A 618** (1997) 455.

[29] R. F. Lebed, Phys. Rev. **D 47** (1993) 1134.

[30] A. Ali Khan, *Effective Field Theories and Quantum Chromodynamics on the Lattice*, e-Print Archive hep-lat/0403006 and the references therein.

[31] S. Godfrey and R. Kokoski, Phys. Rev. **D 43** (1991) 1679.

[32] M. Gronau and J. L. Rosner, Phys. Rev. **D49** (1994) 254.

[33] S. N. Gupta and J. M. Johnson, Phys. Rev. **D 51** (1995) 168.

[34] N. Isgur, Phys. Rev. **D 57** (1998) 4041.

[35] A. F. Falk and T. Mehen, Phys. Rev. **D 53** (1996) 231.

[36] E. Eichten, C. T. Hill and C. Quigg, Phys. Rev. Lett. **71** (1993) 4116;
E. Eichten, C. T. Hill and C. Quigg, Fermilab Conf 94/118 T.

[37] L3 Collab., M. Acciarri et al., Phys. Lett. **B 345** (1995) 589.

[38] ALEPH Collab., D. Buskulic et al., Zeit. Phys. **C 69** (1996) 393.

[39] DELPHI Collab., P. Abreu et al., Zeit. Phys. **C 68** (1995) 353.

[40] OPAL Collab., R. Akers et al., Zeit. Phys. **C 66** (1995) 27.

[41] CLEO Collab., S. Anderson et al., Nucl. Phys. **A 663** (2000) 647.

[42] BELLE Collab., K. Abe et al., BELLE-CONF-0235, submitted to ICHEP02.

[43] BABAR Collab., B. Aubert et al., Phys. Rev. Lett. **90** (2003) 242001;
CLEO Collab., D. Besson et al., CLEO CONF 03-01 (2003).

[44] CLEO Collab., T. Bergfeld et al., Phys. Lett. **B340** (1994) 194.

[45] Y. Kubota et al., Phys. Rev. Lett. **72** (1994) 1972.

[46] ALEPH Collab., D. Buskulic et al., Z. Phys. **C 69** (1996) 393;

[47] DELPHI Collab., P. Abreu et al., Phys. Lett. **B345** (1995) 598.

[48] OPAL Collab., R. Akers et al., Z. Phys. **C 66** (1995) 19.

[49] ALEPH Collab., R. Barate et al., Phys. Lett. **B 425** (1998) 215.

[50] L3 Collab., M. Acciarri et al., Phys. Lett. **B465** (1999) 323.

[51] CDF Collab., T. Affolder et al., Phys. Rev. **D 64** (2001) 072002.

[52] C. Weiser, private communication.

[53] DELPHI Collab., M. Feindt et al., *First Evidence for* Σ_b *and* Σ_b^* *Baryons*, contribution to EPS 1995, Brussels, Belgium, EPS-HEP 95 Ref. eps0565, DELPHI internal Note, DELPHI 95-107 PHYS 542.

[54] A. Warburton for the CLEO Collab., *First Observation of the* Σ_c^{*+} *Charmed Baryon, and New Measurements of the* Σ_c^0, Σ_c^+, Σ_c^{++}, *and* Ω_c^0 *Charmed Baryons*, Talk given at ICHEP 2000, Osaka, Japan, 27 Jul - 2 Aug 2000, published in Proceedings of the 30th International Conference on High Energy Physics, Volume I, eds. C. S. Lim and T. Yamanaka, 387 (2001).

[55] CLEO Collab., G. Brandenburg et al.; Phys. Rev. Lett. **78** (1997) 2304.

[56] R. Roncaglia et al., Phys. Rev. **D 51** (1995) 1248;
A. Martin; Phys. Lett. **B 103** (1981) 51.

[57] A. Scherer, *Neuronale Netze: Grundlagen und Anwendungen* (in German), Friedr. Vieweg & Sohn Verlagsgesellschaft mbH, Braunschweig/Wiesbaden, Germany, 1997.

[58] StatSoft, *Statistics Textbook*,
Internet page, URL: http://www.statsoftinc.com/textbook/stathome.html.

[59] D. E. Rumelhart, G. E. Hinton, R. J. Williams, 'Learning Internal Representations by Error Propagation', in *Parallel Distributed Processing: Exploarations in the Microstructure of Cognition* Vol. 1, eds D. E. Rumelhart, J. L. McClelland (MIT Press, 1986).

[60] M. D. Richard, R. P. Lippmann, Neural Comp. **3** (1991) 461.

[61] M. Feindt, *A Neural Bayesian Estimator for Conditional Probability Densities*, e-Print Archive physics/0402093.

[62] A. S. Weigend, A. N. Srivastava, Int. J. of Neural Systems **2** (no. 2) (1995).

[63] V. Blobel, E. Lohrmann, *Statistische und numerische Methoden der Datenanalyse* (in German), Teubner, Stuttgart/Leipzig, Germany, 1998.

[64] Phi-T, Physics Information Technologies, Karlsruhe, Germany, http://www.phi-t.de.

[65] DELPHI Collab., Nucl. Instr. and Meth. **A303** (1991) 233.

[66] DELPHI Collab., Nucl. Instr. and Meth. **A378** (1996) 57.

[67] DELPHI Collab., P. Abreu et al., Z. Phys, **C68** (1995) 353.

[68] T. Sjöstrand, Computer Phys. Comm. **82** (1994) 74.

[69] D. Brown, M. Frank, *Tagging b-Hadrons Using Track Impact Parameters*, ALEPH Note 92-135 (1992).

[70] G. V. Borisov, *Lifetime Tag of Events* $Z^0 \to b\bar{b}$ *with the DELPHI detector. AABTAG program.*, DELPHI internal Note, 94-125 PROG 208 (1994).

[71] DELPHI Collab., J. Abdallah et al., Eur. Phys. J. **C32** (2004) 185.

[72] W. J. Murray, *Measurement of the Beam Position in DELPHI*, DELPHI Note 96-6 PHYS 590 (1996).

[73] G. V. Borisov and C. Mariotti, Nucl. Instr. Meth., **A372** (1996) 181;
G. V. Borisov and C. Mariotti, *Tuning of the Track Impact Parameter Resolution of the Upgraded DELPHI Detector*, DELPHI Note 97-95 PHYS 717 (1997).

[74] G. Borisov, Nucl. Instr. and Meth. **A417** (1998) 384.

[75] DELPHI Collab., P. Abreu et al., E. Phys. J. **C10** (1999) 415.

[76] T. W. Anderson, *An Introduction to Multivariate Analysis*, Wiley, New York, 1958.

[77] W. Adam et. al., Nucl. Instr. Meth. **A371** (1996) 240.

[78] M. Battaglia and P. M. Kluit, *Particle Identification using the RICH Detectors Based on the RIBMEAN Package*, DELPHI Note 96-133 RICH 90 (1996).

[79] E. Schyns, *NEWTAG - π, K, p Tagging for DELPHI RICHes*, DELPHI Note 96-103 RICH 89 (1996).

[80] Z. Albrecht, M. Feindt and M. Moch, *MACRIB: High Efficiency - High Purity Hadron Identification for DELPHI*, e-Print Archive hep-ex/0111081.

[81] M. Feindt, W. Oberschulte gen. Beckmann and C. Weiser, *How to Use the MAMMOTH Program* DELPHI internal Note 96-52 PROG 216;
C. Weiser, *Messung der Produktionsraten von Σ^--, B_s- und B^+-Hadronen in Z^0-Zerfällen*, PhD thesis (in German), EKP Report IEKP-KA/98-5, Universität Karlsruhe 1998, available at
http://www-ekp.physik.uni-karlsruhe.de/pub/web/thesis/weiser.KA98-5.ps.gz;
DELPHI Collab., P. Abreu et al., Phys. Lett. **B 475** (2000) 429.

[82] Z. Albrecht, T. Allmendinger, G. Barker, M. Feindt, C. Haag and M. Moch, *BSAURUS - A Package For Inclusive B-Reconstruction in DELPHI*, DELPHI Note DELPHI 2000-069 PHYS 868, EKP Report IEKP-KA/2001-3, e-Print Archive hep-ex/0102001.

[83] L. Lönnblad, Computer Phys. Comm. **71** (1992) 15.

[84] L. Lönnblad, C. Peterson and T. Rögnvaldson, Computer Phys. Comm., **70** (1992) 167.

[85] DELPHI Collab., J. Abdallah et. al., Eur. Phys. J. **C33** (2004) 307.

[86] http://claires.home.cern.ch/claires/lepblife.html.

[87] http://lepbosc.web.cern.ch/LEPBOSC.

[88] G. Barker et al., *Measurement of the b quark fragmentation function with the DELPHI detector at LEP I*, DELPHI Note, in preparation.

[89] CUSB2 Collab., Lee-Franzini et al., Phys. Rev. Lett. **65** (1990) 2947.

[90] Z. Albrecht, *Analysis of Excited B-Mesons*, PhD-Thesis, EKP Report IEKP/03-16, Universität Karlsruhe 2003,
available at http:///www-ekp.physik.uni-karlsruhe.de/pub/web/thesis/albrecht_phd.ps.gz.

[91] S. Hügel, *Suche nach Resonanzen im Endzustand $B\pi^+\pi^-$ mit dem DELPHI-Detektor am LEP-Beschleuniger*, Diploma Thesis (in German), EKP Report IEKP-KA/2003-22, Universität Karlsruhe 2003,
available at http://www-ekp.physik.uni-karlsruhe.de/pub/web/thesis/huegel_dipl.ps.gz.

[92] DELPHI Collab., P. Abreu et al., Phys. Lett. **B 475** (2000) 429.

[93] P. Roudeau, private communication.

Acknowledgements

Many people contributed to the finishing of this thesis by some means or other. I want to use the opportunity to thank them at this point.

I thank Prof. Dr. Michael Feindt for the interesting and challenging subject of this work, for his motivating supervision, his never ebbing ideas and the opportunity to join the DELPHI experiment and to participate in the data taking process. Moreover, he made it possible for me to present my results at conferences and to participate in summer schools. I also thank Prof. Dr. Günter Quast for the co-supervision of my work and for his useful comments.

I am deeply indebted to Dr. Gary Barker, Dr. Zoltán Albrecht and Ulrich Kerzel with whom I worked. The neural network techniques presented in this thesis were developed and optimised together with them.

I express my thanks to Zoltán Albrecht, Thomas Allmendinger, Marcel Stanitzki (who managed to get their PhD before me) and Claudia Lecci, Svenja Richter, Christian Dörr, Joachim Heuser, Simon Hügel, Philipp Mack, Michael Milnik, Ludger Ramler and our guests Arantza Oyanguren and Jörgen Dalmau for sharing the office with me for at least some months and for the enjoyable atmosphere in our office. It has always been quite funny and it was often crowded in our office. Thanks to Gary, Uli, Ludger and Jochen the weekends spent at the institute were not that lonely.

I owe Mrs. Edeltraud Haas and Mrs. Waltraud Weißmann a debt of gratitude for their help with all the stuff concerning business trips, administration and bureaucracy at the university.

Special thanks go to the institute's system administrators Yves Kemp, Christian Sander, Dr. Patrick Schemitz, Dr. Jens Rehn and Dr. Marcel Stanitzki for their tireless efforts to keep the entire computer system running - especially one computer exclusively at my service during the last months.

I am much obliged to Dr. Alexander Dierlamm, cand. phys. Joachim Heuser, Dipl.-Ing. Gudrun Hillebrand, StR Peter Langrock, Dr. Stephanie Menzemer, Dr. Jens Rehn and Dr. Marcel Stanitzki for (more or less) carefully reading the manuscript of this thesis (or parts of it).

I thank all members of the institute, especially the EKP AllStars, for the pleasant and

stimulating atmosphere and for their patience with me during lunch and coffee breaks. They did more often wait until I was finished than they left the table without me.

The members of the LEP1 physics team of DELPHI mainly provided a friendly atmosphere in the discussions about the analyses presented in this thesis. I thank them for the insights these discussions gave me into the analyses and especially into the systematics and for the opportunity to present the results at an international conference.

I am grateful to all professors of our institute at the physics high-rise building. Somehow they always managed to support my work financially after the end of my scholarship which was granted by the Land of Baden-Württemberg and the Graduiertenkolleg "Hochenergiephysik und Teilchenastrophysik" promoted by the German Research Community and the German Federal Ministry for Education and Research. I thank them for my scholarship.

Last but not least I would like to express my thanks to my family and my friends for the support and the diversion outside of physics whenever it was necessary.